Experimental Evaluation of Advanced Digital Signal Processing for Intra-Datacenter Systems using Direct-Detection

Dissertation
zur Erlangung des akademischen Grades
Doktor der Ingenieurswissenschaften (Dr.-Ing.)
der Technischen Fakultät
der Christian-Albrechts-Universität zu Kiel

vorgelegt von
Tom Jonas Wettlin

Kiel 2023

1. Gutachter:	Prof. Dr.-Ing. Dipl.-Wirt. Ing. Stephan Pachnicke
2. Gutachter:	Prof. Dr.-Ing. Norbert Hanik
3. Gutachter:	Prof. Dr.-Ing. Sander Wahls
Tag der mündlichen Prüfung:	28. August 2023

Vorwort

Die vorliegende Arbeit ist im Rahmen meiner Tätigkeit als wissenschaftlicher Mitarbeiter am Lehrstuhl für Nachrichtenübertragungstechnik der Christian-Albrechts-Universität zu Kiel entstanden. Die gesamte Forschung fand in enger Zusammenarbeit mit der Datacenter Network Gruppe des Huawei Munich Research Centers statt.

Als Erstes danke ich meinem Betreuer Herrn Prof. Dr.-Ing Stephan Pachnicke für die Möglichkeit an diesem interessanten Projekt zu arbeiten, die systematische Anleitung und die zahlreichen produktiven Diskussionen während der gesamten Zeit. Weiter danke ich Herrn Prof. Dr.-Ing. Norbert Hanik für die Erstellung des zweiten Gutachtens und Prof. Dr.-Ing. Sander Wahls für die Erstellung des dritten Gutachtens.

Vielen Dank an meine Kollegen am Lehrstuhl Lars, Simon, Jonas, Rebekka, Adrian, Shi, Mihail, Olaf, Alexandr, Silas, Kay, Tim, Sebastian, Ali, Sandra und Petra für die angenehme Atmosphäre, die schönen Reisen zu Konferenzen, die gute Zusammenarbeit, und das Korrekturlesen.

Mein Dank gilt auch den Projektpartnern des Huawei Munich Research Centers Dr. Stefano Calabrò, Dr. Talha Rahman, Dr. Nebojsa Stojanovic, Dr. Jinlong Wei und Md Sabbir-Bin Hossain. Während der regelmäßigen, ausführlichen Diskussionen über meine Fortschritte haben Eure Ideen und Anmerkungen sehr geholfen, meine Ergebnisse zu verbessern. Ebenfalls danke ich Euch für die zahlreichen, hilfreichen Kommentare zu meinen Veröffentlichungen.

Ein großer Dank gilt meiner Familie, die mich während meines gesamten Studiums in jeglicher Hinsicht unterstützt hat - ohne Euch wäre das nicht möglich gewesen.

Zuletzt geht riesiger Dank an Kira für die ständige Unterstützung und Deine stets liebevolle Art.

Abstract

To keep the pace of the continuously growing data traffic demand, fiber-optic transmission systems face tremendous challenges. This work focuses on such systems deployed inside datacenters, where a major part of the global traffic occurs. For this application, high data rates and low costs are crucial factors. Currently, systems using intensity modulation (IM) and direct-detection (DD) are serving this demand in the most efficient way. The next generations of intra-datacenter systems will reach rates of 800 Gb/s and 1.6 Tb/s per fiber. This makes IM/DD systems with data rates of 200 Gb/s and beyond per wavelength inevitable to keep the transceiver count low. Due to impairments like bandwidth limitations of transceiver components, fiber effects such as chromatic dispersion (CD) and nonlinearities, such rates can only be reached using digital signal processing (DSP).

Various transmitter and receiver DSP approaches to overcome these impairments in systems using pulse-amplitude modulation are shown, evaluated and compared. These include schemes focusing on the lowpass characteristic of the transmission channel, such as feed-forward equalization, decision-feedback equalization (DFE) and its transmitter counterpart Tomlinson-Harashima pre-coding (THP), partial response signaling, noise whitening filters and Viterbi equalization. For several of these approaches, variations and optimizations are presented. It is shown that duobinary equalization performs well under strong bandwidth constraints and offers a good CD tolerance. THP is the best approach for the strongest lowpass characteristics. Furthermore, variations of DFE combined with a noise whitening filter show promising performance. To tackle nonlinear effects, Volterra nonlinear equalization is thoroughly investigated and different options to reduce the complexity are considered. Various experiments reaching data rates beyond 200 Gb/s are presented.

To cope with the increasing limitations by CD, especially for applications in datacenter campus networks, also advanced DD systems are investigated. The focus of this work lies on simple systems in terms of hardware complexity, namely electronic dispersion pre-compensation and self-coherent systems. Several alternatives to the well-established Kramers-Kronig receiver are considered and advantages of schemes like the DC-value method at low digital oversampling factors are pointed out.

Zusammenfassung

Um mit der ständig wachsenden Datenverkehrsnachfrage Schritt zu halten, stehen Glasfaserübertragungssysteme vor enormen Herausforderungen. Diese Arbeit konzentriert sich auf Systeme für die Anwendung innerhalb von Rechenzentren, in denen ein großer Teil des weltweiten Datenverkehrs anfällt. Für diese Anwendung sind hohe Datenraten und niedrige Kosten entscheidende Faktoren. Gegenwärtig erfüllen Systeme mit Intensitätsmodulation (IM) und Direktdetektion (DD) diese Anforderungen auf die effizienteste Weise. Die nächsten Generationen von Intra-Rechenzentrumssystemen werden Raten von 800 Gb/s und 1,6 Tb/s pro Faser erreichen. Dies macht IM/DD-Systeme mit Datenraten von 200 Gb/s und mehr pro Wellenlänge unumgänglich, um die Anzahl der Sender und Empfänger gering zu halten. Aufgrund von Beeinträchtigungen wie Bandbreitenbeschränkungen von Komponenten, Fasereffekten wie chromatischer Dispersion (CD) und Nichtlinearitäten können solche Raten nur mit digitaler Signalverarbeitung (DSP) erreicht werden.
Verschiedene Sender- und Empfänger-DSP Ansätze zur Überwindung dieser Beeinträchtigungen in Systemen mit Pulsamplitudenmodulation werden gezeigt, bewertet und verglichen. Dazu gehören Verfahren, die sich auf die Tiefpasscharakteristik des Übertragungskanals konzentrieren, wie z.B. Feed-Forward-Entzerrung, Decision-Feedback-Entzerrung (DFE) und dessen senderseitiges Pendant Tomlinson-Harashima-Vorcodierung (THP), sowie Partial-Response Codierung, Rauschglättungsfilter und Viterbi-Entzerrung. Für mehrere dieser Ansätze werden Variationen und Optimierungen vorgestellt. Es wird gezeigt, dass die duobinäre Entzerrung auch bei starken Bandbreitenbeschränkungen effektiv funktioniert und eine gute CD-Toleranz bietet. THP ist der beste Ansatz für Kanäle mit den stärksten Tiefpasscharakteristiken. Des Weiteren zeigen Variationen von DFE in Kombination mit einem Rauschglättungsfilter vielversprechende Ergebnisse. Zur Bewältigung nichtlinearer Effekte wird die nichtlineare Volterra-Entzerrung eingehend untersucht und verschiedene Optionen zur Reduzierung der Komplexität werden gezeigt. Es werden verschiedene Experimente vorgestellt, in denen Datenraten jenseits von 200 Gb/s erreicht werden.
Um die zunehmenden Einschränkungen durch CD bewältigen zu können, insbesondere für Anwendungen in Rechenzentrums-Campus-Netzwerken, werden auch weiterentwickelte DD-Systeme untersucht. Der Schwerpunkt dieser Arbeit liegt auf einfachen Systemen in Bezug auf die Hardwarekomplexität, nämlich elektronischer Dispersionsvorkompensation und selbstkohärenten Systemen. Es werden mehrere Alternativen zum bewährten Kramers-Kronig-Empfänger betrachtet und die Vorteile von Verfahren wie der DC-Value-Methode bei niedrigen digitalen Überabtastungsraten aufgezeigt.

Contents

Chapter 1

Introduction

Fiber-optic transmission systems serve as the backbone of today's internet and telecommunications infrastructure. The usage of silica fiber as a transmission medium brought several advantages over traditional copper cables, especially a low loss and an ultra-high bandwidth. These properties enabled exponentially growing data rates over distances spanning from short-reach to ultra long-haul sub-sea transmission in the past decades.

The first commercial fiber-based systems were deployed in the 1980s [1]. These systems were based on on-off keying (OOK) and were mostly limited to a single wavelength. An important step in the evolution of fiber-optic systems was the invention of practical optical amplifiers, especially the Erbium-doped fiber amplifier (EDFA) [2, 3]. These, alongside other achievements such as improved dispersion management, enabled high-capacity wavelength division multiplexing (WDM) transmission. A further milestone for long-reach transmission systems was set by deploying coherent transmission systems. This way, the inphase and quadrature components as well as the orthogonal polarizations of the optical signal were usable for data transmission, increasing the number of degrees of freedom by a factor of four compared to earlier systems. Additionally, digital signal processing (DSP) simplified the transmission systems by replacing hardware such as dispersion compensating fiber (DCF).

As of today, coherent systems are used for many applications ranging from links between datacenters to sub-sea transmission. Solely for short-reach applications such as intra-datacenter communications and access networks, systems using intensity-modulation (IM) and direct-detection (DD) are still the preferred structure. In these applications, the cost of the transceiver hardware plays a more dominant role and fiber effects are less severe so that these simpler systems show an improved cost-efficiency.

For the next generations of 800 Gb/s and 1.6 Tb/s Ethernet, high per-lane rates are required to keep the transceiver count low. This increases the challenges for IM/DD systems, making higher-order modulation formats and DSP inevitable considerations.

In this work, the challenges and solutions for future IM/DD systems are investigated in simulations and experiments. An overview of DSP approaches to overcome various impairments is given and the relative advantages of the different schemes are shown. Additionally, the option of advanced DD systems using a more sophisticated hardware setup to increase the impairment tolerance and increase the reachable rates is considered and evaluated.

1.1 Structure of this Work

This work is divided into six chapters. After the introduction, the transmission channel and basic concepts are described in Chapter 2. This includes an overview of the datacenter structure, relevant components, and fiber effects. The possible system configurations for fiber-optic transmission systems are explained and the modulation formats as well as forward error correction limits used in the following chapters are described.

Chapter 3 gives an overview of DSP approaches for IM/DD systems. This includes approaches for the transmitter and receiver DSP to overcome various impairments such as bandwidth limitations, chromatic dispersion and nonlinearities. Subsequently, in Chapter 4 DSP approaches for advanced DD systems are explained. These include electronic dispersion compensation (EDC) at the transmitter and self-coherent (SCOH) detection using the Kramers-Kronig (KK) receiver and alternative concepts.

In Chapter 5, the approaches introduced in the previous parts are investigated thoroughly based on simulations as well as experiments on various lab setups. The properties and benefits of all schemes are evaluated and comparisons between the different approaches are shown. Finally, in Chapter 6 conclusions are drawn and an outlook is presented.

Chapter 2

Fiber-Optic Transmission Systems for Intra-Datacenter Applications

Datacenters (DCRs) play a key role in current internet applications. The huge drivers for internet traffic like cloud computing, internet of things and video streaming are running in the DCR infrastructure [4]. Leading companies in these fields are building larger and larger DCRs to cope with the ever-increasing demand for these services. For the connectivity inside such mega DCRs, fiber-optics based interconnects play a central role. Different connection scenarios with varying distance requirements need to be covered by optical links. To get an overview of the requirements, a schematic DCR architecture is depicted in Fig. 2.1. Several servers are bundled inside a rack. All of these are connected to the top of rack (ToR) switch. The next stages are formed by the leaf and spine layers. Finally, different physically distributed DCRs are connected via optical links. The connections between the layers can be separated into four scenarios. Typical distances for each of the scenarios are summarized in Tab. 2.1 [5]. While the connections between servers and ToR switches are up to 20 m in length, ToR to leaf connections can be up to 100 m. The third scenario of leaf to spine connections contains distances between 500 m and 2 km. Interconnects between DCRs are typically classified by distances of up to 100 km [6].

The traffic growth makes companies also consider the option of co-locating several mega DCRs on a single campus. An example of this is the Facebook DCR in Clonee, Ireland, where currently two hyper-scale datacenters are existing and even more buildings on the same campus are planned [7]. The interconnects for such cases are referred to as DCR campus networks and distances of up to 10 km are considered to cover them [8].

Table 2.1: Distances that need to be covered by optical interconnects for the connection scenarios between the different layers inside DCRs according to [5].

	Scenario 1	Scenario 2	Scenario 3	Scenario 4
Application	Server to ToR	ToR to Leaf	Leaf to Spine	Inter Datacenter
Distance	<20 m	<100 m	<2 km	<100 km

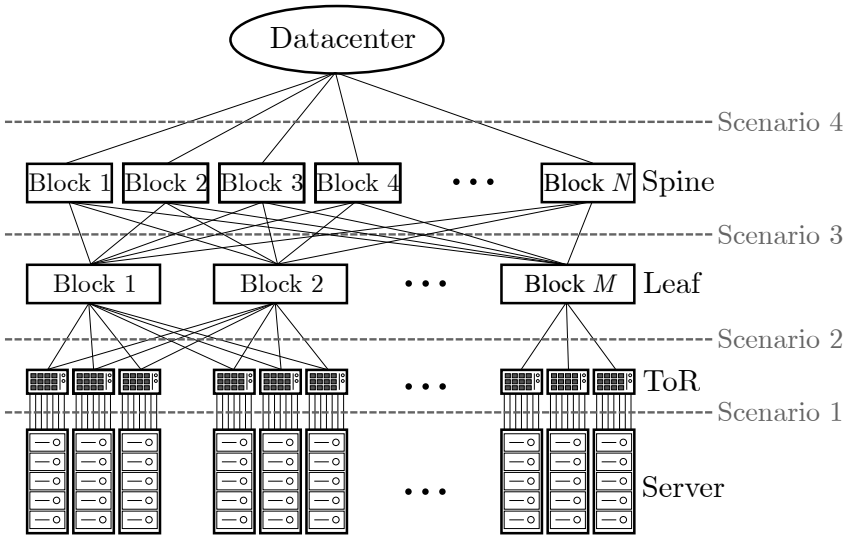

Figure 2.1: Schematic structure of a typical DCR according to [4, 5].

The investigations in this work focus on two reach scenarios. Those are the leaf to spine connections of up to 2 km distance, also denoted as far reach (FR) scenario, and DCR campus networks of up to 10 km length, known as long reach (LR) scenario. For the FR scenario, the standardization of 800 Gb/s systems is currently under progress [9, 10]. A proposal for this is a coarse wavelength division multiplexing (CWDM)-4 system based on 200 Gb/s/λ IM/DD [5]. For the LR scenario, besides IM/DD systems, also coherent systems are considered [4, 11, 12].

In the following, the transmission systems that are applied for the considered scenarios are explained in detail. First, the relevant electrical and optical components are described. Afterwards, the optical fiber as a transmission medium is introduced and the relevant impairments are explained. Then, different configurations of optical transmission systems are shown. Finally, relevant modulation formats and a forward error correction (FEC) option for the considered short-reach scenarios are introduced.

2.1 Electrical and Optical Components

An optical transmission system requires several components for the generation and detection of the optical information-containing signal. A schematic of such a transmission system is shown in Fig. 2.2. After the transmitter DSP, the digital-to-analog converter (DAC) generates an analog electrical signal. This signal is modulated on an optical carrier signal in the electrical-to-optical (E/O) stage. The optical signal is transmitted over the optical link. Inside the link, optical amplification and filtering may be applied,

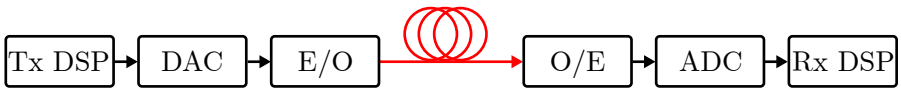

Figure 2.2: Basic setup of an optical transmission system.

depending on the transmission reach and power budget. After transmission, the optical signal is converted into an electrical analog signal in the optical-to-electrical (O/E) stage. Afterwards, a digital signal is generated by the analog-to-digital converter (ADC), before the receiver DSP is performed. The relevant electrical and optical components will be explained in the following subsections.

2.1.1 Electrical-to-Optical Conversion

For transmission over the optical fiber, the electrical baseband signal is converted into an optical bandpass signal. This step can either be conducted by a directly modulated laser (DML) or by an external modulator. The optimal modulator type strongly depends on the application scenario. While DMLs and external intensity modulators can only modulate one-dimensional information on the optical signal, polarization multiplexing (PolMux) inphase-quadrature (IQ) modulators have four degrees of freedom. Besides these capabilities, cost, complexity and form factor play an important role. In the following, two approaches for external intensity modulation, namely the electro-absorption modulator (EAM) and the Mach-Zehnder modulator (MZM) are described. Afterwards, IQ modulation is explained.

Intensity Modulation

For intensity modulation, DMLs offer the attractive properties of low cost and a small footprint [13–15]. However, signals modulated by DMLs experience a higher frequency chirp than for EAMs and MZMs. This effect can result in a significant performance degradation [15, 16]. Therefore, DMLs are rarely used for high-rate systems [17]. The majority of the experimental results that are shown in this work are based on the modulation with an external MZM. Additionally, a few results are based on an O-band EAM. Since no results based on DML are shown, only the former two intensity modulation approaches are explained in more detail in the following.

Electro-Absorption Modulated Laser The concept of the EAM is based on the Franz-Keldysh effect, which describes a dependence of the bandgap of a semiconductor on an externally applied electrical field [17]. Therefore, an external voltage can be used to control the absorption of a transparent semiconductor layer [17]. EAMs are smaller than MZMs and use the same semiconductor material as the laser, leading to the advantage

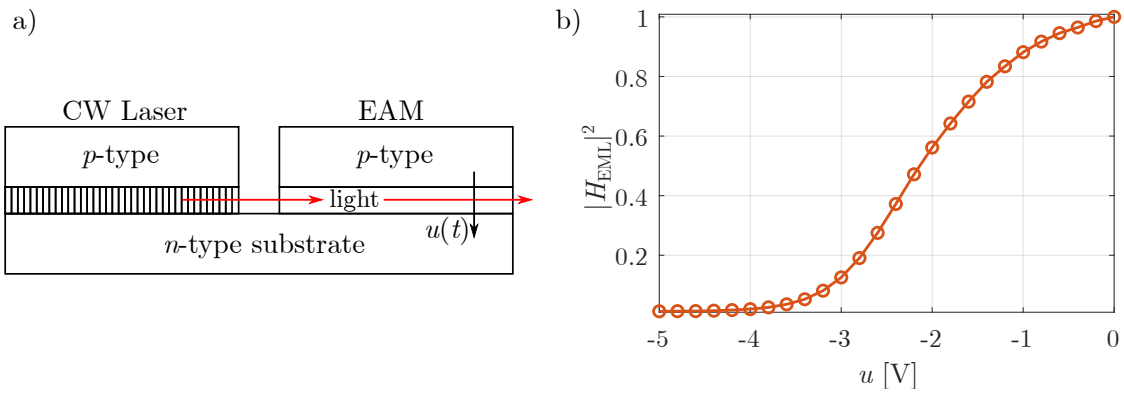

Figure 2.3: Setup and characteristic of an EML. a) shows a schematic EML consisting of a CW laser and an EAM integrated on the same substrate according to [18] and b) shows the measured power characteristic of the CIG ETV800GXLMD001.

that laser and EAM can be integrated on the same chip [17, 18]. The combination of an EAM and a continuous wave (CW) laser is called electro-absorption modulated laser (EML). The structure of an EML is schematically depicted in Fig. 2.3 a). The external voltage $u(t)$ describes the electrical input signal that is modulated on the optical carrier.

EMLs have a nonlinear input-output characteristic H_{EML}. An example of a measured power characteristic of an actual lab component (CIG ETV800GXLMD001) is shown in Fig. 2.3 b). It is visible that the input voltage signal needs to contain a certain direct current (DC) part in order to utilize a linear region of the characteristic.

The electrical field that is applied to the EAM does not only change the absorption of the semiconductor material but also influences the refractive index. Therefore, the signal modulated by an EAM is subject to chirp [15, 18, 19]. The transient frequency chirp induced by an EAM is given by

$$\Delta f = \frac{\alpha_{\mathrm{C}}}{4\pi} \frac{1}{P(t)} \frac{dP(t)}{dt}, \tag{2.1}$$

where $P(t)$ is the optical output power and α_{C} is the linewidth enhancement factor [15, 19]. The parameter α_{C} typically lies below 1 for EAMs [18].

Mach-Zehnder Modulator The MZM is a frequently used external modulator in IM/DD systems. It is based on the combination of two Mach-Zehnder interferometers (MZIs) [17, 18]. These are utilizing the Pockels effect, which describes the change of a waveguide's refractive index by applying an external voltage [17]. The changed refractive index leads to a phase change in the optical signal. Most of the experiments

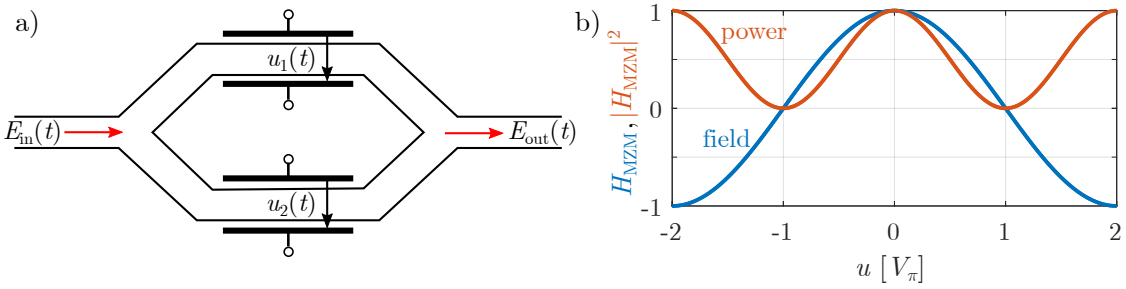

Figure 2.4: Setup and characteristic of an MZM. a) depicts the schematic structure consisting of two MZIs. b) shows the cosine characteristic, where the blue curve refers to the electrical field and the red curve to the power.

shown in this work are done using an MZM based on lithium niobate ($LiNbO_3$). It needs to be mentioned that alternative platforms such as silicon photonics are of interest in research due to low cost and complexity [20–23]. Recently, plasmonic-based MZMs gained interest because of their high reachable bandwidth beyond 100 GHz [24–26].

The structure of an MZM is shown in Fig. 2.4 a). The input signal $E_{\text{in}}(t)$ is split into two parts by a 3-dB coupler. The external voltages $u_1(t)$ and $u_2(t)$ are applied on the respective paths and the resulting signals are coupled to obtain the output signal $E_{\text{out}}(t)$.

The voltage that is applied on the MZM is given by

$$u(t) = u_D(t) + u_{\text{bias}}, \tag{2.2}$$

where $u_D(t)$ is a DC-free drive signal and u_{bias} the bias voltage. The MZMs used in this work are driven in push-pull configuration, which means they are used for amplitude modulation. This configuration is realized by selecting the voltages applied on the MZIs as $u_1(t) = -u_2(t)$. In this case, the modulator is theoretically completely chirp-free [18]. The MZM transfer function is given by

$$H_{\text{MZM}} = \cos\left(\frac{\pi}{2} \cdot \frac{u_D(t) + u_{\text{bias}}}{V_\pi}\right), \tag{2.3}$$

where V_π is the switching voltage, which is distinctive for each MZM [18]. The transfer function is depicted in Fig. 2.4 b). Besides the electrical field characteristic, the power characteristic is shown. The relevant characteristic is dependent on the detection technique. The different approaches for this are explained in Sec. 2.3. While coherent and self-coherent systems can recover the field information, DD systems can only detect the power of the optical signal.

The cosine characteristic of the MZM is nonlinear. This results in nonlinear distortions of

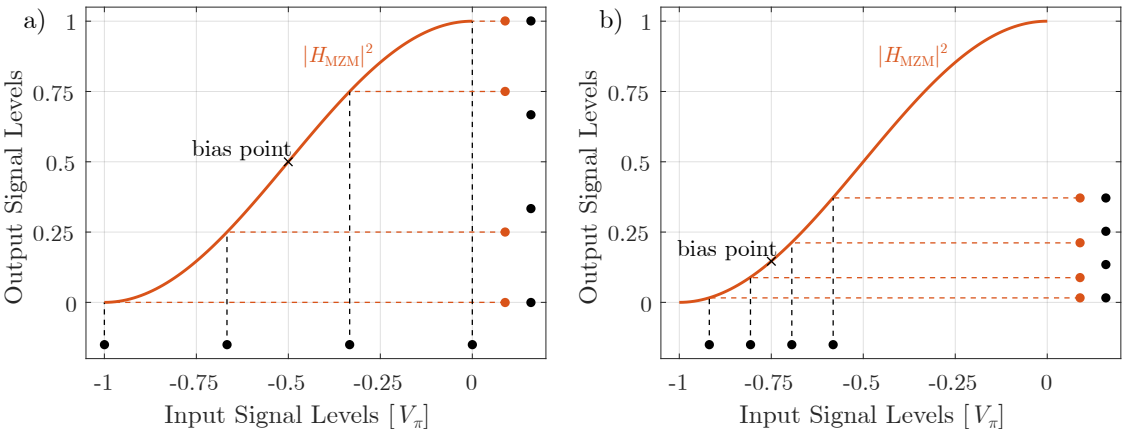

Figure 2.5: Exemplary illustration of the nonlinear input-output characteristic of an MZM. A 4-ASK signal is used as input constellation and the black dots on the right show a linear spacing for reference.

multilevel signals. Therefore, the range of the transfer function that is used for the signal modulation, needs to be chosen carefully. The impact of the nonlinear characteristic is shown for the example of a 4-amplitude shift keying (ASK) constellation in Fig. 2.5. It is visible that two parameters account for the amount and type of nonlinearities in the output signal. Those are the voltage swing of the electrical input signal $u_D(t)$ and the bias voltage u_{bias}. In Fig. 2.5 a) the bias is chosen to be at the so-called quadrature point, which lies directly in the middle between the highest and the lowest output level. For this point, the linear range of the characteristic is the highest, however, a considerable DC results in the optical output signal. In the example, the voltage swing of the input signal is chosen to cover the whole range of the characteristic. Comparing the resulting output levels with the linear spacing given as a reference shows that the output is strongly nonlinearly distorted. Choosing a smaller voltage swing would help to reduce the extent of nonlinearities but would also reduce the output power and therefore the optical signal-to-noise ratio (OSNR) of the resulting signal. In Fig. 2.5 b) a smaller bias voltage is added to the signal and a smaller voltage swing is chosen. The characteristic around the chosen bias point is highly nonlinear and the output levels are nonlinearly distorted despite the relatively small voltage swing.

In Chapter 3, techniques to combat the impact of the nonlinear MZM characteristic are introduced. One option is to adapt the symbol constellation in a way that the cosine characteristic leads to linear output levels. This scheme is explained in detail in Sec. 3.1.3. Another option is Volterra nonlinear equalization (VNLE), which is explained in Sec. 3.2.1. VNLE uses different powers of the received signal to invert the nonlinear behavior. For this, it is relevant to determine which orders of nonlinearity are contained in the

received signal. Information about this can be obtained by forming the Taylor series expansion of the MZM characteristic. Looking at the transfer function in Eq. 2.3, it is visible that the bias voltage u_{bias} leads to a shift of the cosine function. If the quadrature point is chosen as in Fig. 2.5 a), the power characteristic behaves like a $\cos^2(x - \pi/4)$ function. The Taylor series expansion around $x = 0$ results in

$$\cos^2\left(x - \frac{\pi}{4}\right) \approx 0.5 + x - \frac{2}{3}x^3 + \frac{2}{15}x^5 - ... \tag{2.4}$$

Only odd nonlinear terms exist in the resulting signal. If the bias point is chosen as in Fig. 2.5 b), the function is shifted by $-3\pi/8$. Therefore, the Taylor series expansion

$$\cos^2\left(x - \frac{3\pi}{8}\right) \approx 0.146 + \frac{1}{\sqrt{2}}x + \frac{1}{\sqrt{2}}x^2 - \frac{\sqrt{2}}{3}x^3 - ... \tag{2.5}$$

results. In this case even and odd nonlinear terms exist in the output signal. The knowledge about these nonlinearities is relevant for the parameters of the DSP.

(PolMux) IQ Modulation

IQ modulators offer the option of modulating complex signals on the optical carrier. The utilization of inphase and quadrature components for data transmission allows an increased spectral efficiency. The structure of an IQ modulator based on two MZMs in a symmetric MZI configuration is shown in Fig. 2.6 a). The optical input signal $E_{\text{in}}(t)$ is split into two parts and one arm is phase-shifted by 90°. The amplitude of both arms is modulated using an MZM. Instead of MZMs, also other amplitude modulators such as EAMs could be used at this point [27]. However, experiments shown in this work are based on a component using MZMs. The resulting amplitude-modulated signals are combined to obtain the optical output $E_{\text{out}}(t)$.

Two additional degrees of freedom for signal modulation can be obtained by utilizing the orthogonal X- and Y-polarizations of the light. The corresponding device, a PolMux

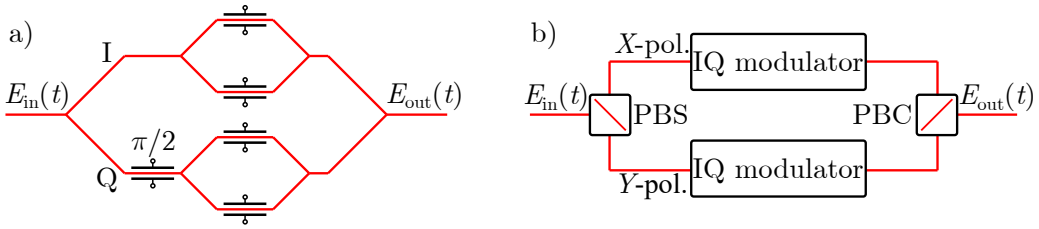

Figure 2.6: Schematic illustration of (PolMux) IQ modulators. a) shows the structure of an IQ modulator composed of two MZMs and a 90° phase shift. b) shows a PolMux IQ modulator utilizing two IQ modulators, a PBS and a PBC.

IQ modulator, is schematically shown in Fig. 2.6 b). The input signal is split into two paths for the respective polarization using a polarization beam splitter (PBS). Both polarizations are modulated using an IQ modulator before the outputs are combined by a polarization beam combiner (PBC).

2.1.2 Optical Amplification

The objective of optical amplification is the compensation of transmission and component-insertion losses. Therefore, optical amplifiers are a key enabler for optical long-haul transmission. For the intra-datacenter systems that are the subject of this work, the usage of optical amplification is generally not necessary due to the short transmission reach and hence low losses. However, the availability of high bandwidth receivers with transimpedance amplifier (TIA) is limited and thus several experiments were conducted using optical amplifiers. Additionally, the extended transmission reach for datacenter campus systems might make optical amplification necessary.

Optical amplifiers can be either used before (post-amplifier), inside (in-line amplifier) or at the end of the link (pre-amplifier) [28]. The types of amplifiers used in this work are the semiconductor optical amplifier (SOA) and the EDFA. The SOA is based on a semiconductor laser, while the EDFA uses an optical fiber doped with ions of the rare-earth metal Erbium as active medium [28]. The wavelengths that can be amplified using an EDFA, are limited to the third optical window around 1550 nm [17]. Using other rare-earth metals to dope fiber amplifiers enables the amplification of different wavelengths. For example, praseodymium can be utilized to form a fiber amplifier for the second optical window [28, 29]. The center wavelength of SOAs can be designed to lie in both, the second and third optical window.

The gain of an amplifier is defined as

$$G = \frac{P_{\text{in}}}{P_{\text{out}}}, \tag{2.6}$$

where P_{in} and P_{out} denote the power of the incoming and the output optical signals, respectively.

In both amplifier types, spontaneous emission occurs next to the desired stimulated emission. The spontaneous emission is amplified itself, leading to the so-called amplified spontaneous emission (ASE) noise. The degradation of the signal-to-noise ratio (SNR)

due to ASE noise is quantified by the noise figure, which is defined as [17]

$$F_{\mathrm{N}} = \frac{\mathrm{SNR}_{\mathrm{in}}}{\mathrm{SNR}_{\mathrm{out}}}. \tag{2.7}$$

The noise figure is a device-specific parameter.

EDFAs generally offer a higher gain and a lower noise figure than SOAs, making them advantageous for many applications [28, 30]. However, for IM/DD systems, which are applied for intra-datacenter links, the second optical window is attractive due to the minimal dispersion. Since such short-reach systems are cost-sensitive, the cheaper SOAs can be advantageous over fiber amplifiers.

2.1.3 Optical Filters

Optical filters can be used for different purposes in optical communication systems. Examples are reconfigurable optical add-drop multiplexers (ROADMs) to select or remove specific channels from the network, or filtering out one sideband of a signal to generate a single-sideband (SSB) signal [31, 32]. In this work, optical filters are applied to remove out-of-band noise before the reception of the optical signal. This way, the receiver detects less noise and the transmission system's performance can be improved. The filter bandwidth needs to be chosen carefully since a narrow filter bandwidth can result in inter-symbol interference (ISI) in the received signal.

2.2 Optical Fiber

The optical fiber is the transmission medium that is used for the communication systems considered in this work. It has a low loss and a huge usable bandwidth, making it an obvious choice for long-distance and high-speed data transmission [18]. The fiber type used in this work is the standard single mode fiber (SSMF). In contrast to multi mode fibers (MMFs) it only uses the fundamental mode of the fiber. The SSMF is a dispersive and nonlinear transmission medium. In the remainder of this section, the linear effects impairing signal transmission will be explained. Additionally, the main nonlinear effects will be described shortly. For a detailed description of the optical fiber and all the relevant effects, the reader is referred to [17, 33].

2.2.1 Linear Effects

The linear effects that affect a signal during transmission over a SSMF are loss, dispersion and polarization mode dispersion (PMD). Considering only loss and dispersion, the

Table 2.2: Typical values for the fiber loss and the dispersion parameter at selected wavelengths according to [17, 18].

Wavelength	α_{dB} [dB/km]	α [Np/m]	D [ps/(nm·km)]
1310 nm	0.4	$9.2 \cdot 10^{-5}$	0
1550 nm	0.2	$4.6 \cdot 10^{-5}$	17

frequency response of the optical SSMF is given by

$$H_{\mathrm{SSMF}}(\omega, L) = \exp\left(-\frac{\alpha L}{2}\right) \cdot \exp\Big(-j\beta(\omega)L\Big), \tag{2.8}$$

where ω is the angular frequency $\omega = 2\pi f$, L the fiber length, α the fiber loss in Np/m and $\beta(\omega)$ the phase constant.

The fiber loss is often described by the attenuation coefficient α_{dB}. Typical values for the wavelengths of 1310 nm and 1550 nm are summarized in Tab. 2.2. The wavelength 1550 nm experiences the lowest loss in an SSMF and is therefore used for long haul transmission [18].

The phase constant can be expressed by a Taylor series expansion around the carrier frequency ω_c [17]:

$$\beta(\omega) = \beta_0 + (\omega - \omega_c)\beta_1 + \frac{1}{2}(\omega - \omega_c)^2\beta_2 + \frac{1}{6}(\omega - \omega_c)^3\beta_3 + ... + \frac{1}{n!}(\omega - \omega_c)^n\beta_n. \tag{2.9}$$

Here, β_0 describes the phase constant at the carrier frequency [28], and β_1 is the reciprocal value of the group velocity [17], whereas the higher-order values describe the dispersive fiber effects. The parameter β_2 is the group-velocity dispersion parameter and gives insight into the pulse broadening during transmission over the fiber [17]. The third-order dispersion parameter β_3 is related to the dispersion slope. This parameter is especially relevant for WDM systems since the involved channels experience different amounts of dispersion [17]. If $\Delta\omega << \omega_c$, the terms of third and higher order in Eq. 2.9 can be neglected [33]. Note that for the equivalent baseband representation the carrier frequency ω_c is zero.

A common way to describe the amount of chromatic dispersion is the dispersion parameter D, which is related to the group velocity dispersion parameter by [17]

$$D = -\frac{2\pi c}{\lambda^2}\beta_2. \tag{2.10}$$

Here, c is the speed of light and λ the wavelength. Typical values for the dispersion

parameter are shown in Tab. 2.2. The wavelength of 1310 nm is the zero-dispersion wavelength for the SSMF, making it an interesting choice for non dispersion-managed transmission systems.

The dispersion slope can be described by the differential dispersion parameter, which is expressed as [17]

$$D_{\mathrm{S}} = \frac{dD}{d\lambda} = \left(\frac{2\pi c}{\lambda^2}\right)^2 \beta_3 + \frac{4\pi c}{\lambda^3}\beta_2. \tag{2.11}$$

Next to loss and dispersion, PMD affects the signal during transmission over the optical fiber. As mentioned before, the optical signal is composed of two orthogonal polarizations. In an ideal fiber with cylindrical core and constant diameter, the polarization states of all frequency components stay constant during transmission. However, in real fibers imperfections and non-uniform stress make the core deviate from a cylindrical shape. Due to this, the propagation constants differ for X- and Y-polarization. This phenomenon is called birefringence [33]. Random changes in fiber birefringence lead to randomly changing group velocities and consequently to pulse broadening. The pulse broadening caused by PMD can be described by the standard deviation of the time delay between the polarization components, which can be approximated as

$$\sigma_{\mathrm{T}} \approx D_{\mathrm{PMD}}\sqrt{L}. \tag{2.12}$$

D_{PMD} is the PMD parameter and typically lies in the range of 0.1-1 $\mathrm{ps}/\sqrt{\mathrm{km}}$ [33]. While the pulse broadening caused by PMD is typically relatively small compared to group-velocity dispersion, it can still be a limiting factor for high-speed transmissions over long distances [17].

2.2.2 Nonlinear Effects

As mentioned before, the optical fiber is a nonlinear transmission medium. The nonlinear effects impairing the signal are classified into two main groups: elastic and inelastic effects. Most of the elastic effects originate from a dependence of the refractive index on the intensity, which is known as the Kerr effect. Three relevant effects of this group are self-phase modulation (SPM), cross-phase modulation (XPM) and four-wave mixing (FWM). SPM occurs in a single channel without the impact of neighboring channels and refers to a phase shift induced on the electrical field during transmission over the fiber [33]. XPM describes a nonlinear phase shift induced by another field transmitted on a different wavelength or polarization [33]. FWM occurs, if three optical fields with different carrier frequencies propagate through the fiber simultaneously. In this case, a fourth field is

generated, which results in a power transfer and interchannel crosstalk, both leading to an impaired transmission performance [17].

The other group of nonlinear fiber effects is based on inelastic scattering. Two examples are given by stimulated Brillouin scattering (SBS) and stimulated Raman scattering (SRS). Both effects describe the scattering of a photon to a lower energy level, where the energy is transferred into a phonon [17]. SBS results from the interaction of photons and acoustic waves in the fiber and only occurs in backward direction. SRS describes the scattering by the interaction of photons with silica molecules and occurs in both directions [17].

In general, nonlinear fiber effects are increasing with growing transmit power and transmission distance. The lower the signal power and the shorter the link, the more linear fiber effects dominate. For intra-DCR transmission, nonlinear effects generally play a subordinate role. However, for a more profound understanding of these effects, the reader is referred to [33].

2.3 Transmission System Configurations

For optical transmission systems, different configurations for their transmitter and receiver hardware as well as the resulting modulation and detection capabilities are distinguished. The most simple approach is IM/DD, where only the intensity of the optical signal is modulated and the detection of the signal intensity is performed using a photodiode (PD). In contrast to that, coherent systems can use PolMux IQ modulation to modulate the amplitude and phase of X- and Y-polarizations of the optical signal. To enable the utilization of the full information after reception, a coherent receiver is necessary. This receiver concept requires significantly more hardware than a DD receiver, so an individual decision for the optimal configuration of a transmission system has to be made for each application. Due to the large difference in terms of modulation and detection capabilities between these two topologies, intermediate configurations, namely advanced DD systems, are interesting for certain applications. These systems can increase the degrees of freedom for data transmission and the impairment tolerance compared to IM/DD systems and require less hardware than full coherent systems.

In the following, the different configurations are shown and the advantages of each concept are highlighted.

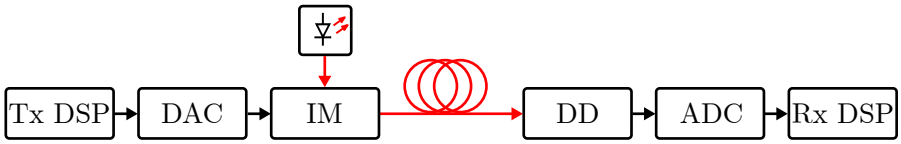

Figure 2.7: Configuration of a single-carrier IM/DD communication system.

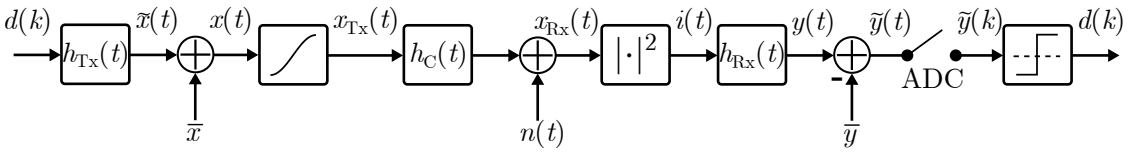

Figure 2.8: Mathematical model of an IM/DD system. The characteristics of transmitter, channel and receiver are described by the impulse responses $h_{\mathrm{Tx}}(t)$, $h_{\mathrm{C}}(t)$ and $h_{\mathrm{Rx}}(t)$, respectively.

2.3.1 Intensity-Modulation and Direct-Detection Systems

IM/DD systems offer a simple approach for transmitting data over the optical fiber. The basic configuration of such a communication system is depicted in Fig. 2.7. The transmitter front-end consists of digital-to-analog conversion and modulation. For the IM of the signal, either DML or external modulation can be applied, as described in Sec. 2.1.1. Due to the DD, the optical signal needs to be unipolar to be detected without ambiguities by the DD receiver. This can be ensured by adding a DC voltage to the information-carrying signal. The optical channel is given by the optical fiber and optional optical components. The receiver front-end contains a PD to detect the intensity of the incoming optical signal and an ADC.

This system can be mathematically described as shown in Fig. 2.8. The linear effects of the transmitter components are summarized in the impulse response $h_{\mathrm{Tx}}(t)$. On the resulting drive signal $\tilde{x}(t)$ a DC voltage $\overline{x}$ is added to ensure a unipolar optical signal at the output of the modulator. The IM is characterized by a nonlinear function, e.g. a cosine function in the case of an MZM. The effects of the optical channel are described by the impulse response $h_{\mathrm{C}}(t)$. Optical noise is added and the optical received signal $x_{\mathrm{Rx}}(t)$ results. The mathematical equivalent of the PD operation is the absolute square operation. The receiver impulse response $h_{\mathrm{Rx}}(t)$ is applied on the photocurrent $i(t)$ and the received analog signal $y(t)$ results, from which the DC part is removed before it is converted into the digital domain.

When the optical signal $x_{\mathrm{Tx}}(t)$ is transmitted via the optical channel and detected by the square law detector, the photocurrent (neglecting noise)

$$i(t) = |x_{\mathrm{Tx}}(t) * h_{\mathrm{C}}(t)|^2 \tag{2.13}$$

results. The transmitted signal can be separated into a DC component and a DC-free part, i.e.

$$x_{\mathrm{Tx}}(t) = \tilde{x}_{\mathrm{Tx}}(t) + \overline{x}_{\mathrm{Tx}}. \tag{2.14}$$

The photocurrent can be shown to be [34]

$$i(t) = \overline{x}_{\mathrm{Tx}}{}^2 \left|H_{\mathrm{C}}(0)\right|^2 + \left|\tilde{x}_{\mathrm{Tx}}(t) * h_{\mathrm{C}}(t)\right|^2 + 2\overline{x}_{\mathrm{Tx}} \Re\{H_{\mathrm{C}}(0)\} \tilde{x}_{\mathrm{Tx}}(t) * \mathcal{F}^{-1}\{\Re\{H_{\mathrm{C}}(f)\}\}, \tag{2.15}$$

where

$$\Re\{H_{\mathrm{C}}(f)\} = \exp\left(-\frac{\alpha L}{2}\right) \cdot \cos\left(2\pi^2 L \beta_2 f^2\right). \tag{2.16}$$

The first part of Eq. 2.15 is a DC component. The second part is referred to as signal-signal beat interference (SSBI) and distorts the signal. The third part contains the data signal and is distorted by the frequency response in Eq. 2.16. The cosine term in Eq. 2.16 describes the *power fading effect* that shapes the spectrum of the received signal [15, 35]. The power fading effect causes spectral nulls at the frequencies [15, 35, 36]

$$f_{\mathrm{null},n} = \pm\sqrt{\frac{1+2n}{4\pi|\beta_2|L}}, n \in \mathbb{N}_0. \tag{2.17}$$

Depending on the spectral extent of the signal $x(t)$, these nulls can distort the signal and cause ISI. The frequency response caused by chromatic dispersion (CD) in a DD system $H_{\mathrm{CD,DD}}(f)$ is visualized in Fig. 2.9 for 2 km and 5 km C-band transmission. The first spectral null for 2 km is observed at 42.85 GHz, while 5 km transmission causes the first null at 27.15 GHz. Even a single null inside the signal spectrum can cause severe distortion and sophisticated DSP is necessary to improve the performance in such scenarios.

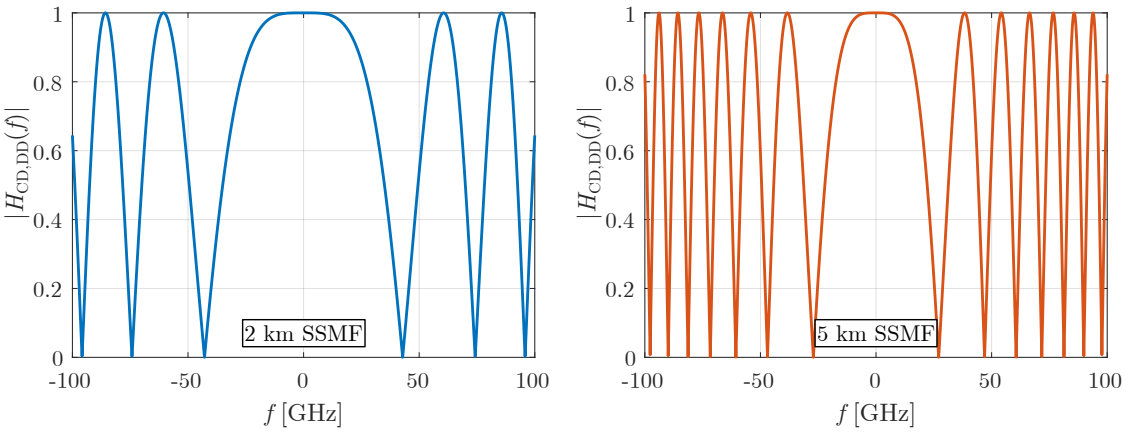

Figure 2.9: Visualization of the frequency response caused by CD in DD systems. A C-band transmission over 2 km and 5 km with a dispersion parameter of $D = 17\,\mathrm{ps/(nm \cdot km)}$ is assumed.

Frequency chirp induced during IM has an impact on the power fading effect. If transient chirp, occurring e.g. in EAMs according to Eq. 2.1, is considered, the frequency response changes to [15]

$$\Re\{H_{\mathrm{C}}(f)\} = \exp\left(-\frac{\alpha L}{2}\right) \cdot \sqrt{1+{\alpha_{\mathrm{C}}}^2}\cos\left(2\pi^2 L\beta_2 f^2 + \arctan(\alpha_{\mathrm{C}})\right). \tag{2.18}$$

According to that, the positions of the spectral nulls change to

$$f_{\mathrm{null,chirp},n} = \pm\sqrt{\frac{\frac{\pi}{2}(1+2n) - \arctan(\alpha_{\mathrm{C}})}{2\pi^2|\beta_2|L}}, n \in \mathbb{N}_0. \tag{2.19}$$

Chirp is therefore not necessarily impairing the transmission. If the linewidth enhancement factor α_C and the dispersion parameter D have opposing signs, the spectral null will be shifted towards higher frequencies compared to the chirp-less case. However, if the signs are the same, the impact of the power fading effect is increased.

2.3.2 Coherent Systems

Coherent detection allows the extraction of amplitude and phase information from the optical signal and additionally offers the capability to receive individual data on X- and Y-polarization. This allows more efficient usage of the electrical bandwidth of the transceiver components, as well as an increased optical spectral efficiency for WDM systems [33]. These advantages over DD systems, however, come at the cost of more complex hardware. Figure 2.10 a) shows the configuration of a coherent transmission system. At the transmitter, four DACs are necessary to convert the inphase and quadrature components of X- and Y-polarizations to the analog domain. Afterwards, a PolMux IQ modulator generates the optical signal. The signal is received by a PolMux coherent receiver (CR) before the digital signals for the four components are generated by four ADCs. The block diagram of a PolMux CR is depicted in Fig. 2.10 b). A PBS is used to split the optical signal into X- and Y-polarizations. The polarization components are fed into 90° optical hybrids and mixed with the signal of a local oscillator (LO). The outputs are detected by four pairs of balanced PDs.

The photocurrents can be expressed as [28, 37]

$$i_{XI}(t) = R_{\mathrm{PD}} \cdot |A_{\mathrm{LO}}| \cdot |x_{\mathrm{Rx},X}(t)| \cdot \cos\left(2\pi f_{\mathrm{IF}} t + \phi_X(t)\right), \tag{2.20a}$$
$$i_{XQ}(t) = R_{\mathrm{PD}} \cdot |A_{\mathrm{LO}}| \cdot |x_{\mathrm{Rx},X}(t)| \cdot \sin\left(2\pi f_{\mathrm{IF}} t + \phi_X(t)\right), \tag{2.20b}$$
$$i_{YI}(t) = R_{\mathrm{PD}} \cdot |A_{\mathrm{LO}}| \cdot |x_{\mathrm{Rx},Y}(t)| \cdot \cos\left(2\pi f_{\mathrm{IF}} t + \phi_Y(t)\right), \tag{2.20c}$$
$$i_{YQ}(t) = R_{\mathrm{PD}} \cdot |A_{\mathrm{LO}}| \cdot |x_{\mathrm{Rx},Y}(t)| \cdot \sin\left(2\pi f_{\mathrm{IF}} t + \phi_Y(t)\right). \tag{2.20d}$$

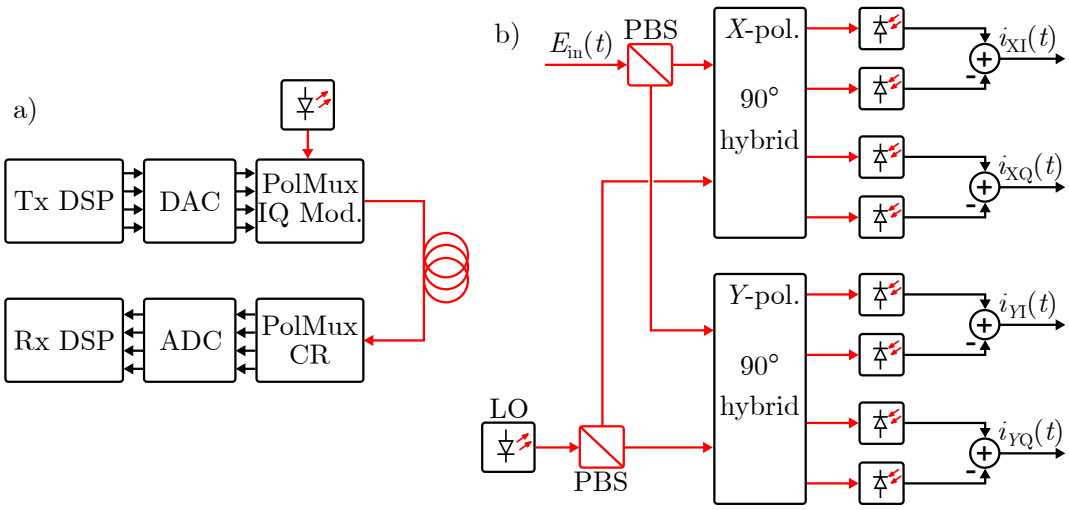

Figure 2.10: PolMux coherent transmission system. a) shows the general configuration and b) the block diagram of a PolMux CR.

Here, R_{PD} is the responsivity of the PDs, A_{LO} the amplitude of the LO output and f_{IF} the frequency difference between carrier and LO. Furthermore, $x_{\text{Rx},X}(t)$ and $x_{\text{Rx},Y}(t)$ denote the amplitudes of X- and Y-polarizations of the optical input signal, respectively, and $\phi_X(t)$ and $\phi_Y(t)$ the corresponding phases.

2.3.3 Advanced Direct-Detection Systems

In this work, the term *advanced DD systems* is used to summarize all transmission system configurations that lie in between IM/DD and coherent systems in terms of hardware complexity. A large group of these advanced DD systems are SCOH schemes. These systems can use different hardware configurations and have different detection capabilities but are all united in the idea that complex data (i.e. amplitude and phase) can be received without using an LO. This is generally achieved by transmitting the carrier along with the signal through the optical channel.

A group of these SCOH systems is based on the transmission of an SSB signal consisting of a DC-free signal $s(t)$ and sufficiently strong carrier tone E_0 at one side of the signal spectrum and the detection of the signal with a single PD. In this case, the photocurrent after square law detection by a PD can be expressed as [38]

$$i(t) = |E_0 + s(t)|^2 = |E_0|^2 + |s(t)|^2 + 2\Re\{E_0 \cdot s(t)\}. \tag{2.21}$$

The first term of Eq. 2.21 is a DC component that contains no relevant information and can be removed easily. The third term contains the desired linear copy of the signal

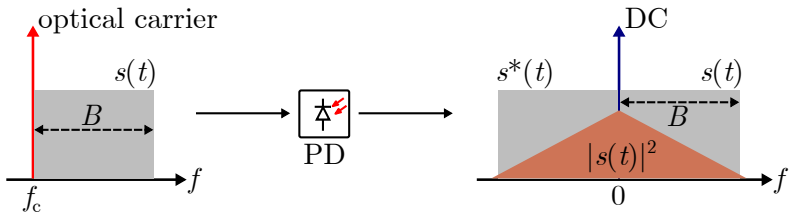

Figure 2.11: Illustration of a transmitted optical SSB signal and the resulting signal after detection with a PD.

$s(t)$. The second term is the SSBI that potentially impedes the reconstruction of the transmitted data. Eq. 2.21 is illustrated in Fig. 2.11. The SSBI overlays the useful signal spectrum and needs to be removed to ensure successful transmission. Approaches to reach this goal are described in Sec. 4.2.

Note that besides approaches based on SSB signals and detection with a single PD, other SCOH schemes exist that allow the detection of double-sideband (DSB) signals [39–41] or even PolMux [42–44]. However, these approaches are not considered in this work.

Another considered approach inside the class of advanced DD systems is the extension of conventional DD systems by the capability of applying EDC at the transmitter. This requires knowledge about the accumulated CD in the channel at the transmitter, which can be solved by estimation in the receiver DSP and a feedback channel to pass the information to the transmitter. Additionally, a system applying transmitter EDC requires a modulator that modulates the inphase and quadrature component of the optical signal, such as an IQ modulator or a dual-drive MZM. This is the case because CD is modeled by a complex transfer function and a real-valued signal convolved with this function results in a complex-valued signal. Details for this are described in Sec. 4.1.

2.4 Modulation Formats

The modulation formats used in this work are mostly restricted to conventional pulse amplitude modulation (PAM) and quadrature amplitude modulation (QAM). Note that bipolar PAM constellations are used during execution of the DSP, which in a strict sense should be referred to as bipolar ASK. However, the signals are converted to unipolar optical signals after adding a proper bias voltage before modulation. Therefore, the used modulation formats behave equally to conventional unipolar PAM. One exception from the conventional formats is given by PAM-6. While the standard PAM formats allow mapping of an integer number of bits on each symbol, this is not possible for this format. Instead, the concept of multidimensional constellations is applied to map five bits on

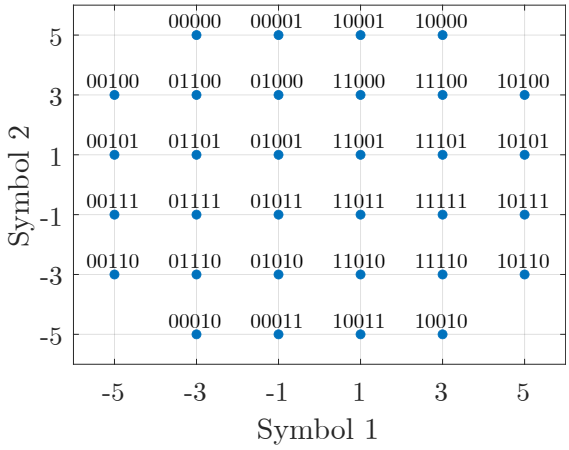

Figure 2.12: Constellation and mapping used for the PAM-6 modulation format.

two consecutive symbols. For a detailed description of the concept of multidimensional constellations, the reader is referred to [37]. The PAM-6 format forms an intermediate stage between PAM-4 and PAM-8 in terms of bandwidth demand and SNR requirement. Therefore, it can be an interesting option for the high-rate systems that are investigated in this work. The PAM-6 format can theoretically carry $\log_2(6) = 2.585$ bits/symbol. However, this would require a complex encoding and decoding concept, so a suboptimal solution of mapping five bits and two consecutive symbols is preferred [45, 46]. A possible constellation for this is shown in Fig. 2.12. The constellation corresponds to that of the 32-QAM format, but instead of using the inphase and quadrature components as two dimensions, the time is used to allow a two-dimensional mapping. Since Gray mapping is impossible for the given constellation, a pseudo-Gray mapping with a Gray penalty of 1.1667 is used [46].

2.5 Forward Error Correction

For a practical optical communication system, the requirement for the bit error ratio (BER) lies in the order of 10^{-15}. To reach such regions, FEC needs to be applied. However, as such low BERs are not accessible through simulations due to the enormous number of bits that would need to be transmitted, FEC limits are assumed. These limits are based on the correction capabilities of specific codes. If a pre-FEC BER below such a limit is reached, it is assumed that the corresponding code with a certain overhead can correct the errors up to the desired BER. This assumption is considered justifiable for hard decision (HD) FEC codes, while it can be inaccurate for soft decision (SD) FEC codes [47, 48]. For the short-reach transmission scenarios considered in this work, the simpler HD FEC codes are typically preferred. For recent standards, the so-called KP4-FEC (Reed Solomon

code) with a pre-FEC BER of $2 \cdot 10^{-4}$ was used [49]. Due to the increased challenges by bandwidth limitation and fiber effects, stronger codes are considered for 800 Gb/s systems [5]. The coding gain by the KP4-FEC can be increased by concatenation with a second code. The decision for a specific code has not been made, but a proposal for FR scenario is shown in [50, 51]. The KP4 code is used as the outer code and a zipper code as the inner code, so that a pre-FEC BER of $2 \cdot 10^{-3}$ is required. This limit is considered for the remainder of this work. The overhead for this code is approx. 12 %.

Chapter 3

Digital Signal Processing for IM/DD Systems

DSP is a simple and flexible way to improve a system's performance. Several impairments that affect the signal during transmission can be mitigated or removed by transmitter and receiver DSP. As described in Chapter 2, the transmission through IM/DD systems suffers from bandwidth limitations, CD and nonlinearities of the fiber and components. Specific algorithms can tackle one or more of these impairments.

The DSP used in this work builds up on top of a basic DSP stack. These schemes are used for all simulations and experiments and additional schemes are supplemented to improve the performance. The basic DSP stack is shown in Fig. 3.1. In the transmitter DSP a pseudo-random binary sequence (PRBS) is generated. This sequence is deterministically generated but emulates the properties of real random data. The binary data is mapped on PAM symbols. In the likely case that the symbol rate is not equal to the DAC sampling rate, the sequence is re-sampled to match the latter. Then, the pulse is shaped, which is done in the most cases by applying a root-raised cosine (RRC) shape to the signal. A few exemplary pulse shapes are depicted in Fig. 3.2. While an RRC with a small roll-off factor (ROF) of $\beta_{\mathrm{ro}} = 0.05$ only slightly increases the spectral width of the signal, a high ROF of $\beta_{\mathrm{ro}} = 1$ distributes the power over twice the frequency range compared to the initial signal. As an alternative to an RRC shape, a raised cosine (RC) or higher roots of the RC can be used. The higher the order of the root, the more energy is shifted towards higher frequencies.

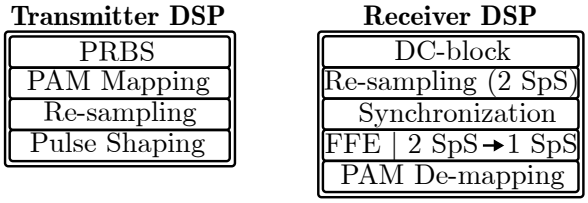

Figure 3.1: Basic transmitter and receiver DSP steps.

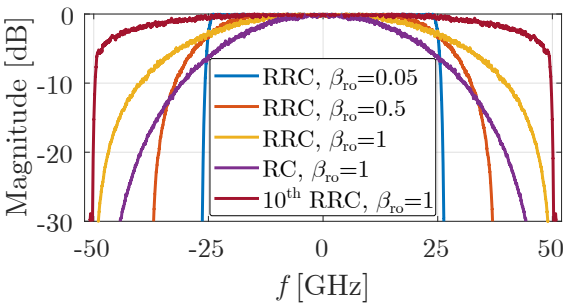

Figure 3.2: Visualization of different pulse shapes. A 50 GBd PAM-4 signal, up-sampled to a rate of 120 GS/s, is shown.

In the receiver DSP, the DC part of the signal is removed before it is re-sampled to two samples per symbol (SpS). Note that processing of the signal at one SpS is also possible, however, this can lead to a decreased performance in case the sampling phase is not ideally matched. The signal is synchronized with the transmitted symbols and feed-forward equalization (FFE) (cf. Sec. 3.2.1) is performed. Finally, the symbols are de-mapped.

3.1 Transmitter Side

It can be advantageous to perform DSP steps at the transmitter side rather than at the receiver. First of all, the signal before transmission is noise-free, so that strong amplifications of signal components can be applied without suffering from noise-enhancement. Additionally, all transmitted symbols are known, which allows avoiding symbol decisions that are prone to errors. However, most transmitter DSP schemes require channel information to prepare the signal for transmission. Different transmitter DSP approaches are described in the following part.

3.1.1 Partial Response Techniques

A well-known technique to improve the transmission performance in bandwidth constrained systems is partial response (PR) signaling. It is based on the application of a partial response filter that introduces a controlled amount of ISI to the signal. This way, the properties of the transmitted signal can be adapted to the channel properties [52, 53]. The transmitted symbol sequence $d(k)$ has a flat spectrum and is transformed into a PR sequence $c_{\mathrm{PR}}(k)$ with different spectral characteristics. The transformation into the PR sequence is done by a simple finite impulse response (FIR) filter with only a few coefficients [54]. The structure of PR filters of length two is shown in Fig. 3.3. The

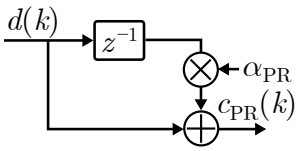

Figure 3.3: Structure of partial response filters of length two.

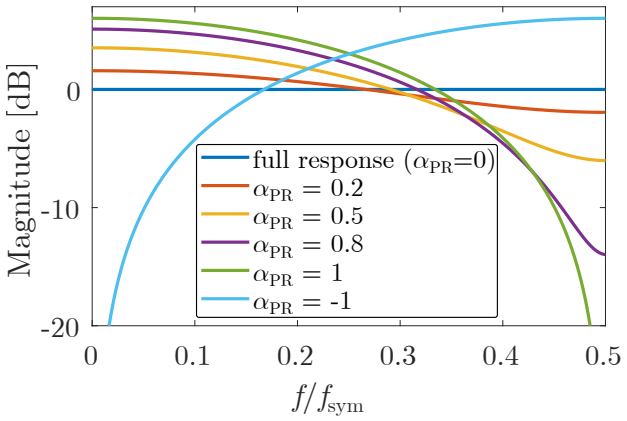

Figure 3.4: Transfer functions of selected partial response filters of length two. The transfer function of the filters is given by $1 + \alpha_{\mathrm{PR}} z^{-1}$.

transfer function of this two-tap FIR filter is given by

$$H_{\mathrm{PR}} = 1 + \alpha_{\mathrm{PR}} z^{-1}. \tag{3.1}$$

The transfer functions of selected PR filters of length two are visualized in Fig. 3.4, where the frequency is normalized on the symbol rate f_{sym}. Positive values for α_{PR} lead to an enhancement of the low frequencies and a suppression of higher frequencies of the signal. The higher α_{PR} is chosen, the stronger this effect gets. If a negative value α_{PR} is applied, the characteristics for the PR filter are inverted, i.e. low frequencies are suppressed and high frequencies are enhanced. Since the components of an optical transmission system typically show a lowpass characteristic and strongly bandwidth-limited systems are investigated in this work, positive values for α_{PR} are of interest [52].

In a bandwidth-limited transmission system, the PR filter does not necessarily need to be applied at the transmitter DSP, but it can also be assumed that the channel automatically applies this characteristic to the signal. In this case, the equalizer in the receiver DSP targets the PR instead of the full response [46, 55].

To retrieve the symbol sequence afterwards, different options exist. These options are explained based on the example of the duobinary (DB) response, which shows desirable properties for the systems investigated in this work.

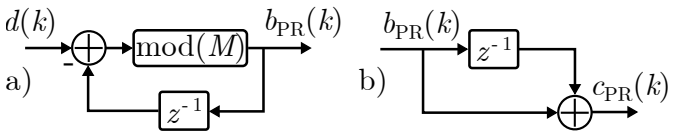

Figure 3.5: Structure of the DB pre-coder a) and coder b).

The DB code is characterized by the transfer function $H_{\mathrm{DB}} = 1 + z^{-1}$, which is shown in Fig. 3.4. The encoded sequence $c_{\mathrm{PR}}(k)$ is obtained as the sum of the current and previous symbols $d(k)$ and $d(k-1)$. Therefore, the relationship $\hat{d}(k) = c_{\mathrm{PR}}(k) - \hat{d}(k-1)$, where $\hat{d}(k)$ is the received symbol sequence, can be utilized to retrieve the initial symbol sequence [54]. However, each decision is dependent on the outcome of the previous decision, which leads to the propagation of errors. Therefore, this approach does not lead to the desired performance. Alternatively, the remaining ISI after equalization can be removed by Viterbi equalization, which is explained in Sec. 3.2.4.

A simpler reconstruction of the symbol sequence $d(k)$ can be enabled by applying pre-coding at the transmitter. The structure of the pre-coder for the DB code is shown in Fig. 3.5 a). The pre-coded sequence $b_{\mathrm{PR}}(k)$ has the same distribution and spectrum as the initial sequence $d(k)$. As visible in Fig. 3.5 a), the pre-coded sequence is obtained as $b_{\mathrm{PR}}(k) = (d(k) - b_{\mathrm{PR}}(k-1))\mathrm{mod}(M)$. If the DB coder is applied on the pre-coded sequence,

$$c_{\mathrm{PR}}(k) = b_{\mathrm{PR}}(k) + b_{\mathrm{PR}}(k-1) = (d(k) - b_{\mathrm{PR}}(k-1))\mathrm{mod}(M) + b_{\mathrm{PR}}(k-1) \tag{3.2}$$

results. Applying the $\mathrm{mod}(M)$ operation on both sides of Eq. 3.2 leads to

$$(c_{\mathrm{PR}}(k))\mathrm{mod}(M) = ((d(k) - b_{\mathrm{PR}}(k-1))\mathrm{mod}(M) + b_{\mathrm{PR}}(k-1))\,\mathrm{mod}(M) \tag{3.3}$$

$$= (d(k) - b_{\mathrm{PR}}(k-1) + b_{\mathrm{PR}}(k-1))\,\mathrm{mod}(M) \tag{3.4}$$

and therefore to

$$d(k) = (c_{\mathrm{PR}}(k))\mathrm{mod}(M), \tag{3.5}$$

as $d(k)$ already is inside the interval $[0, M]$. The symbol sequence $d(k)$ can thus be reconstructed from $c_{\mathrm{PR}}(k)$ without the usage of previous decisions and the error propagation problem is solved. Figure 3.6 shows the probability density function of a DB encoded unipolar PAM-4 sequence. If the modulo 4 operation is applied for decoding, the amplitudes shift as marked by the arrows and the initial unipolar PAM constellation is obtained.

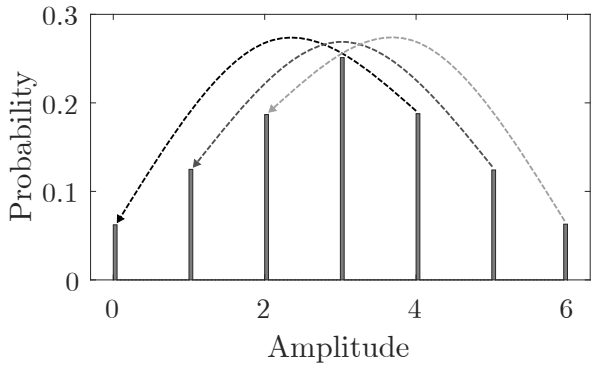

Figure 3.6: Probability density function of a unipolar PAM-4 constellation encoded by the DB coder. The arrows mark the impact of the modulo 4 operation, that can be used for decoding.

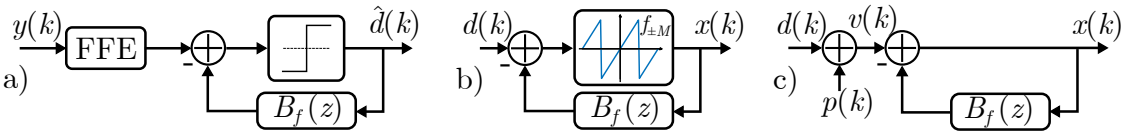

Figure 3.7: Structure of decision-feedback equalization and THP. a) shows the DFE structure, b) the THP structure and c) the linearized THP.

In strongly bandwidth-limited systems, it can be advantageous to apply Viterbi equalization for the retrieval of the symbol sequence and additionally do DB pre-coding at the transmitter. The Viterbi equalization contributes to an improved performance by exploiting the known ISI in the signal, in addition the DB pre-coding can reduce error bursts [56, 57]. The explanation for this advantage lies in the quasi-catastrophic behavior of the trellis. For each error event, long sequences of errors can result, if no pre-coding is applied. However, pre-coding reduces the number of errors for all likely error events to two [56, 57].

3.1.2 Tomlinson-Harashima Pre-Coding

The concept of Tomlinson-Harashima pre-coding (THP) has been proposed in the 1970s by Tomlinson [58] as well as Harashima and Moyakawa [59]. Despite it being known for this long time, it recently gained a lot of interest in optical communications, especially for short-reach applications [60–66]. THP describes the approach of shifting decision-feedback equalization (DFE) from the receiver side to the transmitter side. This solution can be advantageous because DFE suffers from error propagation. This phenomenon occurs because the current output of DFE is dependent on the decisions on previous symbols. Therefore, wrong decisions not only lead to an error on the current symbol but also affect the following symbols negatively. At the transmitter, the symbols are known, so that this effect does not occur. The general structure of THP is shown in Fig. 3.7 b). The structure is equal to that of DFE (Fig. 3.7 a)), except that the decision device is replaced

by a modulo operation that can be described as

$$f_{\pm M}(s) = (s + M)\mathrm{mod}(2M) - M \tag{3.6}$$

for bipolar PAM constellations or as mod$(2M)$ for unipolar PAM constellations at the THP input. The parameter M must be chosen according to the modulation format used ($M = 4$ in case of PAM-4). The data sequence $d(k)$ is filtered by the transfer function $B_f(z)$. This transfer function cannot be calculated at the transmitter as it requires channel knowledge. Therefore, a feedback channel from the receiver to the transmitter is necessary.

The structure shown in Fig. 3.7 b) can also be expressed by a linearized description shown in Fig. 3.7 c). The sequence $p(k) \in 2M \cdot \mathbb{Z}$, where $\mathbb{Z}$ represents the integers, is called pre-coding sequence. It is added to the data sequence and describes the effect of the modulo operation. The resulting sequence $v(k)$ is called effective data sequence (EDS). This sequence is what the receiver side equalizer is aiming at, so the training symbols are symbols coming from this sequence. After the feedback part, finally, the output symbols $x(k)$ are known. Mathematically, the linearized THP can be written as

$$x(k) = d(k) + p(k) - \sum_{n=0}^{N} b(n) \cdot x(k - n). \tag{3.7}$$

The distributions of $d(k)$, $x(k)$ and $v(k)$ are shown in histograms in Fig. 3.8 for PAM-4 symbols. In the initial PAM-4 sequence, all four symbol levels are equally probable. After THP, the resulting sequence $x(k)$ is approximately uniformly distributed in the interval $[-M, M)$ (Fig. 3.8 b)). The equalizer in the receiver DSP targets the EDS and an exemplary FFE output sequence is shown in Fig. 3.8 c). Note that the number of amplitude levels in the EDS varies depending on the THP coefficients. For small coefficient values, i.e. a flatter frequency response, the number of amplitude levels does not significantly increase compared to the input constellation. On the other hand, large THP coefficient values can lead to a doubling of the number of amplitude levels.

Although the problem of error propagation in DFE is avoided in THP, it does not unconditionally lead to better results, if THP is used instead of DFE. One reason for that is the so-called pre-coding loss, which describes a power penalty that is caused by the increased variance of the transmitted sequence $x(k)$ compared to the initial sequence $d(k)$. For PAM-M signals, it can be described as

$$\gamma_p = \frac{E\{|x(k)|^2\}}{E\{|d(k)|^2\}} = \frac{M^2}{M^2 - 1}. \tag{3.8}$$

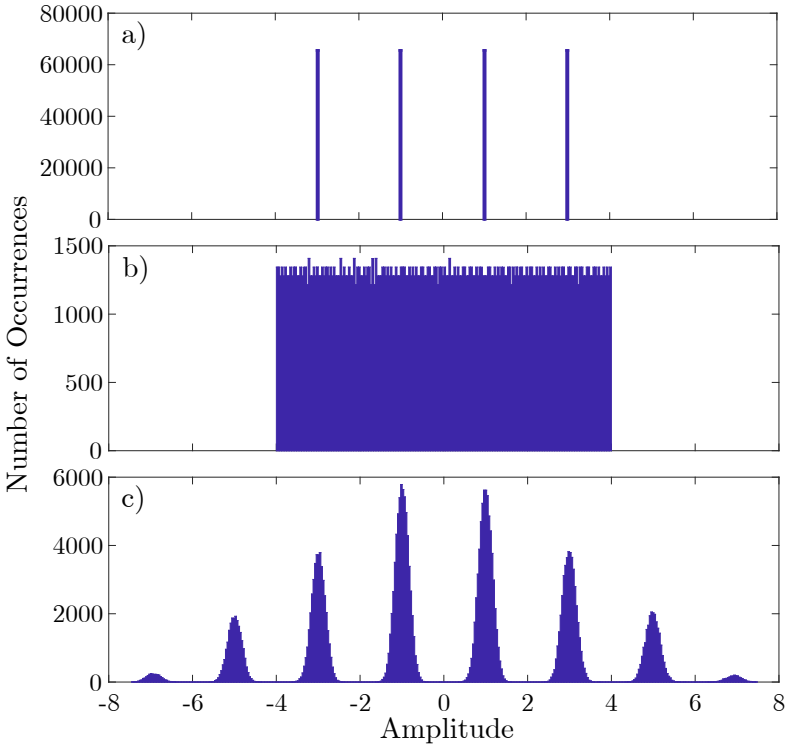

Figure 3.8: Histograms of a) the PAM-4 sequence $d(k)$, b) the THP output sequence $x(k)$ and c) the EDS $v(k)$.

Table 3.1: Pre-coding loss for selected PAM formats.

M	2	4	8
γ_p [dB]	1.25	0.28	0.07

The penalties for different modulation formats are summarized in Tab. 3.1. Apparently, the loss is significantly larger for small constellations and the impact gets negligible for high-order constellations.

Next to the pre-coding loss, a slight disadvantage of THP over DFE is the increased number of nearest neighbors for the received symbols. While in the case of PAM-4 only the symbols with amplitudes $\{\pm 1\}$ have two nearest neighbors and the other two symbols only one, in the effective data sequence each symbol has two nearest neighbors. This also holds for the outermost symbols because of the modulo operation. However, the spacing of the signal points and the noise variance are unchanged, so the effect is not significant.

At the receiver side, the modulo operation needs to be undone and the symbol decision needs to be performed. Both steps need to be conducted after equalization. The order of these two steps can be changed. Either, the modulo operation is applied on the estimate

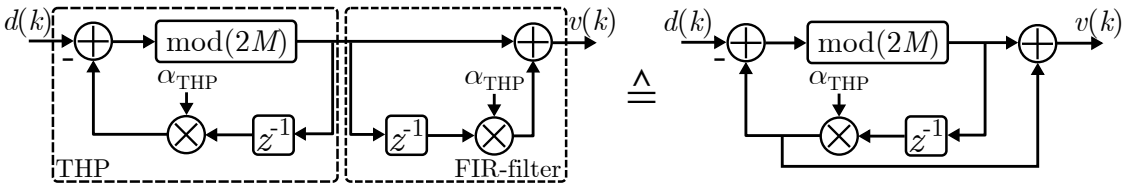

Figure 3.9: Block diagram of 1-coefficient THP with an FIR filter and combined structure.

of the effective data sequence first and the decision is done on the resulting PAM symbols, or the decision is done first on the effective data sequence and the modulo operation is applied afterwards. In the following simulations and experiments, the option of applying the modulo operation first is used.
For additional information on THP, the reader is referred to [36] and [67].

In combination with bandwidth pre-compensation (cf. Sec. 3.1.4) it can be advantageous to modify THP by placing an FIR filter behind the pre-coder [68]. This filter uses the same coefficients used in the THP feedback filter. This THP-FIR structure is shown in Fig. 3.9 for the example of 1-coefficient THP. As shown on the right part, a combined structure can be formed avoiding additional multiplications by the filter. The idea behind this combination is the observation, that conventional THP followed by bandwidth pre-compensation targets a flat received spectrum. The EDS, which is the target for the receiver equalizer, however, strongly deviates from a flat response in bandwidth-limited systems. Therefore, the received signal and the equalizer target do not match in such scenarios. An FIR filter after THP changes the output to the EDS $v(k)$. This way, the mismatch can be corrected and the received signal spectrum matches the equalizer target sequence.

3.1.3 Arccos-based Nonlinear Mapping

The transmission performance in IM/DD systems is impaired by the nonlinear characteristics of the modulator and the square-law detection by the PD. As explained in Sec. 2.1.1, the extent of the nonlinear behavior is dependent on the bias voltage and the voltage swing of the incoming radio frequency (RF) signal. If the bias voltage is chosen to be in the linear region of the characteristic and a low RF voltage swing is used, the nonlinear impairments induced by the modulator can be minimized. However, allowing a higher voltage swing increases the distance between the signal levels in the resulting optical signal, so that these levels can be distinguished better after reception and the performance can be improved under the presence of noise. Therefore, the trade-off between nonlinear behavior and noise tolerance has to be optimized to obtain the best possible performance.

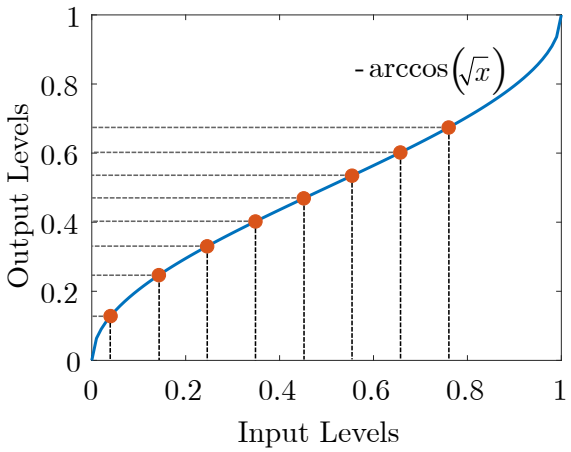

Figure 3.10: Exemplary generation of a non-regular PAM-8 constellation based on a $-\arccos(\sqrt{x})$ function.

The MZM's power characteristic can be described as a squared cosine function. This results in a non-regular spacing of the amplitude levels in the optical output signal (Fig. 2.5). As a countermeasure, the spacing between the PAM symbol levels can be adapted to be non-regular. More precisely, the MZM characteristic needs to be inverted using an $-\arccos(\sqrt{x})$ function. For exact mitigation of the nonlinear effect, the position of the bias point and the voltage swing need to be matched. This is done by scaling the $-\arccos(\sqrt{x})$ function into an interval [0,1] and scaling the initial PAM sequence in the range corresponding to desired bias and voltage swing. This is exemplarily shown for a PAM-8 constellation in Fig. 3.10, where a bias point below the quadrature point and a relatively large voltage swing are chosen. As a result, the spacings between the output levels differ significantly. The non-regular output constellation is re-scaled to be further processed.

Conventional PAM-8 is compared to a non-regular constellation based on 70 GBd experimental data in Fig. 3.11. The non-regular constellation in Fig. 3.11 d) is optimized for a bias point below the quadrature point and a high voltage swing. According to that, the spacing between the lower amplitude levels is significantly increased in order to compensate for the nonlinearities. Figure 3.11 b) and c) show the histograms for the conventional PAM-8 format after receiver linear FFE and VNLE of third order, respectively. The same cases are shown for the non-regular constellation in subfigures e) and f). The histogram in Fig. 3.11 b) shows that the lower signal levels are subject to nonlinearities. If VNLE is applied (Fig. 3.11 c), the positions of the signal levels can be corrected, however, the lower levels are still subject to more errors. The histograms in Fig. 3.11 e) and f) show the effect of the non-regular constellation. After linear FFE, the level spacing is much more uniform than for the conventional PAM-8 constellation. After

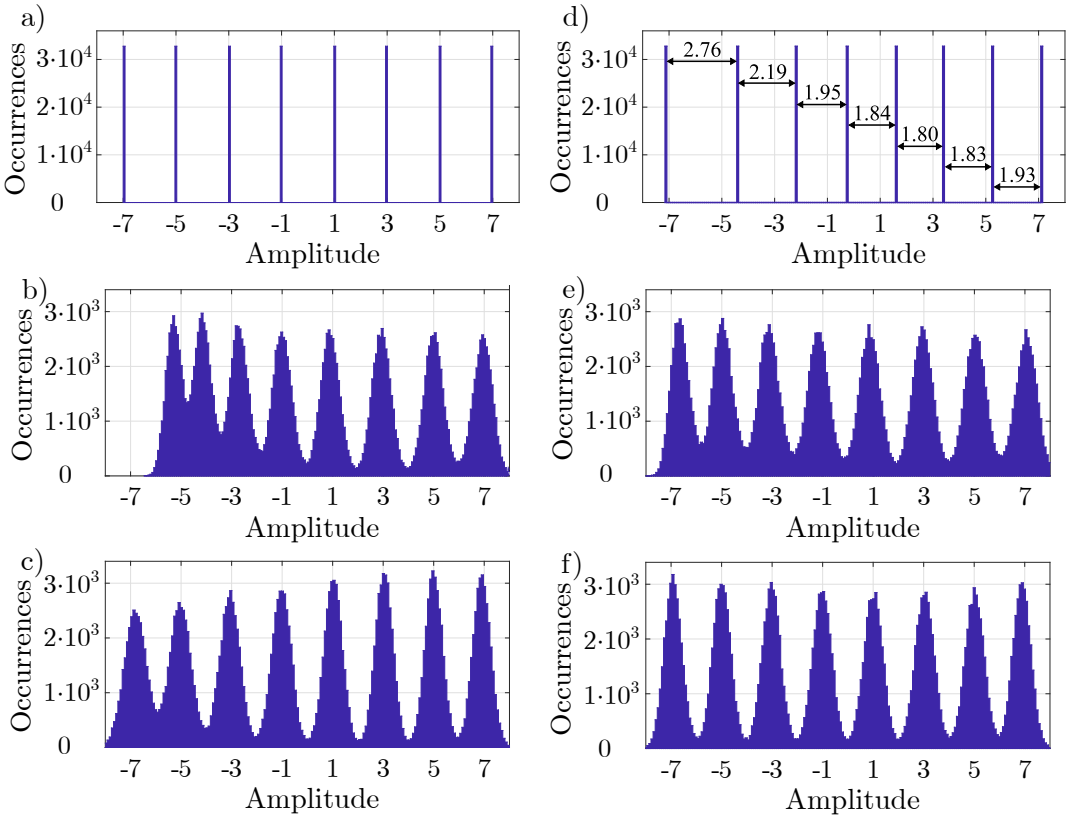

Figure 3.11: Exemplary comparison of regular and non-regular PAM-8 constellation. a) shows the regular constellation, b) the histogram of the signal after linear FFE and c) after VNLE. d) shows the modified non-regular constellation and e) and f) the received signal distributions after linear FFE and VNLE.

VNLE the quality is even better and a clear improvement compared to Fig. 3.11 c) can be observed.

3.1.4 Bandwidth Pre-Compensation

Besides CD induced power fading, bandwidth limitations of the transmitter and receiver components are a major restriction for increasing symbol rates. The ISI resulting from bandwidth limitations can be mitigated in the receiver DSP, however, this might lead to suboptimal performance due to equalizer noise enhancement (cf. Sec. 3.2). Hence, it is common to compensate a part of the bandwidth limitations using pre-compensation in the transmitter DSP [69–72].

To pre-compensate the bandwidth limitations, a frequency response containing the characteristics of the transmitter and receiver components has to be available. Different approaches to obtain this exist. For the majority of the results shown in this work, the

frequency response is measured by transmitting a multi-tone signal through the optical back-to-back configuration. By comparing transmitted and received signals, the attenuation on the different frequency components caused by the setup can be evaluated. A different approach used for a few measurements is the calculation of FIR filter coefficients using the Burg algorithm (cf. Sec. 3.2.3). The coefficients can be calculated based on the received signal after transmitting a signal with a flat spectrum over the optical back-to-back channel.

In case of strong bandwidth limitations, it might be suboptimal to apply the full inverse bandwidth characteristic in the pre-compensation. The reason for this is twofold: first, the peak-to-average power ratio (PAPR) of the signal is increased by strong pre-compensation. As the quantization for the digital-to-analog conversion only allows a limited resolution, this can lead to increased quantization noise. Second, certain frequency components are significantly amplified compared to other parts of the signal. Considering the limited linear range for the modulation of the electrical signal on the optical carrier, this is equal to an attenuation of the unamplified frequency components and leads to performance mitigation. Therefore, the frequency response used for pre-compensation is clipped at a certain amplification in this work. This is done with respect to the overall transmission performance to find an optimal trade-off between the compensation of bandwidth limitations, the increase of quantization noise and the relative attenuation of signal components.

3.2 Receiver Side

The application of DSP after reception of the signal allows the mitigation of several impairments induced during transmission. Linear and nonlinear effects of the channel can be estimated and inverted. After the signal is detected by a PD, it is re-sampled to two SpS for all results shown in this work. Note that processing at one SpS saves computational complexity and does not necessarily lead to a decreased performance, however, it requires an exact sampling phase correction [73]. Before applying the remaining DSP steps, the signal frame is synchronized with the training symbols using a cross-correlation. In the following, several schemes for receiver DSP are introduced.

3.2.1 Feed-Forward Equalization

FFE is a basic step used for all results shown in this work. It is based on an FIR filter with a number of N_{FFE} coefficients. This number of coefficients should be chosen to be high enough to compensate for the ISI induced on the signal during transmission, i.e. it should match the length of the impulse response of the system. The experiments shown

in this work are based on a discrete setup of several components and connectors, which results in reflections. To compensate for these reflections, the number of FFE coefficients is typically chosen to be significantly higher than the length of the system's impulse response would be without these effects.

The relation between FFE input $x_{\text{in}}(k)$ and output $x_{\text{out}}(k)$ can be expressed as

$$x_{\text{out}}(k) = h_{\text{DC}} + \sum_{n=0}^{N_{\text{FFE}}-1} h(n) \cdot x_{\text{in}}(k-n), \tag{3.9}$$

where h contains the equalizer coefficients. The coefficient h_{DC} is responsible for the DC part of the signal. It is often omitted in FFEs, but it can lead to improved performance, even if the equalizer input is already DC-free and is especially relevant, if asymmetric constellations are used [73].

The channel to be equalized is generally unknown. Therefore, the impulse response has to be estimated for an effective equalization. A popular algorithm for this is based on the minimum mean square error (MMSE) criterion with the cost function [67, 74]

$$F_{\text{MSE}} = \text{E}\left\{|x_{\text{out}}(k) - x_{\text{in}}(k)|^2\right\} \rightarrow \min_{\mathbf{h}}, \tag{3.10}$$

where $\mathbf{h}$ is a vector containing all FFE coefficients. The estimation is based on training symbols $d_t(k)$, i.e. a part of the transmitted symbols that is known at the receiver. Based on these, the coefficients can be calculated by the so-called Wiener-Hopf equation as

$$\mathbf{h}_{\text{MMSE}} = \mathbf{R}_{xx}^{-1} \cdot \mathbf{r}_{xd}. \tag{3.11}$$

Here, $\mathbf{R}_{xx}$ is the auto-correlation matrix of the received training symbols, and $\mathbf{r}_{xd}$ is the cross-correlation vector of received training symbols and the actual training symbols [74, 75].

In time-variant systems, it can be advantageous to adapt the coefficients during operation. For this, several adaptive algorithms exist, of which the least mean squares (LMS) algorithm is the most considered one. This algorithm is a robust and low-complexity approach to finding an approximate solution to the Wiener-Hopf equation [76]. In contrast to the MMSE solution, it does not require knowledge about the auto-correlation matrix $\mathbf{R}_{xx}$ and the cross-correlation vector $\mathbf{r}_{xd}$, nor a matrix inversion is required. The LMS algorithm iteratively approaches the optimal solution. The current coefficients are updated

based on the derivation of the MMSE cost function [74]:

$$h_{\mathrm{LMS}}(k+1) = h_{\mathrm{LMS}}(k) - \mu \frac{\partial F_{\mathrm{MSE}}}{\partial h_{\mathrm{LMS}}^{\mathrm{H}}(k)}. \tag{3.12}$$

The parameter μ is the step size that controls the speed and accuracy of convergence. While a large μ leads to fast convergence and a high residual error, a small value leads to slower convergence but a more exact result. The superscript H denotes the Hermitian transposition.

The most common expression for the LMS algorithm is based on the instantaneous error

$$\epsilon(k) = x_{\mathrm{out}}(k) - \hat{x}_{\mathrm{out}}(k). \tag{3.13}$$

For the adaptation of the coefficients, the rule

$$h_{\mathrm{LMS}}(k+1) = h_{\mathrm{LMS}}(k) - \mu \epsilon(k) x_{\mathrm{in}}^{*}(k) \tag{3.14}$$

results [74]. This principle is known as decision-directed LMS.

A problem of the LMS algorithm is the dependence of the coefficient updates on the magnitude of the input vector [75]. This motivates the normalized LMS that changes the adaptation rule to [75, 77]

$$h_{\mathrm{LMS}}(k+1) = h_{\mathrm{LMS}}(k) - \overline{\mu} \epsilon(k) \frac{x_{\mathrm{in}}^{*}(k)}{x_{\mathrm{in}}^{\mathrm{H}}(k) x_{\mathrm{in}}(k)}. \tag{3.15}$$

This normalization of the input vector also requires a change of the step size. For the normalized LMS a step size of $\overline{\mu} = 1$ typically leads to a good performance, which makes the parameter optimization for this algorithm simpler.

Note that it might be advantageous to initialize the FFE coefficients in a training stage and track the changes during operation by adaptive coefficient updates. For the initialization, both, the MMSE criterion or the LMS algorithm based on training symbols, can be applied. For the LMS algorithm in training mode, the hard decision $\hat{x}_{\mathrm{out}}(k)$ in Eq. 3.13 needs to be replaced by the respective training symbol $d_t(k)$.

In Fig. 3.12, the properties of the FFE and the resulting signal are exemplarily illustrated. For this example, a channel with an impulse response of $h_{\mathrm{Ch}} = [0.4\,1\,0.4]$ is assumed. The incoming signal is impaired by weak additive white Gaussian noise (AWGN) so that an

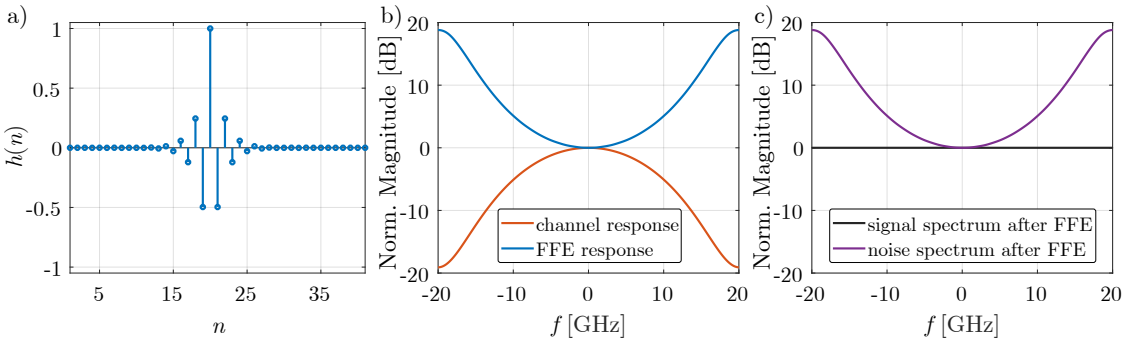

Figure 3.12: Illustration of a) FFE coefficients, b) normalized FFE and channel frequency response and c) normalized signal and noise spectrum after FFE.

SNR of 50 dB results. Figure 3.12 a) shows the FFE coefficients $\mathbf{h}$ for this example. The FFE uses 41 coefficients, but only a few central coefficients have a significant amplitude. The central coefficient is the strongest and the amplitude of the neighboring coefficients decreases with distance to the center. Comparing the frequency responses of the channel and the FFE (Fig. 3.12 b)), it can be observed that the channel is inverted. Note that an exact inversion of the channel corresponds to a zero-forcing equalizer and an optimization based on the MMSE criterion can deviate from this. While the overall signal after FFE shows the desired flat spectrum, the noise that was added after the channel response, is enhanced according to the FFE frequency response. This noise enhancement can significantly impair the transmission quality in systems with strong lowpass characteristics. This characteristic is common in high-rate IM/DD systems, due to the stringent bandwidth limitations of the components and the CD induced power fading effect (see Sec. 2.3.1). Several DSP approaches to overcome this issue exist and are described in this work.

Volterra Nonlinear Equalization

A nonlinear generalization of linear filters is given by polynomial filters based on the Volterra series. The Volterra series can be described as a Taylor series with memory and is the basis for VNLE. Assuming discrete real input and output sequences $x_{\mathrm{in}}(k)$ and $x_{\mathrm{out}}(k)$, and a discrete-time causal nonlinear system, the Volterra series expansion can be

defined as [75, 78, 79]

$$\begin{aligned} x_{\text{out}}(k) = h_{\text{DC}} + \sum_{n_1=0}^{\infty} h_1(n_1)x_{\text{in}}(k-n_1) + \\ \sum_{n_1=0}^{\infty}\sum_{n_2=0}^{\infty} h_2(n_1,n_2)x_{\text{in}}(k-n_1)x_{\text{in}}(k-n_2) + ... + \\ \sum_{n_1=0}^{\infty}\sum_{n_2=0}^{\infty}...\sum_{n_N=0}^{\infty} h_N(n_1,n_2,...,n_N)x_{\text{in}}(k-n_1)x_{\text{in}}(k-n_2)...x_{\text{in}}(k-n_N) + ..., \end{aligned} \tag{3.16}$$

where h_N is the N^{th} Volterra kernel. The Volterra series is not applicable in practice, since it is strictly infinite. Two restrictions need to be made in order to use it for equalization: The order N needs to be limited and the number of terms for each order needs to be a finite number.

In optical communication systems, it is typical to apply VNLE with kernels up to the third order [80–85]. This can be done because the relevant fiber nonlinearities are included in the third-order kernels. However, for the short-reach systems considered in this work, nonlinearities due to the modulator characteristic combined with the square-law detection play a dominant role. As described in Sec. 2.1.1, these nonlinearities can contain terms of different orders depending on the bias point. The impact of the terms, however, shrinks with growing order, so that a restriction of the VNLE to the third order results in a fair trade-off between performance and complexity.

The Volterra kernels are symmetric [73], so only coefficients with non-decreasing indices, i.e. $n_N \geq n_{N-1}$, are considered. According to that, the third order VNLE can be written as

$$\begin{aligned} x_{\text{out}}(k) = h_{\text{DC}} + \sum_{n_1=0}^{N_1-1} h_1(n_1)x_{\text{in}}(k-n_1) + \\ \sum_{n_1=0}^{N_1-1}\sum_{n_2=n_1}^{N_2-1} h_2(n_1,n_2)x_{\text{in}}(k-n_1)x_{\text{in}}(k-n_2) + \\ \sum_{n_1=0}^{N_1-1}\sum_{n_2=n_1}^{N_2-1}\sum_{n_3=n_2}^{N_3-1} h_3(n_1,n_2,n_3)x_{\text{in}}(k-n_1)x_{\text{in}}(k-n_2)x_{\text{in}}(k-n_3). \end{aligned} \tag{3.17}$$

Here, N_i is the memory length for the i^{th} order. The relationship between the number of coefficients and the memory length for each order is given in Tab 3.2. The higher the order, the more coefficients result for a certain memory length, meaning that especially the memory length for the third order needs to be limited to low values.

Table 3.2: Relationship between memory length and coefficient number for first to third order VNLE.

VNLE Order	Number of Coefficients
1^{st}	$C_1 = N_1$
2^{nd}	$C_2 = N_2 \left(N_2 + 1\right)/2$
3^{rd}	$C_3 = N_3 \left(N_3 + 1\right)\left(N_3 + 2\right)/6$

Complexity Reduction of VNLE As the number of VNLE coefficients increases fast with growing memory length, realizations with reduced coefficient numbers are of interest. In this context, two different groups of complexity reduction approaches can be distinguished. The first group does not change the number of coefficients during the adaptation of the weights, but rather selects the relevant coefficients afterwards or changes the cost function to suppress irrelevant coefficients. The second group applies a structural reduction, i.e. rules are defined to limit the number of coefficients before the adaptation of the weights. The latter option is attractive since the final structure of the VNLE is constant for different channels, which is especially important for an implementation in a practical system. Additionally, it has been shown that larger matrices built from transmitted and received data, lead to lower accuracy in matrix inversion [86, 87]. This step is, however, needed for least squares estimation. As a result, realizations with fewer coefficients can lead to better convergence.

A simple approach inside the non-structural reduction schemes is pruning [88, 89]. It is based on the fact that the coefficient weights directly give insight into the coefficient's relevance to the output. A threshold is defined and coefficients with a weight below this threshold are rejected. Another approach is the utilization of the ℓ_1 norm [84, 90, 91]. It is based on an extension of the MMSE cost function (Eq. 3.10) by a penalty term according to

$$F_{\text{MSE},\ell_1} = \mathrm{E}\left\{\left|x_{\text{out}}(k) - x_{\text{in}}(k)\right|^2\right\} + \gamma \sum_{i=1}^{N} ||h_i(k)||_1 \rightarrow \min_{\mathbf{h}}. \tag{3.18}$$

Here, γ is a parameter that controls the influence of the penalty term. Through the penalty term, the coefficient weights are minimized leading to a convergence of less significant coefficients to zero. This way, these coefficients can be neglected and the VNLE complexity is reduced.

In the group of structural approaches for complexity reduction, the memory polynomial (MP) VNLE is a simple and popular example [92]. This approach drastically decreases the

complexity by neglecting all cross-terms. The contribution of the second- and third-order kernels to the equalizer output can be written as

$$x_{\mathrm{out},2,3}(k) = \sum_{n=0}^{N_2-1} h_2(n) x_{\mathrm{in}}(k-n)^2 + \sum_{n=0}^{N_3-1} h_3(n) x_{\mathrm{in}}(k-n)^3. \tag{3.19}$$

Only the quadratic and cubic terms based on a single sample contribute to the equalizer output. The number of coefficients for the nonlinear parts is therefore equal to the respective memory length, i.e. $C_2 = N_2$ and $C_3 = N_3$.

Another structural complexity reduction approach is based on the assumption that coefficients based on neighboring samples play a more significant role for the VNLE output than those further apart from each other. Therefore, the coefficients are limited to those, for which the spacing between the participating samples is limited. A parameter $d_{\max}$ is defined that specifies this maximum spacing and the complexity reduced equalizer is referred to as restricted interval (RI)-$d_{\max}$ VNLE. The contributions of the second and third-order parts on the VNLE output are given by

$$\begin{aligned} x_{\mathrm{out},2,3}(k) = &\sum_{n_1=0}^{N_2-1} \sum_{n_2=n_1}^{N_{d,2}-1} h_2(n_1,n_2) x_{\mathrm{in}}(k-n_1) x_{\mathrm{in}}(k-n_2) \\ &+ \sum_{n_1=0}^{N_3-1} \sum_{n_2=n_1}^{N_{d,3}-1} \sum_{n_3=n_2}^{N_{d,3}-1} h_3(n_1,n_2,n_3) x_{\mathrm{in}}(k-n_1) x_{\mathrm{in}}(k-n_2) x_{\mathrm{in}}(k-n_3). \end{aligned} \tag{3.20}$$

The upper limit is defined as $N_{d,i} = \min\{N_i - 1, n_1 + d_{\max} - 1\}$ for the i^{th} order Volterra kernel. For the number of coefficients of the second and third order, the following relationships result:

$$C_2 = (d_{\max} + 1)(2N_2 - d_{\max})/2, \tag{3.21a}$$
$$C_3 = (d_{\max} + 1)(d_{\max} + 2)(3N_3 - 2d_{\max})/6. \tag{3.21b}$$

This reduction approach is also referred to as diagonally pruned VNLE [93–95].

For the third-order kernel, an extension of the MP VNLE is proposed [96]. In addition to the cubic terms, all cross terms with two different participating samples are considered. This means all cross terms with three different participating samples are neglected. The concept is referred to as 2S VNLE in the following. The contribution of the third-order

kernel is given by

$$x_{\text{out},3}(k) = \sum_{n_1=0}^{N_3-1} \sum_{n_2=n_1}^{N_3-1} \sum_{n_3 \in \{n_1,n_2\}} h_3(n_1,n_2,n_3) x_{\text{in}}(k-n_1) x_{\text{in}}(k-n_2) x_{\text{in}}(k-n_3). \quad (3.22)$$

The case that $\{n_1, n_2\}$ contains $n_1 = n_2$ only results in one coefficient. The number of third-order coefficients is given by

$$C_3 = {N_3}^2. \quad (3.23)$$

Finally, the number of third-order coefficients can be further reduced by combining 2S and RI-$d_{\max}$ VNLE. According to that, only coefficients based on up to two different samples with a maximum spacing of $d_{\max}$ are considered. The third-order part can be written as

$$x_{\text{out},3}(k) = \sum_{n_1=0}^{N_3-1} \sum_{n_2=n_1}^{N_{d,3}-1} \sum_{n_3 \in \{n_1,n_2\}} h_3(n_1,n_2,n_3) x_{\text{in}}(k-n_1) x_{\text{in}}(k-n_2) x_{\text{in}}(k-n_3). \quad (3.24)$$

For the number of coefficients in dependence on the memory length

$$C_3 = 2N_3 d_{\max} - d_{\max}(d_{\max}+1) + N_3. \quad (3.25)$$

results.

The effect of the described complexity reduction approaches on the number of third-order coefficients is visualized in Fig. 3.13. A fast growth of the coefficient number can be observed for the full VNLE. A memory length of $N_3 = 10$ leads to more than 200 coefficients and therefore to high computational complexity. On the other side, the MP VNLE drastically lowers the complexity. Due to the linear relationship between memory length and resulting coefficient number, it uses significantly fewer coefficients than all other approaches. The 2S VNLE lies between these two extremes and reaches approximately 200 coefficients at a memory length of $N_3 = 14$. The RI-$d_{\max}$ VNLE allows a flexible scaling of the complexity. The two examples of $d_{\max} = [N_3/2]$ and $d_{\max} = [N_3/4]$ are shown, where $[\cdot]$ denotes the rounding operation. While for $d_{\max} = [N_3/2]$ the coefficient number lies between full and 2S VNLE, $d_{\max} = [N_3/4]$ leads to a complexity slightly lower than that of the 2S variant. For the combined approach based on RI-$d_{\max}$ and 2S VNLE, the relationship between third-order memory length and the coefficient number is exemplary shown for $d_{\max} = [N_3/2]$. This restriction leads to less than 200 coefficients at a memory length of $N_3 = 15$. The complexity reduction approaches can either reduce the number of

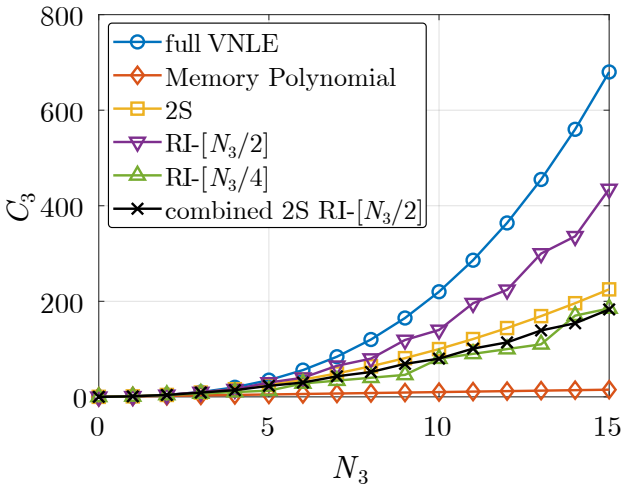

Figure 3.13: Third order VNLE coefficient number C_3 over memory length N_3. Different structural complexity reduction approaches are compared.

coefficients at a given memory length significantly, or a higher memory length is possible at a given coefficient number. The latter point can be very beneficial in systems that induce strong ISI on the signal before the nonlinearities occur. To allow a statement over the benefit of the complexity reduction schemes, the complexity-performance trade-off needs to be carefully compared for a given system.

Non-uniformly Quantized Equalizer As shown in the previous part, the equalizer complexity can be reduced by reducing the coefficients to a subset. A different approach proposed in [97] is changing the resolution of the input samples to reduce the equalizer computational complexity. Generally, the receiver DSP works with an input signal at the resolution provided by the ADC. If the length of this binary representation is shortened, the multiplications done during the training of the coefficients and equalization require less resources. Therefore, it is desirable to reduce the average resolution per sample processed by FFE. The non-uniformly quantized (NUQ) FFE realizes this by separating the coefficients of conventional FFE into two subsets. While the first subset works with the full available resolution, the second subset uses samples from the same signal with a lower resolution. The signal with the lower resolution is generated by quantizing the initial signal. The structure of the NUQ FFE is depicted in Fig. 3.14. Both coefficient sets are individually adapted and executed before the output is generated by summing up the individual outputs. During the decision-directed adaptation of the coefficients, this output is used for both subsets. As shown in the example in Fig. 3.12 a), the central linear coefficients have a large impact on the output. According to that, a promising approach is using the full resolution samples for these coefficients, while the outer linear, as well as the nonlinear coefficients, use samples with a limited resolution.

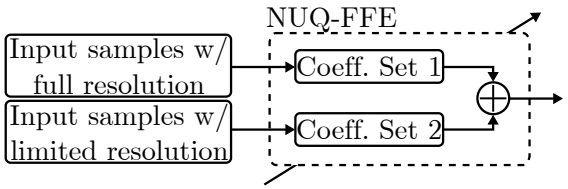

Figure 3.14: Structure of the NUQ FFE.

3.2.2 Decision-Feedback Equalization

In contrast to the linear FFE, DFE is based on a nonlinear equalizer structure. It can compensate spectral nulls and avoids noise enhancement [74]. DFE is, however, typically used in combination with FFE. This combination has good capabilities for compensating pre- and post-cursor ISI. The relationship between equalizer input and output for the FFE-DFE combination can be expressed as

$$x_{\text{out}}(k) = h_{\text{DC}} + \sum_{n=0}^{N_{\text{FFE}}-1} h(n) \cdot x_{\text{in}}(k-n) - \sum_{n=0}^{N_{\text{DFE}}-1} b(n) \cdot \hat{x}_{\text{out}}(k-n). \tag{3.26}$$

Here, b contains the DFE coefficients.

The coefficient update rule according to the LMS algorithm for DFE is given by [74]

$$b_{\text{LMS}}(k+1) = b_{\text{LMS}}(k) + \mu\epsilon(k)\hat{x}^*_{\text{out}}(k). \tag{3.27}$$

The structure of an adaptive FFE-DFE combination is shown in Fig. 3.15. The incoming signal $x_{\text{in}}(k)$ is filtered through the FIR filter structure of the FFE with the coefficient vector $\mathbf{h}$. From the resulting signal, the feedback branch filtered with the DFE coefficients $\mathbf{b}$ is subtracted. Afterwards, a decision is performed on the resulting equalizer output $x_{\text{out}}(k)$. This is typically done based on the nearest-neighbor criterion, i.e. the constellation point with the least distance to the equalizer output is selected as decision $\hat{x}_{\text{out}}(k)$. The decided equalizer output is used to calculate the error $\epsilon(k)$ according to Eq. 3.13. During the initial training mode, the training symbols $d_t(k)$ are used instead of the decisions. The same error is used to update both, FFE and DFE coefficients so that a joint optimal channel equalization is achieved.

The contribution of the feedback branch is based on decisions $\hat{x}_{\text{out}}(k)$ on the equalizer output values. Wrong symbol decisions will therefore not only lead to an error in the current equalizer output but will also impact successive outputs. To visualize the effect of error propagation, Fig. 3.16 shows the distribution of errors along a PAM-4 signal transmitted over the exemplary channel with the response $h_{\text{Ch}} = [0.4\ 1\ 0.4]$ at an SNR

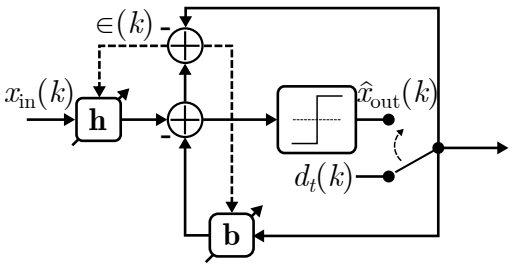

Figure 3.15: Structure of an adaptive FFE-DFE combination.

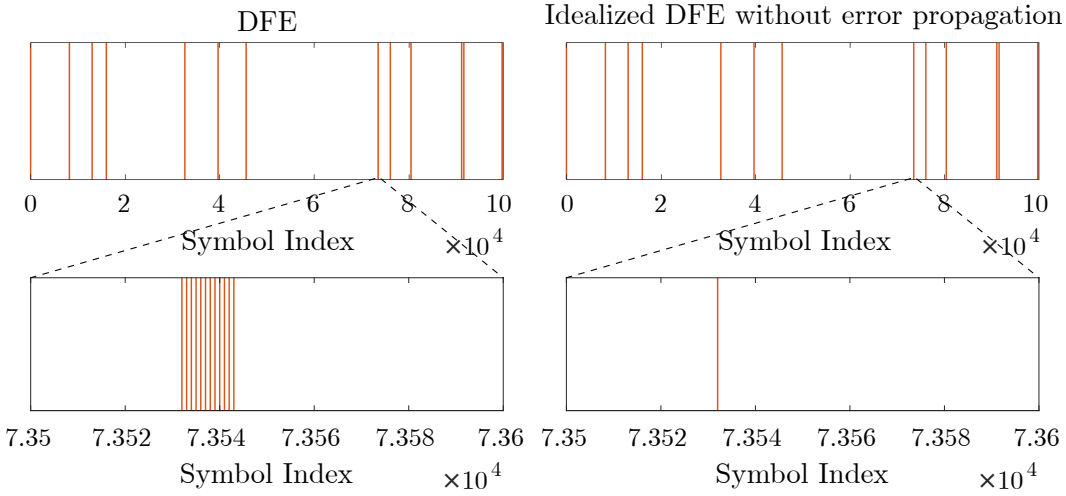

Figure 3.16: Distribution of errors after FFE-DFE. The idealized DFE shows the unpractical scenario of a DFE that always feeds back the correct symbol.

of 40 dB. The red bars denote the indices, at which errors occurred. Two scenarios are considered: conventional DFE and an idealized DFE that always feeds back the correct symbol. The latter case is unpractical since knowledge about all transmitted symbols would need to be available, however, it shows the performance limit that could be reached, if no error propagation would exist. Looking at the upper distribution, it seems that the errors occur at the same indices for both cases. When looking closer into the regions where errors occur, it can be observed that several consecutive errors occur after conventional DFE, while only one error results in the idealized scenario. All errors following the initial one are caused by error propagation.

Modifications of DFE

As described in the previous part, DFE suffers from error propagation. THP can avoid this problem, however, channel information needs to be available at the transmitter, which makes a feedback channel necessary. Weighted decision-feedback equalization (WDFE) is an approach to limit error propagation in DFE while still being deployed in the receiver DSP. While the hard decision $\hat{x}_{\text{out}}(k)$ on the equalizer output $x_{\text{out}}(k)$ is fed back in

conventional DFE, a weighted decision is utilized in WDFE. The weighted decision, which is formed as a combination of equalizer output and hard decision, is defined as

$$\overline{x}_{\text{out}}(k) = f(\gamma_k)\,\hat{x}_{\text{out}}(k) + [1 - f(\gamma_k)]\,x_{\text{out}}(k). \tag{3.28}$$

Here, γ_k is the reliability value and $f(\cdot)$ is a function that defines the proportions of equalizer output and hard decision. The reliability value is based on the distance between the equalizer output and the associated decision. For a PAM-4 constellation with the constellation points [-3;-1;1;3], it is calculated according to

$$\gamma_k = \begin{cases} 1 - |x_{\text{out}}(k) - \hat{x}_{\text{out}}(k)|, \text{if } -3 < x_{\text{out}}(k) < 3 \\ 1, \text{else} \end{cases}. \tag{3.29}$$

For the WDFE function, several approaches have been proposed [98–102]. For example, a threshold function

$$f_{\text{R1}}(\gamma_k) = \begin{cases} 1, & \text{if} \gamma_k \geq d_{\min} \\ 0, & \text{else} \end{cases} \tag{3.30}$$

is used [99, 100], where $d_{\min}$ is a threshold constant. If the reliability value is above the threshold, the hard decision is fed back, while the equalizer output without decision is fed back otherwise. An alternative is given by the relationship

$$f_{\text{R2}}(\gamma_k) = \gamma_k. \tag{3.31}$$

In this case, the reliability value directly decides about the proportions between equalizer output and decision value in the feedback branch.

An improved approach is given by a compressed sigmoid function [98]:

$$f_{\text{I1}}(\gamma_k) = \frac{1}{2}\left(\frac{1 - \exp\left[-a_s(\gamma_k/b_s - 1)\right]}{1 + \exp\left[-a_s(\gamma_k/b_s - 1)\right]} + 1\right). \tag{3.32}$$

Here, a_s is a positive integer defining the steepness of the sigmoid function and $0 \leq b_s \leq 1$ is a compression factor defining the reliability value, at which the function reaches the value 0.5. The output values of the function f_{I1} are inside the interval [0;1]. However, for some scenarios it can be advantageous to introduce an upper limit $I_{\max}$ to the function,

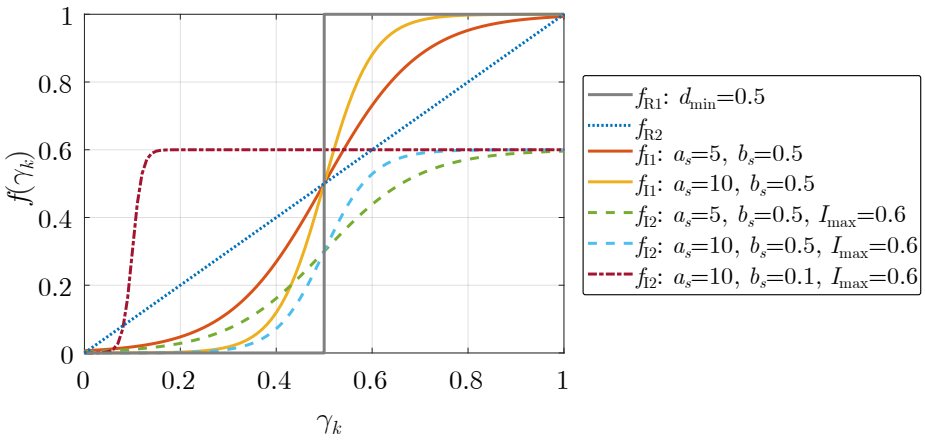

Figure 3.17: Visualization of selected WDFE functions.

resulting in the rule

$$f_{\mathrm{I2}}(\gamma_k) = \frac{I_{\max}}{2}\left(\frac{1-\exp\left[-a_s(\gamma_k/b_s-1)\right]}{1+\exp\left[-a_s(\gamma_k/b_s-1)\right]}+1\right). \tag{3.33}$$

In this case, the function values lie inside the interval $[0,I_{\max}]$. Examples for all introduced WDFE functions are shown in Fig. 3.17. Conventional DFE would be represented by a constant function value of $f(\gamma_k) = 1$. All shown functions share the property that a reliability value close to zero leads to a function value close to zero. A high reliability value, on the other hand, leads to the maximum value of each function.

The concept of WDFE can be further simplified by specifying a constant ratio r_c between hard decision $\hat{x}_{\mathrm{out}}$ and equalizer output x_{out}. This corresponds to a constant value for the WDFE function and makes the calculation of the reliability value pointless. The feedback for this case is given by

$$\overline{x}_{\mathrm{out}}(k) = r_c\hat{x}_{\mathrm{out}}(k) + [1-r_c]\,x_{\mathrm{out}}(k). \tag{3.34}$$

WDFE with a ratio in the range $0 < r_c < 1$ can be viewed as an intermediate stage between infinite impulse response (IIR) filter ($r_c = 0$) and DFE ($r_c = 1$). As this concept avoids an evaluation of the reliability and does therefore not weight decisions, it is referred to as partial decision-feedback equalizer (PDFE) in the following. The closer the equalizer approaches an IIR filter, the more noise enhancement after equalization can result. Therefore, it can be relevant to combine this concept with approaches to overcome or avoid noise enhancement.

If the WDFE coefficients are optimized in a decision-directed manner, two options for

the calculation of the error $\epsilon(k)$ exist. Either, it is calculated based on the hard decision as in Eq. 3.13, or it is calculated based on the weighted decision as

$$\epsilon(k) = x_{\text{out}}(k) - \overline{x}_{\text{out}}(k). \tag{3.35}$$

The latter option leads to a less significant adaptation of the coefficients, the closer the WDFE approaches an IIR filter.

3.2.3 Noise Whitening Filter

As explained in Sec. 3.2.1, the equalization of channels that induce strong attenuation on certain signal components using FFE, results in noise enhancement. In the previous sections, several approaches to avoid the occurrence of this effect during equalization have been explained, such as partial response signaling, THP and DFE. The idea of a noise whitening filter is to flatten the noise after FFE based on the actual noise enhancement. This is done by a simple FIR filter with few memory taps, as shown e.g. in [103–106]. As this filter induces ISI to the signal, additional DSP is necessary to remove the controlled ISI and enable recovery of the data. For this task, Viterbi equalization (cf. Sec. 3.2.4) is used. As the complexity of this approach grows exponentially with memory length, it is critical to keep the FIR filter short.

Fig. 3.18 shows the DSP steps for the application of a noise whitening FIR filter and Viterbi equalization after FFE. Additionally, the spectra of signal and noise are shown for the exemplary low pass channel introduced in Sec. 3.2.1. As already depicted in Fig. 3.12, FFE flattens the signal spectrum, but leads to enhanced noise, in case the noise occurred after the low-pass characteristic was induced on the signal. The following FIR filter with the memory coefficients $\mathbf{l} = [l_1, l_2, ..., l_N]$ flattens the noise spectrum, but introduces ISI to the signal. Note that an exact flattening of the noise spectrum may require a high number of FIR coefficients. The spectra of noise and signal are similar to the situation before FFE, but the filter coefficients applied to the signal are exactly known so that these can be effectively removed using Viterbi equalization. After removing the ISI, both, the signal and noise spectra, show the desired flat shape.

A straightforward approach to finding the ideal coefficients for the FIR filter is a sweep through possible values and the selection of the coefficients leading to the best overall performance [103, 104]. However, this procedure is not desirable, since it becomes elaborate for higher coefficient numbers. Alternatively, the coefficients can be estimated by autoregression. For example, the Yule-Walker equations can be applied to the noise signal to find coefficients that whiten the sequence [105]. In this work, the iterative Burg

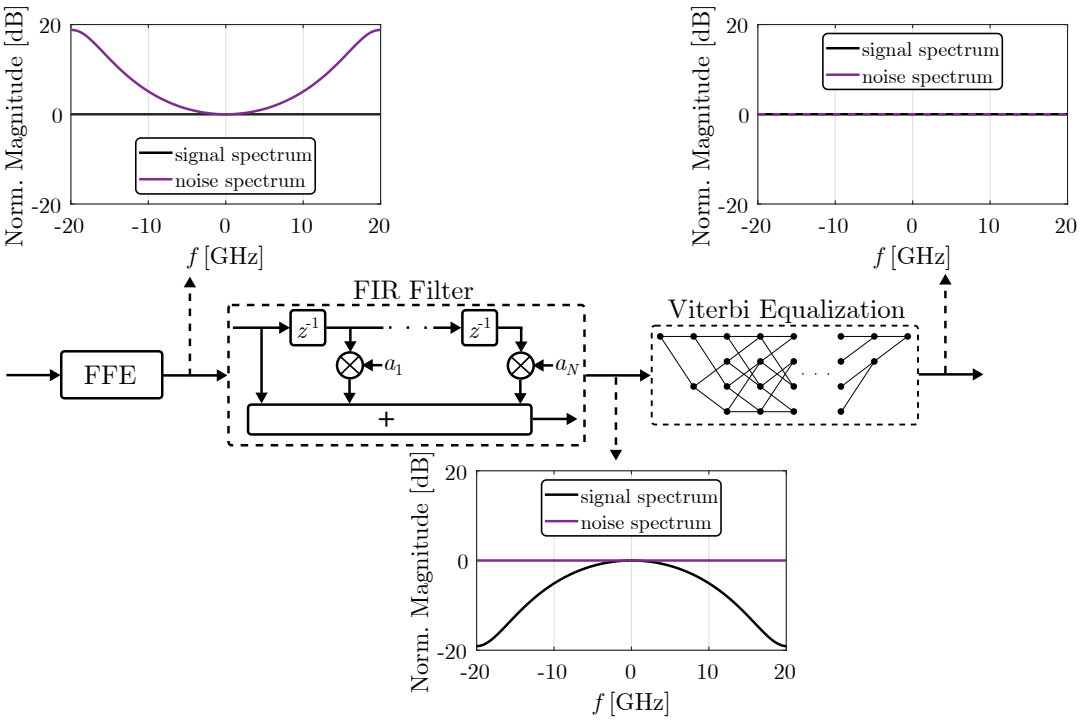

Figure 3.18: DSP structure for FFE followed by a noise whitening FIR filter and Viterbi equalization. Exemplary spectra showing the impact on the signal and noise are shown after each step.

algorithm [107–109], a scheme known for parametric power spectrum estimation, is used to find the FIR filter coefficients. In each iteration, the reflection coefficient is updated according to

$$\hat{k}_m = \frac{2 \cdot \sum_{k=1}^{K-1} e_{m-1}(k) \cdot g_{m-1}(k-1)}{\sum_{k=1}^{K-1} |e_{m-1}(k)|^2 + |g_{m-1}(k-1)|^2}. \tag{3.36}$$

Here, K is the number of training symbols and $e(k)$ and $g(k)$ are the forward and backward prediction errors, respectively. These are initialized with the noise sequence of the training symbols. The noise is estimated here as the difference between equalizer output and training symbols. The updating rules for the prediction errors are given by

$$e_m(k) = e_{m-1}(k) - \hat{k}_m \cdot g_{m-1}(k-1) \quad \text{and} \tag{3.37}$$

$$g_m(k) = g_{m-1}(k-1) - \hat{k}_m \cdot e_{m-1}(k). \tag{3.38}$$

Based on these parameters, the coefficient vector is updated by

$$l_m(n) = l_{m-1}(n) - \hat{k}_m \cdot l_{m-1}(p-n), \quad 1 \leq n \leq p-1 \tag{3.39}$$

$$1 \leq p \leq N. \tag{3.40}$$

The steps are repeated N times to find the set of coefficients $\mathbf{l}$. The zero-delay coefficient has a value of $l_0 = 1$. Applying an FIR filter with these coefficients on the signal flattens the noise. The higher the number of coefficients N is chosen, the flatter the resulting noise spectrum.

Decomposition of Post-filter Response

While a single memory coefficient for the noise whitening filter can be sufficient for many scenarios, in case of strong lowpass characteristics of the channel multiple coefficients may be required to flatten the noise spectrum. However, in case a decision-directed update process of the equalizer coefficients is applied, the performance in a constrained scenario can still be poor, even if high numbers of post-filter coefficients are used. The reason for this is a poor equalizer convergence because the received signal response and the target response deviate significantly. Therefore, it can be advantageous to decompose the noise whitening filter response into a partial response equalization and a shorter subsequent post-filter. For example, instead of a full response equalizer followed by a two-coefficient noise whitening filter, equalization directly targeting the DB response followed by a one-coefficient post-filter can be applied. This can significantly increase the equalizer convergence and therefore the overall performance.

3.2.4 Viterbi Equalization

The Viterbi algorithm has been proposed as a decoding scheme for convolutional codes [110]. It can be described as an optimal solution to estimate the state sequence of a discrete-time finite-state Markov process recursively, given memoryless noise [111]. This kind of process can be represented by a trellis diagram. Such a diagram has a node for each state at a given time, as exemplarily shown in Fig. 3.19 for a four-state process. Depending on the process, each state can be followed by all other states or only has certain successors. The longer the input sequence is, the more complex the calculation of the whole trellis diagram gets. Since this leads to an excessive computational complexity that cannot be tolerated for practical systems, a less complex approach to finding an optimal path through the trellis needs to be applied. The Viterbi algorithm delivers a solution for this problem by neglecting all but the shortest path to each state. For each transition from a state i to state j, a path metric $\lambda_p^{(i \to j)}(k)$ can be calculated. For each

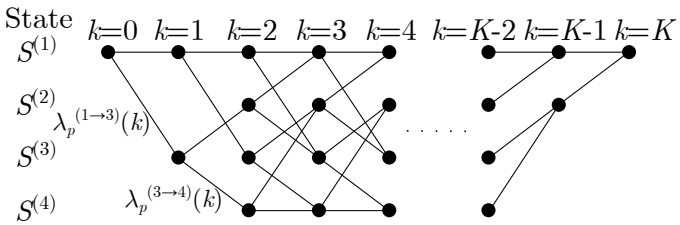

Figure 3.19: Exemplary trellis diagram describing a four-state process, according to [111].

state $S^{(j)}$ at a time instant k, the sum path metric $\Lambda_p^{(j)}(k)$ is determined using all paths leading to that state. The path segment with the lowest sum path metric is selected as *survivor*, while all other paths to the respective state are neglected [111].

The Viterbi algorithm can be effectively used to remove known ISI from a signal [67, 111]. To describe the operation of Viterbi equalization (VE) for this task, lets assume $x_{\text{in}}(k)$ is the input sequence, and the ISI can be described by the frequency response $H(z) = 1 + \sum_{k=1}^{p} h(k) z^{-k}$. For a symbol constellation of order M, a number of M^p states defined as $S^{(i)} = [s^{(i)}(k-1), s^{(i)}(k-2), ..., s^{(i)}(k-p)]$, $i = 1, 2, ..., M^p$ results. To find the optimal path through the trellis given the defined ISI, the Viterbi algorithm undergoes the following steps [67]:

- The path metrics for all M paths leading to each state $S^{(i)}$ are calculated according to

$$\lambda_p^{(i \to j)}(k) = \left| x_{\text{in}}(k) - s(k) - \sum_{n=1}^{p} h(k) \cdot s^{(i)}(k-n) \right|^2 . \tag{3.41}$$

- These path metrics are added to the accumulated sum path metric $\Lambda_p^{(i)}(k)$.

- The M sum path metrics $\Lambda_p^{(j)}(k+1)$ for each state are compared.

- The path with the lowest sum path metric is selected as survivor for the state $S^{(j)}$ at the time $k+1$, while all other paths are rejected.

After the full signal was processed through these steps, the most probable sequence can be determined by a method called *trace back*. Beginning with the final sum path metrics for all states, the lowest value is taken as a starting point. From this point on, the algorithm runs through the sequence backwards and goes from each state to the stored predecessor. Finally, the optimal sequence of states results and the signal without ISI is determined.

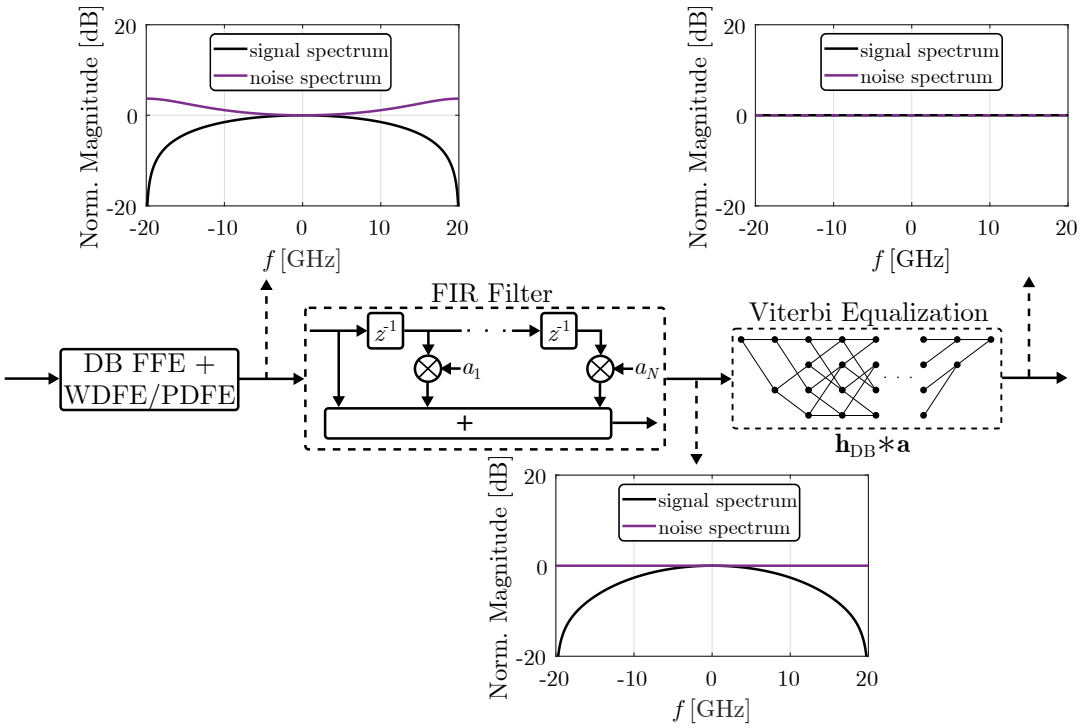

Figure 3.20: DSP structure for DB FFE + WDFE/PDFE followed by a noise whitening FIR filter and VE. Exemplary spectra showing the impact on the signal and noise are shown after each step.

3.2.5 Combinations of DSP Approaches

It can be beneficial to combine multiple of the previously introduced DSP approaches. Simple schemes like non-regular PAM constellations can be combined with any other approach. Also, bandwidth pre-compensation and VNLE can be beneficial in combination with the other schemes. An interesting approach is given by the combination of WDFE/PDFE and a noise whitening filter. If the upper limit $I_{\max}$ is selected to be smaller than one, noise enhancement can result in the equalizer output signal. The same effect occurs for a small ratio r_c in PDFE. A noise whitening filter in combination with VE can help to combat this effect and significantly improve performance. Under strongly constrained conditions, it might be helpful to combine DB equalization with DFE. The performance can additionally be improved by combining WDFE/PDFE with DB equalization, noise whitening filtering and VE, i.e. to decompose a longer post-filter response (cf. Sec. 3.2.3), as depicted in Fig. 3.20. Even equalization targeting the DB response may lead to noise enhancement. This happens, if the transmission system's end-to-end response is even narrower than the DB spectrum. In this case, a noise whitening FIR filter can be additionally applied. The signal after this filter contains ISI induced by the DB response and the whitening filter response. Therefore, the subsequent VE needs to

remove the combined response, given by the convolution of both individual responses, from the signal. Afterwards, the signal and noise spectra have the desired flat shape. Such combinations of DSP approaches can lead to a significantly increased complexity and may therefore not be considered for practical systems unless a large performance advantage can be achieved.

3.3 Approaches Specifically Focussing on Chromatic Dispersion

It is well known, that CD cannot be completely removed by EDC in IM/DD systems due to the lack of complex field information at the receiver. This can lead to tremendous performance degradation due to power fading, as described in Sec. 2.3.1. Two approaches to limit the impact of this effect are described in the following part.

3.3.1 Gerchberg-Saxton based Electronic Dispersion Compensation

Recently, an approach to overcome CD in IM/DD systems has been proposed [112] and experimentally investigated [113, 114]. It is based on the Gerchberg-Saxton (GS) algorithm and iteratively adjusts the transmitted signal to the dispersive channel, as depicted in Fig. 3.21. The initial signal $a_0(k)$ is given as the square root of the input signal intensity $I(k)$. This signal is transmitted over a simulated channel, which only adds CD. This is simulated using the frequency response

$$H_{\mathrm{GVD}}(f) = e^{-j\lambda^2 DL\pi f^2/c}, \tag{3.42}$$

which can be directly concluded from Eqs. 2.8 and 2.10 considering only the group velocity dispersion parameter. The accumulated dispersion $D \cdot L$ needs to be equal to the actual value of the pre-compensated channel. The received signal $r(k)$ is complex-valued and can therefore be separated into magnitude and phase. In the next step, a so-called receiver constraint is applied, which sets the magnitudes of the received signal to those of the initial signal $a_0(k)$. Afterwards, the signal is transmitted back over a channel with an inverse dispersion coefficient. At the transmitter side, a second constraint is applied: The absolute value of the signal is taken, i.e. the phase is removed. This procedure is repeated multiple times to optimize the signal for transmission over the dispersive channel. After the N iterations, the output is given by $a_{\mathrm{out}}(k) = |a'_N(k)|^2$.

For the proper functioning of the scheme, the input signal needs to contain a certain DC component. To specify this DC, the digital extinction ratio (ER) is defined as the ratio between the maximum and minimum power of the signal.

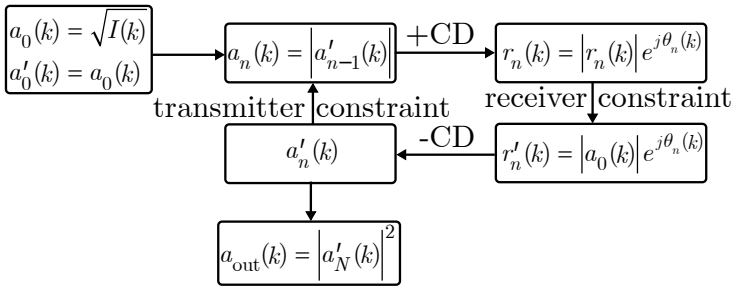

Figure 3.21: Iterative procedure of the GS based EDC scheme.

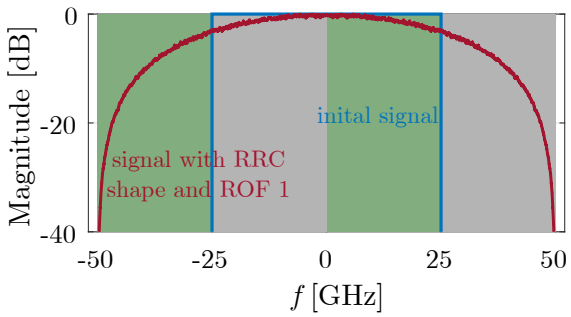

Figure 3.22: Visualization of the redundant information in oversampled signals. The areas with the same color contain identical information.

3.3.2 Selected Frequency Pre-Compensation

Due to the complete loss of certain frequency components in the received signal, spectral nulls induced by the power fading effect can severely degrade the performance in IM/DD systems. Selected frequency pre-compensation (SFPC) is an approach to improve the capability of compensating these nulls for certain systems [115]. The approach is based on the fact, that oversampled transmitted signals contain redundant information. This redundancy can be utilized at the receiver in order to reconstruct the missing information at the null frequencies. To visualize the redundancy in an oversampled signal, Fig. 3.22 shows the spectra of a 50 GBd signal before and after oversampling by a factor of two. An RRC pulse shape with an ROF of $\beta_{\text{ro}} = 1$ is used in this example, however, the observation is the same for other pulse shapes. Due to the oversampling, the spectral width of the signal is doubled. As the information still originates from the same source, the oversampled signal contains redundant information. More precisely, two frequencies in the oversampled signal that are separated by the symbol rate contain the same information. According to that, the two grey areas and the two green areas in Fig. 3.22 contain the same information. If real-valued signals are considered, the two sidebands of the signal are also redundant. However, as the power fading effect leads to symmetric spectral nulls at positive and negative frequencies (cf. Sec. 2.3.1), this redundancy cannot help to compensate for that effect.

Assuming the frequency $f_{\mathrm{null},n}$ is the n^{th} spectral null caused by power fading, the redundant frequency $f_{\mathrm{r},n}$, which contains the same information, exists in a sufficiently oversampled signal. The relationship is given by

$$f_{\mathrm{r},n} = \begin{cases} f_{\mathrm{null},n} + f_{\mathrm{sym}}, & \text{if } f_{\mathrm{null},n} < 0 \\ f_{\mathrm{null},n} - f_{\mathrm{sym}}, & \text{else} \end{cases}. \tag{3.43}$$

Here, f_{sym} is the symbol rate. This redundant frequency can therefore be used at the receiver to recover the lost information at $f_{\mathrm{null},n}$. The idea of SFPC is to make this reconstruction more effective, by amplifying the relevant redundant frequencies in the transmitted signal to ensure increased quality of these signal parts at the receiver. This makes it necessary to know the positions of the spectral nulls at the transmitter. The redundant frequencies can only be utilized at the receiver, if sufficient oversampling is given. The amount of oversampling required is dependent on the positions of the redundant frequencies. Assuming $f_{\mathrm{r,max}}$ is the highest redundant frequency, required to compensate the lowest spectral null frequency, the necessary oversampling factor is given by

$$n_{\mathrm{OS}} \geq \frac{f_{\mathrm{r,max}}}{f_{\mathrm{sym}}}. \tag{3.44}$$

Since frequencies close to the spectral nulls also experience significant attenuation, it helps to amplify not only the redundant frequencies but also a certain range of frequencies around these. This range as well as the exact amount of amplification applied on each redundant frequency needs to be optimized in order to achieve a gain through SFPC. A straightforward, but computationally costly, approach is to sweep through these parameters and select the set of parameters that leads to the best performance. A more practical approach is choosing the amplifications according to the inverse of the power fading frequency response (Eq. 2.16). This, however, requires that the redundant frequencies are not significantly attenuated by other effects, such as bandwidth limitations. This situation can be achieved by combining SFPC and conventional inverse bandwidth pre-compensation (cf. Sec. 3.1.4).

A drawback of SFPC and the general concept of using redundant frequencies of oversampled signals to reconstruct spectral nulls is the fact, that the redundant frequencies can be subject to power fading themself. If this is the case, the spectral null cannot be compensated and the performance is significantly degraded. To find those combinations of wavelength, accumulated dispersion and symbol rate for which this undesired case occurs, Eq. 2.19 can be utilized. If $F_{\mathrm{null}} = \{f_{\mathrm{null},0}; f_{\mathrm{null},1}; f_{\mathrm{null},2}; ...\}$ is the set containing

all spectral nulls for a certain scenario, the condition for the redundant frequency to be at the exact position of a spectral null is

$$f_{\mathrm{sym}} - |f_{\mathrm{null},m}| \in F_{\mathrm{null}}, m \in \mathbb{N}_0. \tag{3.45}$$

Here, $f_{\mathrm{null},m}$ is restricted to the spectral nulls inside the useful data signal range:

$$|f_{\mathrm{null},m}| \leq \frac{f_{\mathrm{sym}}}{2}. \tag{3.46}$$

While redundant frequencies lying directly at the position of a spectral null have no use, also redundant frequencies neighboring spectral nulls are significantly attenuated and can therefore hardly be utilized. According to that, the condition for non-compensable combinations of wavelength, accumulated dispersion and symbol rate can be adapted based on the power fading frequency response $H_{\mathrm{CD,DD}}(f)$ (right part of Eq. 2.18). A spectral null can be considered as non-compensable or only partly compensable, if the corresponding redundant frequency experiences an attenuation of at least a_{min}. The condition can be written as

$$H_{\mathrm{CD,DD}}(f_{\mathrm{sym}} - |f_{\mathrm{null},m}|) \leq a_{\mathrm{min}}, m \in \mathbb{N}_0. \tag{3.47}$$

In realistic scenarios, it is probable, that a fixed data rate is transmitted at a fixed wavelength over varying fiber lengths. In this case, the condition results in one or more intervals of lengths that are hardy compensable. As it is not tolerable, that certain transmission lengths lead to significantly degraded performance, a solution to flexibly shift these intervals to other lengths is of interest. An interesting approach is a variation of the transient frequency chirp. As described in Eq. 2.19, the chirp parameter α_{C} has a direct influence on the positions of the spectral nulls. Different transmitters with a variable chirp have been shown in the literature. One approach is the chirp-managed laser, which consists of a DML followed by an optical filter that attenuates one sideband [116, 117]. Alternatively, a polarization modulator with a tunable polarization controller can be used to vary the chirp parameter [118]. A simple option to achieve variations of the transient chirp is given by the fact, that several components show a dependency between chirp and their input signals [119, 120]. For example, the linewidth enhancement factor of an EAM is dependent on the input voltage. Therefore, the bias voltage can be changed to achieve changed chirp characteristics. This, however, also has an impact on the optical output power and extinction ratio. Similarly, SOAs show a dependence between driving current and chirp [120]. This change in driving current also results in a change in amplification. These relationships for EAMs are analyzed in Sec. 5.1.9.

Chapter 4

Digital Signal Processing for Advanced Direct-Detection Systems

Different options to increase the impairment tolerance of DD systems and to increase the achievable rates exist. In the following, relevant options based on advanced DD systems, i.e. systems using advanced hardware compared to IM/DD systems, are described in detail. The first approach, namely the electronic dispersion pre-compensation (EDPC), only focuses on the compensation of dispersion. Additionally, a certain group of SCOH systems that enable the recovery of the complex field using only a single PD is described. These systems do not only enable EDC at the receiver but also the use of complex symbol constellations. In this context, the KK receiver and different SSBI cancellation approaches are shown.

4.1 Chromatic Dispersion Pre-Compensation

In the transmitter DSP of any transmission system, the full complex signal information, i.e. real and imaginary parts of the signal, are known. Therefore, EDPC can be applied, given that the complex output signal can be modulated on the optical carrier. The basis for electrical CD compensation is the frequency response in Eq. 3.42. To apply this function, the accumulated dispersion $D \cdot L$ in the link needs to be known at the transmitter. This makes a feedback channel necessary in networks with unknown or varying dispersion parameters.

To modulate this information on the optical signal, so that the CD effect is pre-compensated, a simple intensity modulator is not sufficient. As information is stored on the real and imaginary parts of the signal, either a dual-drive MZM [121, 122] or an IQ-modulator [123, 124] needs to be used for this task. For a dual-drive MZM, the input-output relationship is given by [122]

$$E_{\text{out}} = E_{\text{in}} \cos\left(\frac{\pi(u_1(t) - u_2(t))}{2V_\pi}\right) e^{j\pi(u_1(t)+u_2(t))/(2V_\pi)}, \tag{4.1}$$

where $u_1(t)$ and $u_2(t)$ are the electrical driving signals. The desired pre-compensated field $E_{\mathrm{Tx}} = |E_{\mathrm{Tx}}| \cdot e^{j\phi}$ is given by the initial signal waveform filtered with the CD frequency response. The driving voltages to realize this output are given by

$$u_1(t) = \frac{V_\pi}{\pi}\left(\phi + \arccos\left(\frac{E_{\mathrm{Tx}}}{E_{\mathrm{in}}}\right)\right) \text{ and } u_2(t) = \frac{V_\pi}{\pi}\left(\phi - \arccos\left(\frac{E_{\mathrm{Tx}}}{E_{\mathrm{in}}}\right)\right). \tag{4.2}$$

If an IQ-modulator is used, the real and imaginary parts of the filtered signal waveform can be directly handed over to the two modulator branches and no further adaptations are necessary. As an alternative to the frequency response in Eq. 3.42, FIR filters for the I- and Q-branches of the modulator can be used for pre-compensation [124]. To do this, the same real-valued signal before digital-to-analog conversion is fed into two different FIR filters $\mathrm{FIR_I}$ and $\mathrm{FIR_Q}$. The filter outputs are fed to the corresponding branches of the IQ-modulator. The filter coefficients can be calculated as given in Eqs. 27 and 28 in [35].

4.2 Self-Coherent Systems

While IM/DD systems are limited to real-valued modulation formats and their tolerance towards CD is limited, coherent systems are costly due to the high demand on additional receiver hardware (cf. Sec. 2.3.2). SCOH systems aim at the reconstruction of complex-valued signals, which allows complex modulation formats and EDC, with less hardware - especially without the need for an LO.

In this work, a subgroup of SCOH systems that uses only a single PD for the O/E conversion is considered. Such systems can recover the complex field information of the received signal, if the minimum phase condition is fulfilled [125]. One requirement to fulfill this condition is the transmission of an SSB signal. Assuming $s(t)$ is a signal that is contained in the frequency range $[-B/2; B/2]$, an SSB signal can be expressed as

$$s_{\mathrm{SSB}}(t) = E_0 + s(t)e^{-j\pi Bt}, \tag{4.3}$$

where E_0 is a constant. It can be shown that the minimum phase condition is fulfilled for an SSB signal, if the time trajectory of the signal does not encircle the origin [125, 126]. This can be achieved by choosing the carrier component $|E_0|$ sufficiently large. To describe the relative power of the carrier component compared to the signal, the carrier-to-signal power ratio (CSPR) is defined as the carrier power divided by the signal power. Figure 4.1 shows two exemplary time trajectories for SSB 16-QAM signals with different CSPR

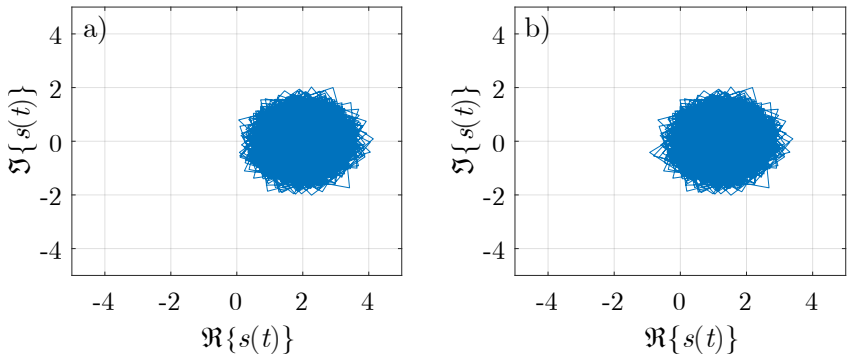

Figure 4.1: Constellation diagrams of SSB signals (16-QAM, RRC roll-off factor $\beta_{\mathrm{ro}} = 0.05$). a) shows a signal with an CSPR of 6 dB fulfilling the minimum phase condition and b) shows a violation of the condition at a CSPR of 2 dB.

values. At 6 dB CSPR the signal does not cross the origin and the minimum phase condition is fulfilled. Figure 4.1 b) shows a signal with a CSPR of 2 dB. The time constellation diagram clearly crosses the origin, so that this signal violates the minimum phase condition and cannot be completely reconstructed.

As described in Sec. 2.3.3, the signal after detection with a PD is overlaid by SSBI. Two straightforward approaches to overcome this effect are either leaving a large frequency gap between signal and carrier, so that the SSBI does not fall into the signal range, or choosing the CSPR so high that the SSBI term gets negligible [38]. Both of these approaches are not practical, as they result in lowered spectral efficiency or reduced SNR sensitivity, respectively. Approaches that avoid these issues are the well-studied KK receiver (Sec. 4.2.2) and SSBI cancellation (Sec. 4.2.3).

4.2.1 SSB Signal Generation

As described in the previous part, SSB signals are required for SCOH systems based on the reception with a single PD. For the generation of such signals, different approaches exist. If only the amplitude of the signal is modulated, two common approaches are used: The SSB signal can either be formed by generating the analytical signal based on the Hilbert transform and using an IQ-modulator, or an intensity modulator is used and one sideband is removed by an optical filter [31, 32].

However, in this work SCOH systems transmitting complex symbol constellations are considered. For the transmission of such constellations, three approaches for the SSB signal generation can be distinguished [38, 127]. These approaches are visualized in Fig. 4.2. The first approach in Fig. 4.2 a) uses a digital up-conversion of the complex signal before digital-to-analog conversion. The signal spectrum is shifted by half of the bandwidth B

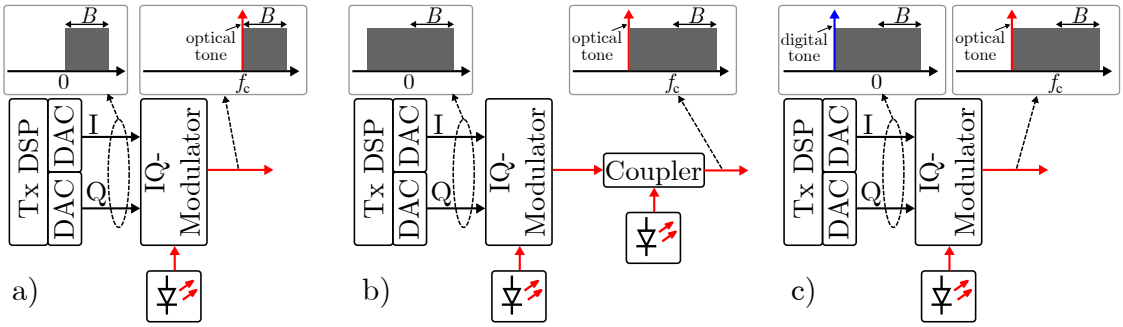

Figure 4.2: Approaches to generate an SSB signal. a) is based on driving the modulator with an electrical SSB signal, in option b) the carrier is added optically and in option c), a digital tone is added on one side of the signal spectrum during transmitter DSP.

so that an electrical SSB signal results. This signal is modulated on the optical carrier by an IQ-modulator and an optical SSB signal results. The power of the optical carrier is controlled by the bias of the modulator. The drawback of this approach is, that only half of the bandwidth of the transmitter components can be used for the signal. This problem does not exist for the approach in Fig. 4.2 b). In this case, the unshifted electrical signal is modulated on the optical signal by an IQ-modulator biased at the null point, so that no carrier results in the optical signal. Afterwards, an optical carrier is added on the edge of the spectrum and the resulting signal is treated as an optical SSB signal. This approach, however, requires a second laser or a comb generator, which increases the hardware costs [127]. The third approach in Fig. 4.2 c) adds a digital tone on one side of the spectrum in the transmitter DSP. The IQ-modulator is biased at the null-point, i.e. no additional carrier results in the optical signal. This approach is promising because the full transmitter bandwidth can be used and no additional hardware is necessary. However, the strong carrier component is overlaying the signal during digital-to-analog conversion and modulation, which reduces the available resolution and linear modulation range for the data signal.

For the reception of SSB signals, only half of the bandwidth of the receiver components can be utilized. The selection of the SSB signal generation approach depends on the ratio between available transmitter and receiver bandwidth, as well as on DAC resolution, modulator characteristics and cost sensitivity of the application scenario. If more bandwidth is available at the transmitter than at the receiver, the approach based on driving the modulator with an electrical SSB signal is promising. In less cost-sensitive scenarios, the addition of an optical carrier using a second laser can lead to improved performance. Finally, the approach based on adding a digital tone on one side of the signal spectrum leads to a good trade-off in cost-sensitive scenarios, where the transmitter bandwidth is limited.

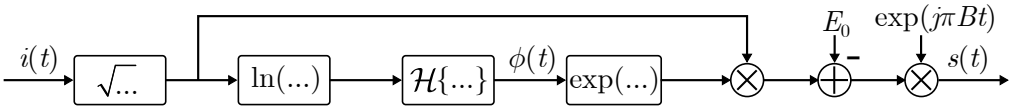

Figure 4.3: Block diagram for the signal recovery by the KK SCOH receiver.

4.2.2 Kramers-Kronig Receiver

The KK receiver has gained great interest in optical communications research in recent years [127–135]. It utilizes the KK-relations [136] to relate the phase and amplitude of certain signals. More specifically, the phase of an SSB signal that fulfills the minimum phase condition can be obtained as [127, 137]

$$\phi(t) = \mathcal{H}\left\{\ln\left[\sqrt{i(t)}\right]\right\}. \tag{4.4}$$

Here, $\mathcal{H}\{...\}$ denotes the Hilbert transform. Given, that the signal has the bandwidth B and the carrier is transmitted at the left edge of the information carrying signal $s(t)$, it can be recovered as [125, 127]

$$s(t) = \left\{\sqrt{i(t)}e^{j\phi(t)} - E_0\right\} e^{j\pi Bt}. \tag{4.5}$$

The steps for the field reconstruction are summarized in the block diagram in Fig. 4.3.

Besides nonidealities related to the implementation of the scheme, the KK receiver perfectly cancels the SSBI [38]. One source of nonidealities is the fact that the KK steps assume an undistorted photocurrent. Since this current is impacted by the bandwidth limitations of the PD and the digital storage oscilloscope (DSO), the requirement is not necessarily fulfilled. Hence a compensation of this effect before application of the KK scheme is necessary to avoid nonideal behavior. However, this compensation was not done for the results shown in this work, since the exact response of these components was not available. Still, the error should be limited, as systems with high bandwidth for the receiver hardware were investigated.

The second source of nonidealities is the spectral broadening introduced by the nonlinear operators, i.e. the ln and square root operation [35]. This spectral broadening can cause spectral aliasing leading to a suboptimal linearization. A solution to reduce the error caused by this phenomenon is digital up-sampling of the signal before applying the KK scheme. However, this leads to an increased DSP complexity so that the amount of oversampling needs to be chosen carefully.

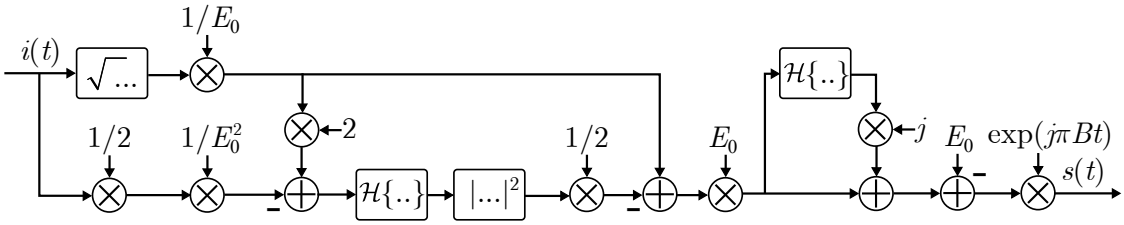

Figure 4.4: Block diagram for the signal recovery by the modified KK SCOH receiver.

Modified Kramers-Kronig receiver

To avoid the issues related to the spectral broadening caused by the nonlinear operations during KK DSP, a modified scheme avoiding these operations was proposed [138]. This is done by adopting mathematical approximations for these operations. Without showing the details on these approximations, which can be found in [138], the modified field recovery is denoted as

$$s(t) \approx \left\{ \sqrt{i(t)} - \frac{E_0}{2} \left[\mathcal{H} \left\{ 2\frac{\sqrt{i(t)}}{E_0} - \frac{i(t)}{2E_0^2} \right\} \right]^2 - E_0 \right\} e^{j\pi Bt}. \tag{4.6}$$

Here, as in Eq. 4.5 a signal with a bandwidth B and a carrier at the left edge of the spectrum is assumed. This relationship still uses a square root operation, but this operation only slightly broadens the spectrum. Therefore, only a relatively small gain can be achieved by digital upsampling, compared to the conventional KK scheme. The DSP steps for the modified KK scheme are summarized in the block diagram in Fig. 4.4. As visible, the signal is expressed in Cartesian coordinates, i.e. as the sum of real and imaginary parts, rather than in polar coordinates as for the conventional KK scheme.

4.2.3 SSBI Cancellation Approaches

Besides the KK receiver and its modifications, several other approaches to mitigate the SSBI in SCOH systems were shown [127, 139–142]. In contrast to the KK receiver, these approaches do not yield a perfect cancellation of the SSBI. However, they can be advantageous in terms of complexity and requirements for oversampling the input signal. Two simple approaches are depicted in Fig. 4.5. The approach in Fig. 4.5 a) is based on the assumption that given a high signal-to-noise-and-distortion ratio the SSBI term can be approximated as [140]

$$|s(t)|^2 \approx \gamma \left| \sqrt{i(t)} + j\mathcal{H} \left\{ \sqrt{i(t)} \right\} \right|^2, \tag{4.7}$$

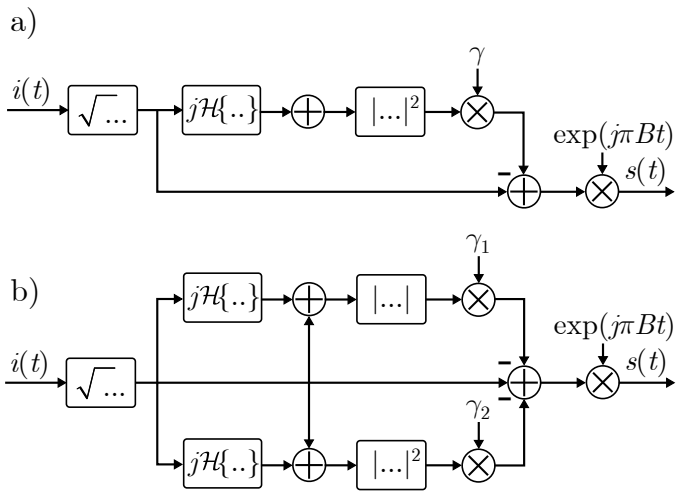

Figure 4.5: Block diagrams for two simple SSBI cancellation schemes based on one-stage (a)) and two-stage (b)) estimation.

where γ is a scaling factor that needs to be optimized. The approach in Fig. 4.5 b) slightly extends this idea by not only considering the absolute squared term in Eq. 4.7, but also the non-squared term with a different scaling factor [139]. According to that, for the approximation the following term results:

$$|s(t)|^2 \approx \gamma_1 \left|\sqrt{i(t)} + j\mathcal{H}\left\{\sqrt{i(t)}\right\}\right|^2 + \gamma_2 \left|\sqrt{i(t)} + j\mathcal{H}\left\{\sqrt{i(t)}\right\}\right|. \tag{4.8}$$

For both approaches, the estimated SSBI term is subtracted from the signal and the result is shifted by the signal bandwidth B to retrieve the approximately SSBI free signal, i.e.

$$s(t) \approx \left\{\sqrt{i(t)} - \gamma \left|\sqrt{i(t)} + j\mathcal{H}\left\{\sqrt{i(t)}\right\}\right|^2\right\} e^{j\pi Bt} \tag{4.9}$$

and

$$s(t) \approx \left\{\sqrt{i(t)} - \gamma_1 \left|\sqrt{i(t)} + j\mathcal{H}\left\{\sqrt{i(t)}\right\}\right|^2 - \gamma_2 \left|\sqrt{i(t)} + j\mathcal{H}\left\{\sqrt{i(t)}\right\}\right|\right\} e^{j\pi Bt}, \tag{4.10}$$

respectively. Both approaches avoid the ln operation that causes the most spectral broadening in the KK receiver [35], so that the oversampling requirements are relaxed. On the other hand, the optimization of the scaling parameters is an additional step that is not required for the KK scheme.

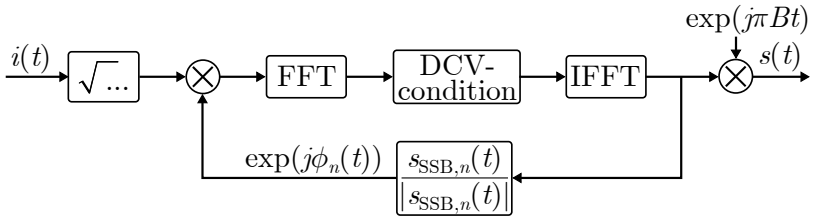

Figure 4.6: Block diagram of the iterative DCV method.

DC-Value Method

In contrast to the two approaches introduced in the previous part, the DC-value (DCV) method is an iterative process to remove the SSBI [141, 142]. It is based on subsequently imposing the SSB and DC properties, resulting from the minimum phase condition, on the signal [141]. The structure of the method is depicted in Fig. 4.6. After taking the square root of the incoming signal intensity $i(t)$, the signal is multiplied with a phase correction term. Then, the signal is shifted into the frequency domain and the DCV condition is applied. This condition imposes the properties of a minimum phase signal on the spectrum and is defined by the operation [142]:

$$\underbrace{S_{\mathrm{SSB},n}(f) = \begin{cases} p\hat{S}_{\mathrm{SSB},n}(f), & \text{for } f > 0 \\ NE_0, & \text{for } f = 0 \\ 0, & \text{else} \end{cases}}_{\text{carrier at the left side of signal spectrum}} \qquad \underbrace{S_{\mathrm{SSB},n}(f) = \begin{cases} 0, & \text{for } f > 0 \\ NE_0, & \text{for } f = 0 \\ p\hat{S}_{\mathrm{SSB},n}(f), & \text{else} \end{cases}}_{\text{carrier at the right side of signal spectrum}} \tag{4.11}$$

Here, $\hat{S}_{\mathrm{SSB},n}(f)$ is the frequency domain representation of the estimated SSB signal, N is the fast Fourier transform (FFT) length, n the iteration number and p a scaling factor, which is chosen according to

$$p = \begin{cases} 2, & \text{for } n = 1 \\ 1, & \text{else.} \end{cases} \tag{4.12}$$

This scaling factor corrects the amplitude, which is halved by suppressing one sideband of the signal, in the first iteration. This way, the convergence speed can be increased [141]. After transforming the corrected signal back to the time domain, the phase correction term for the n^{th} iteration is obtained by

$$e^{j\phi_n(t)} = \frac{s_{\mathrm{SSB},n}(t)}{|s_{\mathrm{SSB},n}(t)|}. \tag{4.13}$$

The more iterations are passed, the closer the optimal SSBI cancellation is approached.

Chapter 5

Experimental and Simulative Investigations

The DSP schemes described in the previous sections are investigated in various simulations and experiments. If available, the properties of the different approaches are shown based on experimental data, as these include all relevant transmission effects. These experimental investigations are supplemented by simulations that allow more flexible adaptations of certain parameters such as component characteristics. First, the investigations on DSP schemes for IM/DD systems, which make up the major part of this work, are shown. The properties of several individual schemes are examined before comparisons between different approaches for certain scenarios are shown. Finally, the advanced DD schemes are studied in detail.

5.1 Approaches for IM/DD Systems

In the following part, the schemes described in Sec. 3 are investigated. First, the setups for the simulations and experiments are described, before the obtained results are shown.

5.1.1 System Setup

For the simulations and experiments shown in the following parts, transmission systems with different hardware have been used. All these systems are based on a similar setup, which is depicted in Fig. 5.1. The signal is generated and prepared in the transmitter DSP before the digital-to-analog conversion is executed by an arbitrary waveform generator (AWG). The analog electrical signal is amplified by a driver amplifier (DA). The voltage swing of the AWG output signal and the gain of the DA need to be chosen carefully to make the signal utilize the desired range of the nonlinear modulator characteristic. For the E/O conversion external intensity modulators are used for the results shown in this work. While most results are based on C-band MZMs, few results are shown based on O-band EMLs. The optical signals are transmitted over SSMF and for some setups,

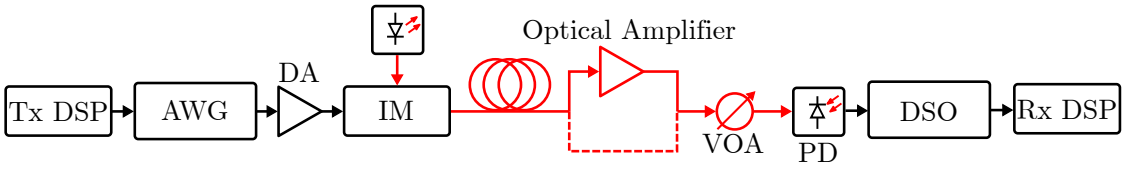

Figure 5.1: General block diagram of the system setups used for simulations and experiments.

Table 5.1: Parameters of the experimental setup used for investigations on various schemes. The systems block diagram is depicted in Fig. 5.1, no optical amplifier is used in this setup.

Component Type	Model Name	Parameters
AWG	Keysight M8194A	3-dB bandwidth: 45 GHz Sampling Rate: 120 GS/s ENOB: $\approx$ 5.5 bits
DA	SHF 810	3-dB bandwidth: >40 GHz Gain: 30 dB
MZM	Oclaro SD-40	3-dB bandwidth: 32 GHz V_π: $\approx$ 5 V
PD	u2t XPD2150R	3-dB bandwidth: >50 GHz
DSO	Keysight UXR1104A	3-dB bandwidth: 110 GHz Sampling Rate: 256 GS/s ENOB: $\approx$ 5 bits

optical amplification using an EDFA or SOA is performed. Then the signal power is controlled by a variable optical attenuator (VOA), before the O/E conversion is done by a PD. The analog-to-digital conversion of the photocurrent is executed by a DSO and finally, the receiver DSP is applied to the digital signal. The exact parameters of the system, such as bandwidth, effective number of bits (ENOB), etc., for the individual results are summarized in tables in the corresponding subsections.

5.1.2 Duobinary Equalization

The DB response is an interesting example of PR signals for high-rate systems due to the strong attenuation of high-frequency components. Additionally, in contrast to other PR filters, the increase in the number of signal levels is limited, so that the equalizer can use signals with this response as a target, even if decisions are performed. The investigations on DB equalization are done on a system with the parameters summarized in Tab. 5.1. The major part of the following results has been published in [106].

To evaluate, whether the DB response is a reasonable target for the equalizer, it is useful to look at the received signal spectra. These are shown for 112 GBd PAM-4 and 90 GBd PAM-6 after back-to-back and 1 km C-band transmission in Fig. 5.2. Note that bandwidth pre-compensation was applied on the signals in the transmitter DSP. The

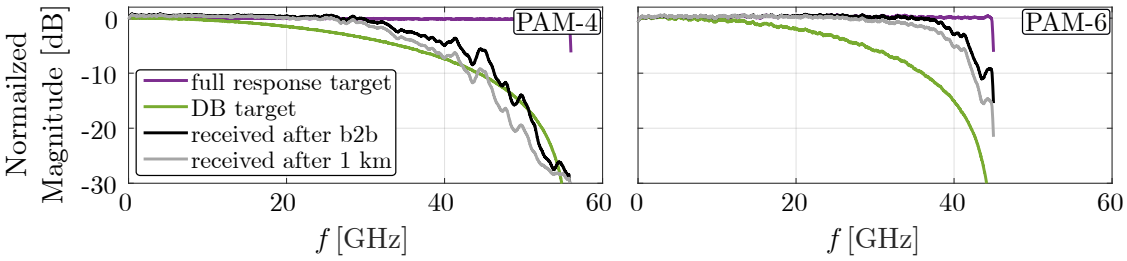

Figure 5.2: Received spectra of bandwidth pre-compensated PAM-4 and PAM-6 signals at a rate of 224/225 Gb/s after back-to-back and 1 km C-band transmission. As a reference, the full response and DB response spectra are shown.

received spectrum of the 112 GBd PAM-4 signal after back-to-back transmission shows strong attenuation at high frequencies. Frequencies of 50 GHz and higher are attenuated by over 20 dB. As no fiber is included in the back-to-back configuration, this strong attenuation is solely caused by bandwidth limitations of the components. As visible in Tab. 5.1, several components have 3-dB bandwidths (BWs) below 50 GHz, leading to these attenuations. After transmission over 1 km SSMF in C-band, the spectrum shows additional attenuation caused by power fading. Although no spectral null lies inside the signal spectrum (first null at 60.6 GHz), the frequencies above 30 GHz experience visible attenuation due to this effect. To evaluate, which response is the better target for equalization, the full response and DB response are shown in the figures. For PAM-4, the received spectra for both transmission distances match the lowpass DB response very well. If the equalizer targets this response, only small adaptations of the received signal are necessary and no noise enhancement occurs. On the other side, the flat full response is far away from the received spectra, so the equalizer would need to amplify the high frequencies significantly, resulting in severe noise enhancement. According to that, significantly better performance can be expected for an equalizer targeting the DB response.

Due to the lower symbol rate that is required to reach 225 Gb/s using PAM-6, a narrower spectrum is transmitted. Therefore, significantly less attenuation of the highest signal frequencies is observed. Again, a small impact of the power fading effect is visible, when comparing the spectra for the back-to-back configuration and 1 km transmission. The comparison between received spectra and the possible equalizer target response leads to different conclusions than for the PAM-4 case. Due to the less significant attenuation, the full response target is closer to the received signal spectra so that a better performance for an equalizer targeting this response can be expected.

It needs to be noted, that besides the attenuation by the channel, a small attenuation of

Table 5.2: Investigated approaches for DB equalization.

Approach	Transmitter DSP	Receiver DSP
(a)	-	VNLE with DB target + VE
(b)	DB pre-coding	VNLE with DB target + mod(M)
(c)	DB pre-coding	VNLE with DB target + VE + mod(M)

the outermost signal frequencies is caused by a Kaiser window filter used as a re-sampling filter in the transmitter DSP. This is the reason, why the magnitude near 45 GHz of the received PAM-6 signal is lower than for the PAM-4 signal.

As described in Sec. 3.1.1, different options for pre-coding and the point, where the DB response is applied, exist. Three relevant approaches are summarized in Tab. 5.2. All of these approaches do not apply the DB response on the signal in the transmitter DSP but assume that it is induced by the channel. Approach (a) does not use any pre-coding. The equalizer, in this case represented by VNLE with memory lengths of $N_1 = 200$, $N_2 = 11$, $N_3 = 11$ for the first to third order, targets the DB signal. This can be realized by filtering the training symbols with the DB response and performing decisions on the extended constellation. As the signal after equalization contains ISI, VE is applied to remove it and to obtain the initial PAM symbols. Approach (b) applies pre-coding in the transmitter DSP. The equalizer again targets the DB response, but due to the pre-coding, the PAM constellation can be retrieved using a mod(M) operation. Finally, approach (c) combines the two former approaches. DB pre-coding is applied in the transmitter DSP, the equalizer targets the DB response and both, VE and the modulo operation are applied. This can be done by adapting VE to output the extended DB constellation instead of PAM symbols. As explained in Sec. 3.1.1, the application of VE can improve the performance by exploiting the known ISI in the signal, while DB pre-coding can help to avoid error bursts.

The three approaches are compared in Fig. 5.3 for 112 GBd PAM-4 and 90 GBd PAM-6 transmission over 1 km. As expected based on the spectra, VNLE targeting the full response leads to poor performance for PAM-4. The BER is above 10^{-1} for all shown received optical power (ROP) values between 0 dBm and 6 dBm. In contrast to this, the performance of the DB approaches is significantly better. Approach (a) outperforms approach (b) for ROPs above 2 dBm. This can be explained by the gain that is obtained by the exploitation of the known ISI in the signal after VNLE by VE. Approach (c) performs better than approach (a) since, in addition to the gain by VE, the number of errors in each error burst is reduced by DB pre-coding. In a system with severe bandwidth

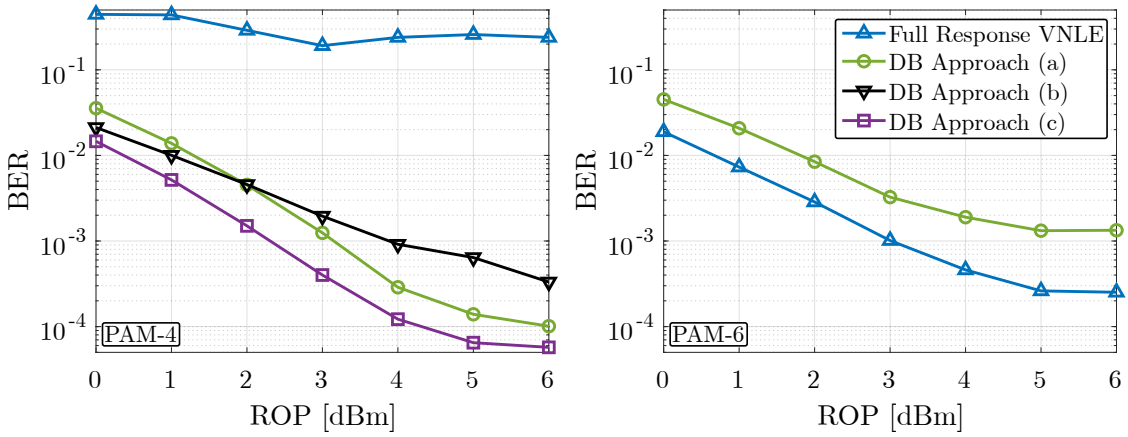

Figure 5.3: Experimental results for 112 GBd PAM-4 and 90 GBd PAM-6 transmission over 1 km comparing full response equalization and different DB response approaches.

limitations, approach (c) is generally superior to the alternatives. However, VE adds additional complexity to the DSP that is avoided in approach (b).

For PAM-6 only the performance of the DB approach (a) is compared to full response VNLE. The reason for this is based on the non-uniform probability of the levels in the PAM-6 constellation (cf. Fig. 2.12). This leads to the issue, that the combination of DB filtering and the mod(M) operation changes the constellation, resulting in degraded performance. As opposed to the results for PAM-4, VNLE targeting the full response signal outperforms the DB response. Comparing the performance between PAM-4 and PAM-6, it is observed that PAM-4 with DB approach (c) shows the best overall performance. However, full response PAM-6 saves DSP complexity, as no pre-coding and VE are applied.

5.1.3 Tomlinson-Harashima Pre-Coding

To evaluate the performance of THP, it is often helpful to compare it to its receiver side counterpart DFE. As explained in Sec. 3.1.2, THP avoids error propagation but suffers from pre-coding loss and other minor impairments. Especially the fact that THP requires channel information at the transmitter makes it only an attractive alternative, if the performance can be improved compared to DFE. The performance of both approaches for different constraints is compared in Fig. 5.4 for 112 GBd PAM-4 transmission. For both schemes two coefficients were used and for FFE, VNLE with memory lengths of $N_1 = 50$, $N_2 = 9$, $N_3 = 9$ for the first to third-order is applied. The parameters for the simulations are chosen according to the lab setup in Tab. 5.1. Only the modulator bandwidth is chosen to be 50 GHz to avoid a limitation of the overall bandwidth by this component. Besides the two contending schemes, the basic DSP stack (Fig. 3.1) is

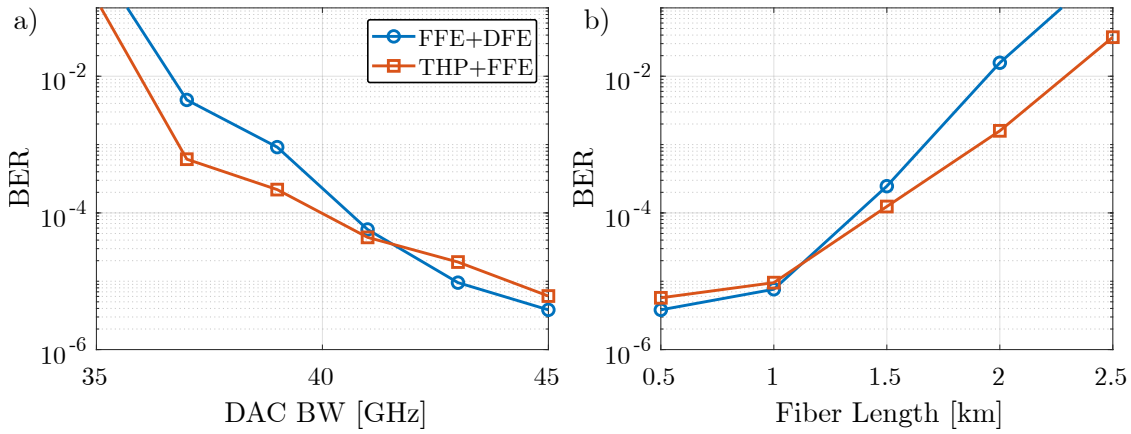

Figure 5.4: Simulative comparison of THP and DFE performance under different constraints for 112 GBd PAM-4 transmission. a) shows the performance of both schemes in dependence on the DAC bandwidth and b) the dependence on the transmission distance in C-band ($D = 17$ ps/nm/km).

applied. Figure 5.4 a) shows the BER in dependence on the DAC bandwidth, which is modeled by a 5^{th}-order Gaussian filter. For strong bandwidth limitations below 41 GHz, THP outperforms DFE clearly. However, if the bandwidth constraints are more relaxed, DFE leads to slightly better performance. A similar trend is observed for the variation of the fiber length and hence the accumulated CD in the link, as shown in Fig. 5.4 b). As C-band transmission with a dispersion parameter of $D = 17$ ps/nm/km is considered, short transmission distances already lead to severe impairments due to power fading. At short transmission distances and therefore low accumulated CD, DFE leads to a slightly better performance than THP. With increasing distance and therefore stronger power fading, a gain by THP is visible. For both impairments, it is observed that THP shows a better relative performance compared to DFE, if the constraints are more severe. Both, a limited bandwidth and strong power fading lead to increased ISI in the signal. Therefore, it can be concluded that strong ISI results in a significant error propagation in DFE. On the other hand, DFE slightly outperforms THP under relaxed constraints, because THP is impaired by the pre-coding loss and due to the low BER, resulting in less potential error propagation.

In addition to the simulative investigations, the performance of THP compared to DFE is evaluated based on experimental data. For the measurements, the setup in Tab. 5.1 was used. Besides the curves for THP and DFE, a lower bound given by an idealized DFE that always feeds back the right symbol, as introduced in Sec. 3.2.2, is shown. Two feedback coefficients are used for all schemes and additionally VNLE with memory lengths of $N_1 = 200$, $N_2 = 11$, $N_3 = 11$ is applied. The results are depicted in Fig. 5.5. For 112 GBd PAM-4 transmission over 1 km in C-band, THP shows a clearly better performance than

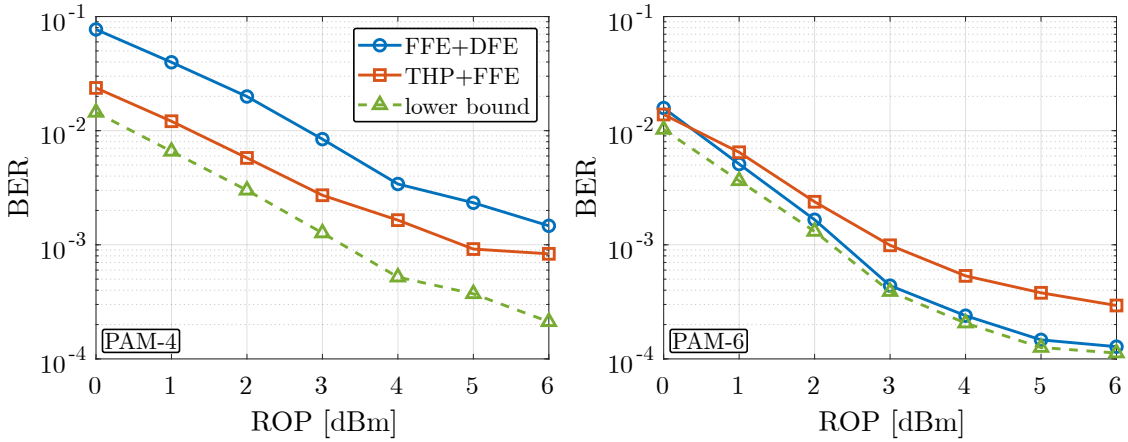

Figure 5.5: Experimental comparison of THP and DFE for 112 GBd PAM-4 and 90 GBd PAM-6 transmission over 1 km. The lower bound is given by the impractical scenario of an DFE that always feeds back the correct decision.

DFE. However, a significant gap between THP and the lower bound is observed. For 90 GBd PAM-6 transmission the situation changes. THP shows worse performance than DFE, which nearly performs as good as the idealized DFE. These results match the observations based on the simulative investigations. The high symbol rate PAM-4 signal is impaired by significant ISI, which is mainly caused by bandwidth limitations and enhanced due to CD. In these scenarios, error propagation plays a significant role and the performance of DFE is strongly limited. THP cannot reach the lower bound, since effects like the pre-coding loss impair the performance. The PAM-6 signal suffers from less ISI due to the reduced symbol rate. This makes the impact of error propagation less severe, as visible when comparing DFE performance with the lower bound. THP can therefore not achieve a relevant advantage over DFE by avoiding error propagation and the aforementioned limitations of THP lead to a decreased performance.

All in all, one can conclude that THP can be a superior alternative to DFE under strong ISI in the received signal, which can be either caused by bandwidth limitations or CD induced power fading. If the conditions are more relaxed, THP can even show worse performance than DFE, making it uninteresting for such scenarios.

THP-FIR Structure

The modified THP structure in Fig. 3.9 can improve the performance compared to conventional THP under certain circumstances. The major part of the corresponding results shown in the following has been published in [68]. To view the effect of the THP-FIR structure, the received spectra after 92 GBd PAM-4 transmission over the setup in Tab. 5.3 for different transmitter DSP approaches are shown in Fig. 5.6 a). The response of

Table 5.3: Parameters of the experimental setup used for investigations on the THP-FIR structure and non-regular PAM mapping. The systems block diagram is depicted in Fig. 5.1, no optical amplifier is used in this setup.

Component Type	Model Name	Parameters
AWG	Keysight M8196A	3-dB bandwidth: 32 GHz Sampling Rate: 92 GS/s ENOB: $\approx$ 5.5 bits
DA	SHF 810	3-dB bandwidth: >40 GHz Gain: 30 dB
MZM	Oclaro SD-40	3-dB bandwidth: 32 GHz V_π: $\approx$ 5 V
PD	u2t XPD2150R	3-dB bandwidth: >50 GHz
DSO	Keysight DSOZ634A	3-dB bandwidth: 63 GHz Sampling Rate: 160 GS/s ENOB: $\approx$ 5 bits

the THP target for the applied coefficient of $\alpha_{\mathrm{THP}} = 0.5$ is given as the desired spectrum. If no pre-compensation is applied after THP, the received spectrum is strongly attenuated and lies clearly below the desired response. If inverse bandwidth pre-compensation is applied, the received signal spectrum is flat up to 30 GHz and drops steeply afterwards. The reason why the spectrum is not flat for higher frequencies is given by the limitation of the pre-compensation to a certain amplification to avoid strong quantization noise. Anyway, the spectrum for this case does not match the desired response well. In case the THP-FIR scheme is combined with inverse bandwidth pre-compensation, the received spectrum matches the target well. According to that, the receiver equalizer has to perform only minor adaptations to retrieve the EDS. This has an impact on the necessary complexity for FFE. Figure 5.6 b) shows the performance after 92 GBd 1 km transmission in dependence on the number of linear FFE coefficients. The memory lengths for the nonlinear coefficients are fixed to $N_2 = 11$ and $N_3 = 11$. For low coefficient numbers $N_{\mathrm{FFE}} \leq 40$, the THP-FIR structure yields a significant gain over conventional THP. This gain shrinks with growing coefficient numbers. This can be explained by the better match of the received spectrum with the target after THP-FIR. This way, fewer FFE coefficients are sufficient to reach a good performance.

To have a closer look at the impact of the THP-FIR structure on the overall performance, the BER as a function of the ROP for 92 GBd PAM-4 1 km measurements is shown in Fig. 5.7. The approach is compared to FFE only, FFE combined with DFE and conventional THP with FFE. For FFE, VNLE with either $N_1 = 40$ or $N_1 = 200$ linear coefficients and $N_2 = 11$ as well as $N_3 = 11$ is applied. In case of $N_1 = 40$ VNLE only shows the

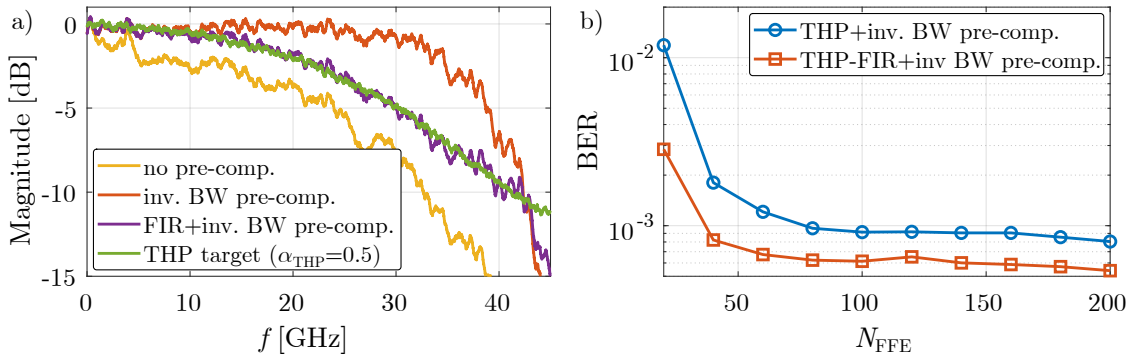

Figure 5.6: Investigations on the THP-FIR structure transmitting the EDS. a) shows the received spectra for 92 GBd PAM-4 back-to-back transmission and b) shows the impact of the linear FFE coefficient number on the performance for 1 km transmission.

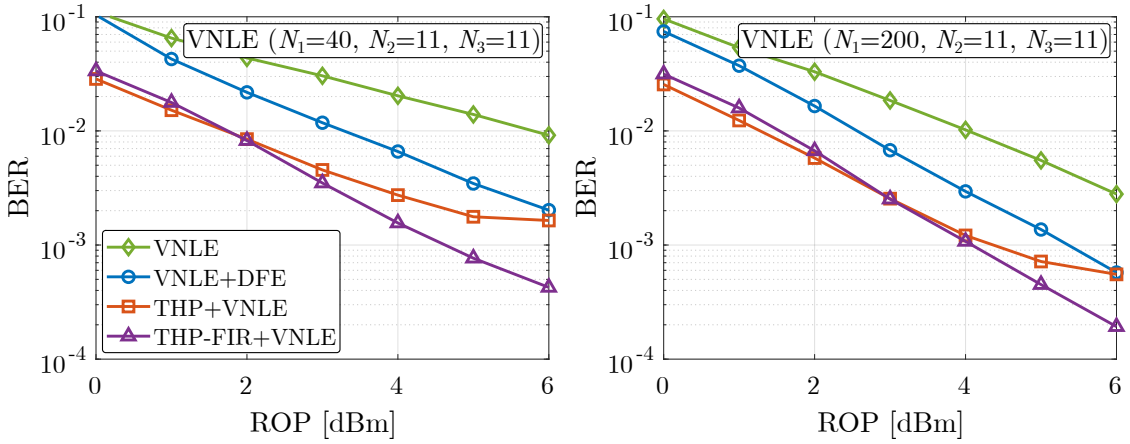

Figure 5.7: Experimental results on the THP-FIR structure compared to conventional schemes. 92 GBd PAM-4 is transmitted over 1 km in C-band.

worst performance, followed by DFE. Conventional THP and the THP-FIR approach show a similar performance up to a ROP of 2 dBm and the combined structure shows a performance gain for higher ROPs. For $N_1 = 200$ the order of the DSP approaches is similar. However, the combined structure only performs better than conventional THP for ROPs above 5 dBm. The relative performance of the THP approaches is much more similar for a long receiver equalizer. The explanation is the same as for the previous findings: the better match of the received spectrum to the target spectrum allows a better performance of the THP-FIR approach for short FFE, while a high memory length allows mitigating the performance gap for conventional THP.

5.1.4 Non-Regular PAM Mapping

The impact of nonlinearities caused by the combination of the MZM characteristic and DD gets more severe, if a higher-order PAM constellation is used. Therefore, PAM-8 is chosen for the related investigations which were done experimentally based on a system with the

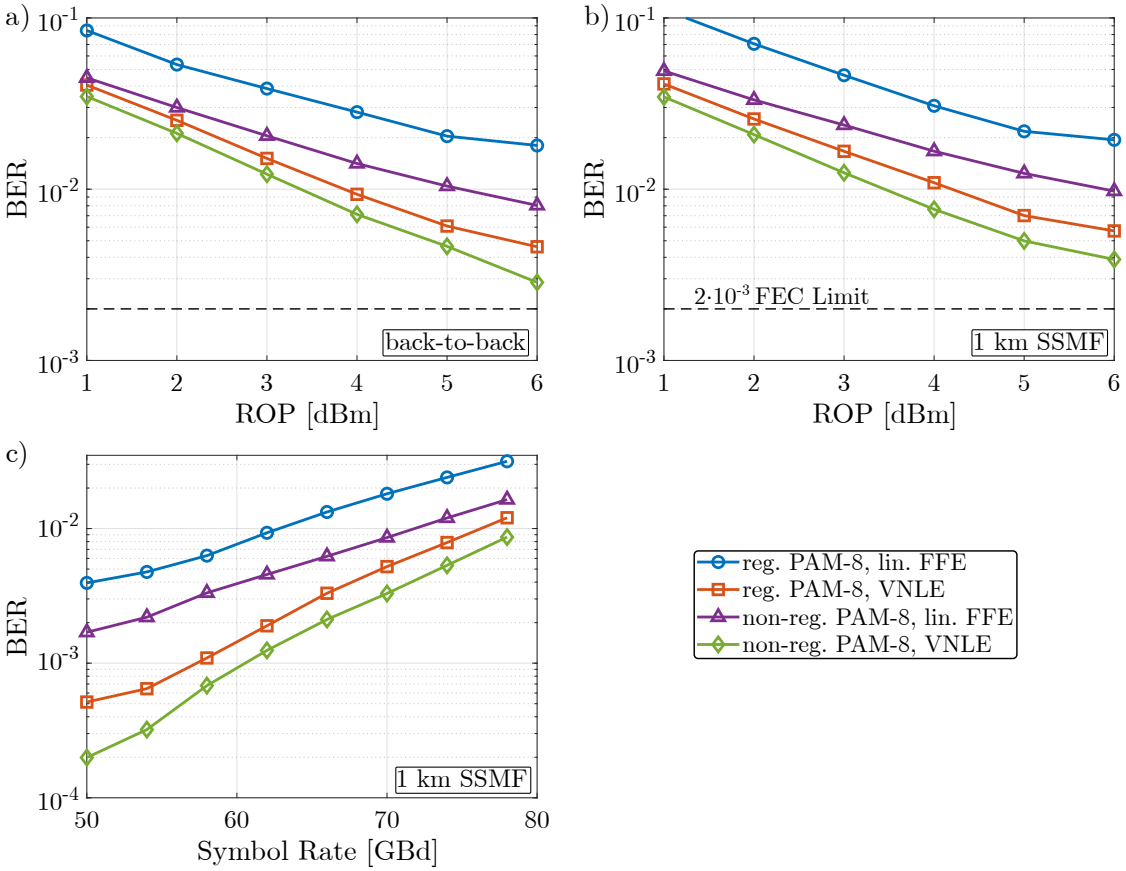

Figure 5.8: Experimental results comparing the performance of conventional and non-regular PAM-8. a) shows the BER over the ROP for a back-to-back configuration and b) for 1 km C-band transmission at a symbol rate of 70 GBd. c) shows the performance at a varying symbol rate for 1 km transmission.

parameters summarized in Tab. 5.3. The corresponding results shown in the following have been published in [97]. Figure 5.8 a) shows the BER as a function of the ROP for 70 GBd transmission in a back-to-back configuration. Four options are considered: regular PAM-8 with linear FFE ($N_{\mathrm{FFE}} = 50$) and with VNLE ($N_1 = 50, N_2 = 9, N_3 = 9$), as well as non-regular PAM-8 with both equalizer concepts. For all options, the bias point is fixed to be slightly below the quadrature point ($u_{\mathrm{bias}} \approx -0.4V_\pi$) and the voltage swing at the AWG output was individually optimized by sweeping through a range of values and choosing the optimum with respect to the resulting BER. Regular PAM-8 combined with linear equalization shows the worst performance and a BER below 10^{-2} is not reached. Changing the symbol constellation to a non-regular spacing significantly improves the performance and the BER is approximately halved. VNLE shows a clear advantage over linear FFE for the given scenario. Considering a regular PAM-8 mapping, the BER can be reduced to a quarter. The gain by VNLE is higher than the gain by changing to a non-regular constellation which can be explained by additional sources of

nonlinearities in the system, such as electrical amplifiers, and by the capability of VNLE to equalize nonlinearities with memory. The latter result from the fact that the signal already suffers from ISI due to bandwidth limitations, before nonlinear effects occur. An additional gain can be achieved by combining non-regular PAM-8 with VNLE. This gain is possible because VNLE is limited to the third order and therefore the nonlinearities cannot be approximated ideally. For 1 km transmission in C-band, similar results are observed. The performance of all schemes is slightly degraded due to CD, but non-regular PAM-8 again shows a clear gain over the conventional format.

Fig. 5.8 c) shows the performance of the four options at varying symbol rates between 50 GBd and 78 GBd. Transmission over 1 km and a ROP of 6 dBm were considered for these results. For all symbol rates, the non-regular mapping improves the performance. All in all, non-regular PAM constellations seem to be an effective option to improve the performance of the considered short-reach IM/DD systems. This concept is especially attractive because no additional complexity results compared to conventional PAM once the constellation is optimized.

5.1.5 Volterra Nonlinear Equalization

The experimental investigations on VNLE were done based on the components summarized in Tab. 5.1. High memory lengths for the higher order kernels of VNLE lead to enormous complexity as shown in Fig. 3.13 for the third order, so optimization of this parameter is crucial. Figure 5.9 shows the impact of the coefficient number for the first to third order based on 90 GBd PAM-6 back-to-back data. These results have already been published in [96]. It needs to be noted that the bias voltage as well as the drive signal voltage swing were optimized for third-order VNLE so that the linear and second-order FFE performance is not necessarily the optimum. The linear coefficient number C_1 is investigated in Fig. 5.9 a). The BER decreases up to 120 coefficients and thus this number is chosen as optimum. In Fig. 5.9 b) the impact of the second-order coefficients is shown for $C_1 = 120$ linear coefficients. Few coefficients are sufficient to decrease the BER by a factor of more than three. Increasing the coefficient number further does not lead to a relevant gain. For further investigations, $C_2 = 21$ second-order coefficients are considered, which corresponds to a memory length of $N_2 = 6$. The impact of the third-order coefficients is even more significant, as shown in Fig. 5.9 c). A number of $C_3 = 165$ seems to offer a good trade-off between performance and complexity and decreases the BER by a factor of more than 10. Figure 5.9 d) shows the BER as a function of the ROP for linear FFE as well as second and third-order VNLE with the coefficient numbers chosen based on Fig. 5.9 a)-c). Here, $\mathbf{C}$ is a vector containing the

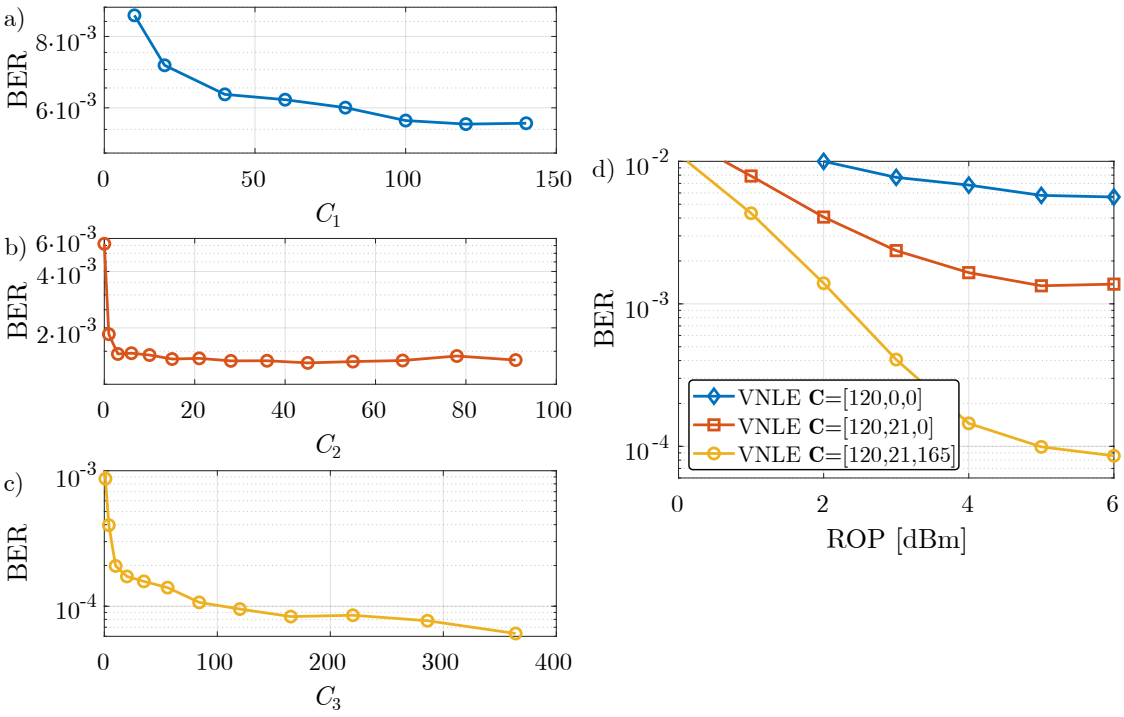

Figure 5.9: Optimization of the VNLE coefficient numbers for 90 GBd PAM-6 transmission in a back-to-back configuration. a) shows the performance in dependence on the linear coefficient number, b) considers the second-order coefficients and c) the third-order coefficients. d) shows the BER over ROP for the optimized coefficient numbers.

number of coefficients for the respective order. For all ROPs a significant improvement by nonlinear equalization is observed.

Structural Complexity Reduction

To evaluate the structural complexity reduction approaches, it is useful to look at the performance-complexity trade-off compared to conventional full VNLE. While the performance is quantified by the BER, the number of coefficients can be used as a complexity measure. This trade-off is investigated for the third-order coefficients, as these make up the largest part of the overall equalizer complexity for the given example. The corresponding results have been published in [96]. Figure 5.10 shows the relationship of BER and third-order coefficient number C_3 for different complexity reduction schemes. The number of linear coefficients is $C_1 = 120$ and of the second-order coefficients $C_2 = 21$ for these results.

Fig. 5.10 a) shows the comparison of full VNLE and 2S VNLE. While no significant performance improvement can be achieved for low coefficient numbers, several points below the reference curve are reached for coefficient numbers above 50. This improved trade-off leads to the conclusion that coefficients based on two different samples include the most relevant ones to overcome third-order nonlinearities. In Fig. 5.10 b) MP VNLE

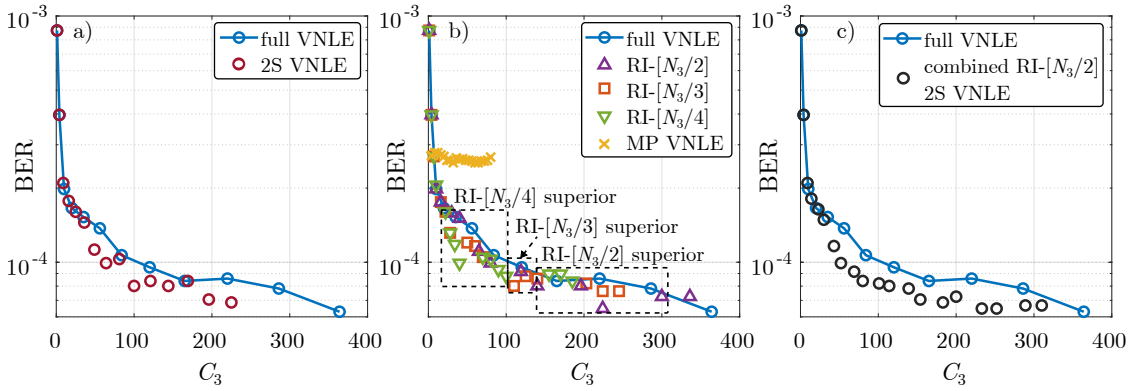

Figure 5.10: Trade-off between performance and complexity for full VNLE and structural complexity reduction approaches. a) shows results for the 2S VNLE, b) for MP and RI-$d_{\max}$ VNLE and c) for the combination of 2S and RI-$d_{\max}$. The coefficient numbers for the first and second order are $C_1 = 120$ and $C_2 = 21$, respectively.

and RI-$d_{\max}$ VNLE are considered. The performance of MP VNLE is nearly constant over the coefficient number. While few coefficients improve the performance by a factor of more than three compared to second-order VNLE, higher memory lengths do not bring additional gain. The trade-off between performance and complexity cannot be improved compared to full VNLE. The RI-$d_{\max}$ VNLE is shown for different parameters, namely $d_{\max} = C_3/4$, $d_{\max} = C_3/3$ and $d_{\max} = C_3/2$. The smaller $d_{\max}$ is chosen, the stronger the complexity is reduced since only coefficients with a small spacing among participating samples are considered. For $d_{\max} = C_3/4$ a good performance at a relatively low complexity can be reached. For third-order coefficient numbers below $C_3 = 100$ an improved performance is reached compared to full VNLE. A spacing of $d_{\max} = C_3/3$ leads to an improved trade-off for slightly higher coefficient numbers and $d_{\max} = C_3/2$ outperforms full VNLE for coefficient numbers of $C_3 > 130$. Note, that the points with the highest complexity for the RI-$d_{\max}$ VNLE are obtained by increasing the memory length to higher values than considered for full VNLE. The reason why some points with a higher memory length show a worse performance compared to smaller memory lengths is that unnecessary additional coefficients can distort the output. These coefficients may not exactly converge to zero and therefore add noise-like distortions. Figure 5.10 c) shows the combination of RI-[$C_3/2$] and 2S VNLE. This combination achieves a better trade-off between performance and complexity than full VNLE for all considered coefficient numbers of $C_3 > 30$. Therefore, it is generally advantageous to apply this structural complexity reduction approach in the given scenario. Comparing the results for the combined complexity reduction approach to the individual approaches shows a general advantage by combining 2S and RI-$d_{\max}$ VNLE.

Fig. 5.11 shows the BER as a function of the ROP for different third-order VNLEs.

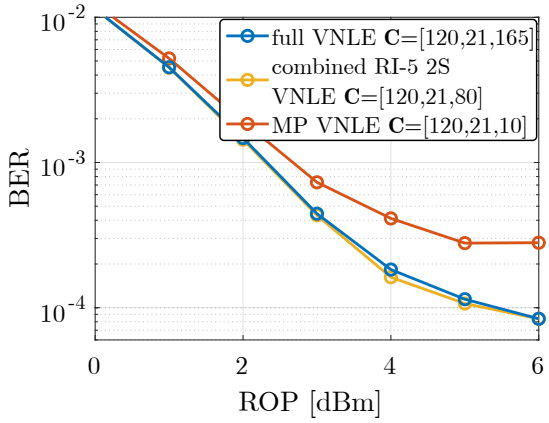

Figure 5.11: Comparison of full VNLE, combined RI-$d_{\max}$ 2S VNLE and MP VNLE for 90 GBd PAM-6 back-to-back transmission.

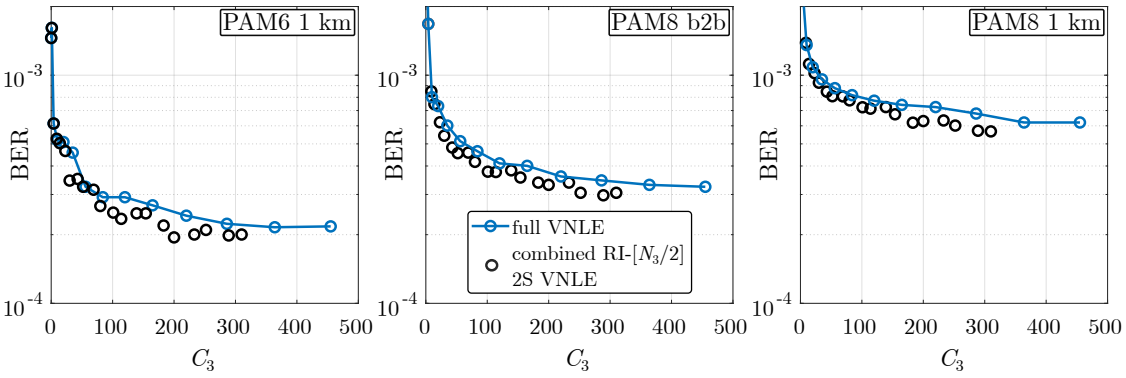

Figure 5.12: Trade-off between performance and complexity for full VNLE and combined RI-$d_{\max}$ 2S VNLE. 90 GBd PAM-6 transmission over 1 km as well as 75 GBd PAM-8 for back-to-back and 1 km are shown.

Combined RI-$d_{\max}$ 2S VNLE with a memory length of $N_3 = 10$ results in $C_3 = 80$ third-order coefficients. Full VNLE with a memory length of $N_3 = 9$ uses approximately twice the number of coefficients. The performance of both schemes is identical despite the clear difference in complexity. MP VNLE with a memory length of $N_3 = 10$ shows a degraded performance compared to the other candidates. However, only $C_3 = 10$ third-order coefficients are used, which implies a significant complexity reduction. It depends on the particular application if the performance penalty can be accepted.

The trade-off between performance and complexity for combined RI-$d_{\max}$ 2S VNLE is further investigated based on additional data. Figure 5.12 shows the comparison with full VNLE for 90 GBd PAM-6 transmission over 1 km as well as 75 GBd PAM-8 back-to-back and 1 km transmission. For all the considered scenarios, the combined structural complexity reduction approach shows the capability of improving the trade-off. Therefore, it can be concluded that the third-order nonlinearities in the investigated system can be

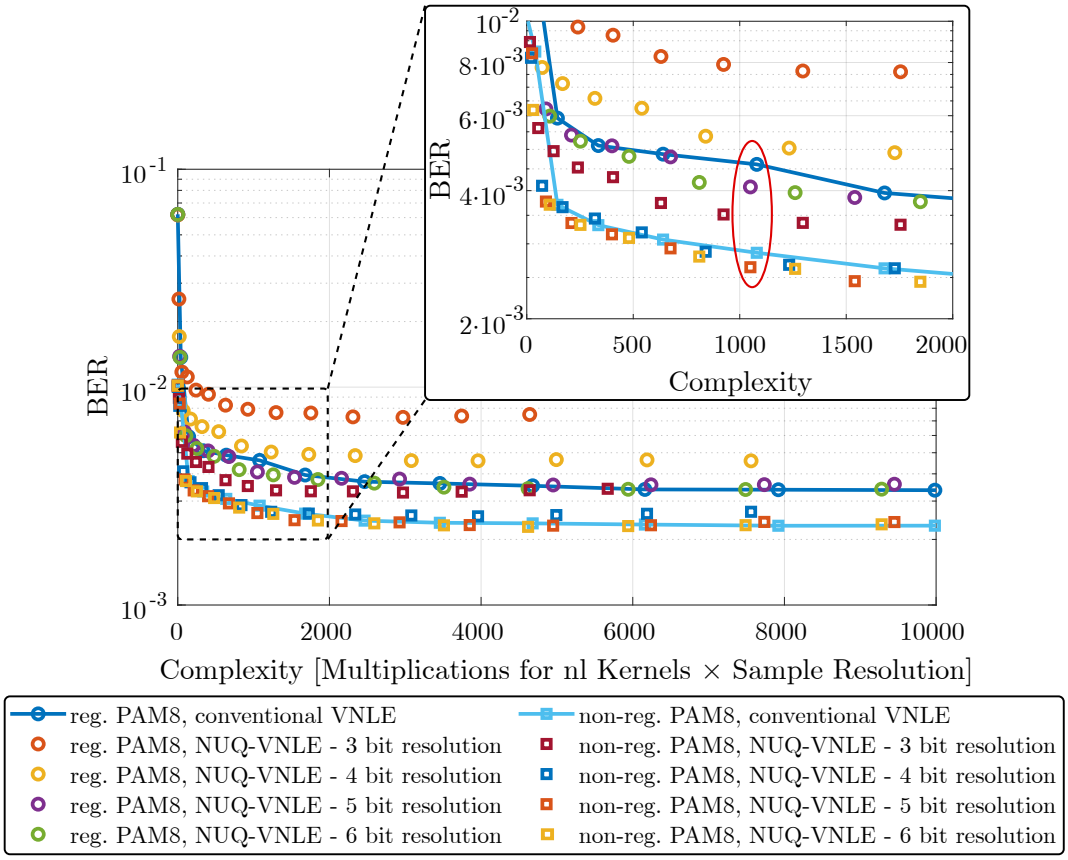

Figure 5.13: Comparison of complexity and performance for full resolution VNLE and NUQ VNLE. The red circle in the inset shows the selected points for further investigation.

well approximated without using coefficients with a large spacing among participating samples as well as any cross terms with three different samples.

Non-uniform Quantization

Instead of reducing the number of coefficients, NUQ VNLE aims at a reduction of the average resolution per processed sample. This way, the complexity measured as the product of the number of multiplications for the kernels and the sample resolution can potentially be reduced compared to VNLE working with a signal at the full available resolution. A comparison of performance and complexity is shown in Fig. 5.13 for experimental 70 GBd PAM-8 back-to-back data obtained on a system with the parameters summarized in Tab. 5.3. The results have been published in [68]. Besides regular PAM-8 also non-regular PAM-8 is considered. For a simple comparison, the NUQ VNLE uses a fixed number of ten central linear coefficients with an 8 bit input signal, while the remaining linear and nonlinear coefficients work with 3 - 6 bit input samples. Additionally, only VNLEs with an equal memory length for second and third-order coefficients are considered. While the full resolution VNLE uses $N_1 = 50$ linear coefficients, the number of linear coefficients

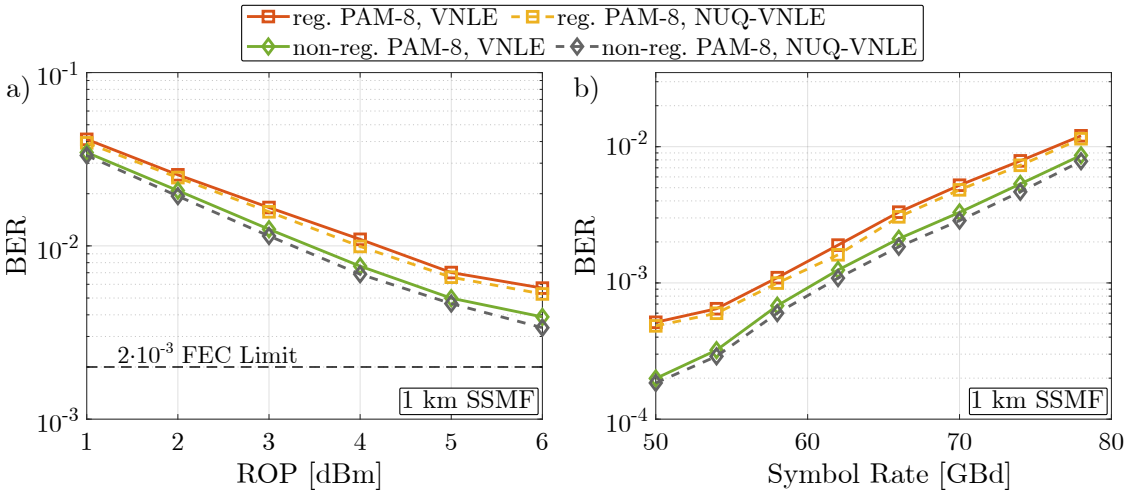

Figure 5.14: Experimental results for 70 GBd PAM-8 transmission over 1 km comparing full resolution VNLE and NUQ VNLE.

in NUQ VNLE is adjusted depending on the resolution, so that the same complexity is obtained. The results show, that several points slightly below the reference curve of VNLE working with 8 bit resolution exist. This means NUQ VNLE reduces the complexity at a certain performance. The red circle in the inset of Fig. 5.13 shows a group of points used for further investigations. In this case for both, regular and non-regular PAM-8, the performance is improved at a slightly decreased complexity.

A comparison of VNLE working with full resolution input samples and NUQ VNLE with parameters according to the previous optimization is shown in Fig. 5.14 for PAM-8 transmission over 1 km. Figure 5.14 a) visualizes the BER as a function of the ROP for 70 GBd. For both, regular and non-regular PAM-8, a small gain is achieved by NUQ VNLE while slightly decreasing the complexity compared to conventional VNLE. Figure 5.14 b) shows results for different symbol rates between 50 GBd and 78 GBd. Again, a constant gain by NUQ VNLE is observed. Even though the gains achieved by NUQ VNLE are small, they can be a useful contribution to make the application of VNLE more practical. This approach could be combined with structural coefficient reduction schemes to reduce the complexity more significantly.

5.1.6 Noise Whitening Filter

The impact of a noise whitening FIR filter combined with VE is experimentally investigated on the setup with the parameters in Tab. 5.1. For the investigations, 112 GBd PAM-4 and 90 GBd PAM-6 transmission in an optical back-to-back configuration are considered. The major part of these results has been published in [106]. To visualize the effect of noise whitening filtering, it is helpful to view the noise spectra at different

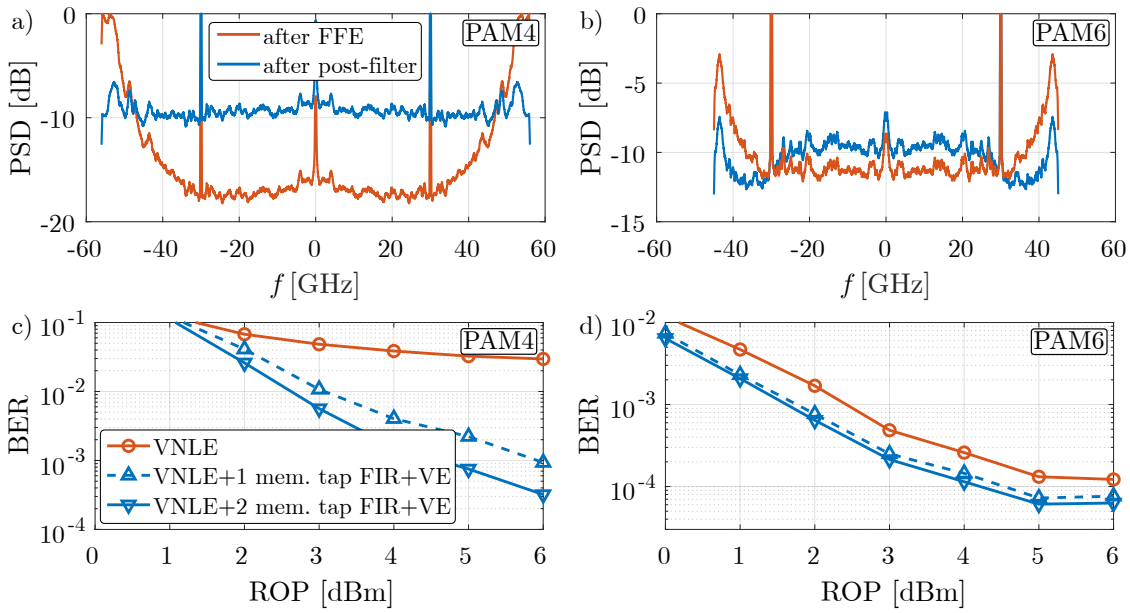

Figure 5.15: Experimental investigations on noise whitening filters. a) and b) show the noise spectra after FFE and the whitening post-filter for 112 GBd PAM-4 and 90 GBd PAM-6 and c) and d) show the resulting BER over the ROP.

stages. These spectra after FFE and after a two memory coefficient post-filter are shown in Fig. 5.15 a) and b) for PAM-4 and PAM-6, respectively. The noise is estimated to be the difference between the samples after the respective DSP stage and the corresponding training symbols. As the samples after the noise whitening filter contain ISI, the same filter function needs to be applied to the training symbols to calculate the noise. Note, that all spectra contain considerable DAC clock tones at 30 GHz, which corresponds to a quarter of the DAC sampling rate. These can be removed in DSP to further improve the performance. The noise after FFE in case of 112 GBd PAM-4 (Fig. 5.15 a)) shows a strong amplification of higher frequencies above 40 GHz. The noise at the outermost signal frequencies is enhanced by more than 15 dB compared to the inner frequencies. For this scenario, poor transmission performance can be expected. The application of a noise whitening FIR filter, however, results in a significantly flatter noise power spectral density (PSD). The spectrum of the 90 GBd PAM-6 signal is narrower so that the signal suffers from less severe attenuations by bandwidth limitations. As a result, the noise enhancement in the signal after FFE, as shown in Fig. 5.15 b), is weaker than for PAM-4. The application of a post-filter can improve the flatness of the noise spectrum, but a less significant impact on the performance compared to the PAM-4 signal can be expected.

The results for the transmission of 112 GBd PAM-4 and 90 GBd PAM-6 in terms of the BER as a function of the ROP are shown in Fig. 5.15 c) and d). As expected based on

Table 5.4: Coefficients for the noise whitening post-filters optimized using the Burg algorithm for 112 GBd PAM-4 and 90 GBd PAM-6 transmission.

Modulation Format	1 memory tap FIR	2 memory tap FIR
PAM-4	$\mathbf{l} = [0.78]$	$\mathbf{l} = [0.58, -0.25]$
PAM-6	$\mathbf{l} = [0.36]$	$\mathbf{l} = [0.31, -0.14]$

the strong noise enhancement in the PAM-4 signal after FFE, poor performance results, if no post-filter is applied. Applying an FIR filter with only one memory coefficient and removing this ISI with a four state VE results in a significant improvement of the performance. At an ROP of 6 dBm the BER is reduced by a factor of 20. Using a second memory tap additionally improves the performance by a factor of more than two. The coefficient values that were optimized using the Burg algorithm (cf. Sec. 3.2.3) are summarized in Tab. 5.4. The gain achieved for the PAM-6 format is significantly smaller, as expected based on the less significant noise enhancement. While the first memory coefficient leads to a constant gain over all ROPs, the second memory tap hardly improves the performance. Comparing the FIR coefficient values in Tab. 5.4 shows that clearly smaller coefficient values were calculated for PAM-6. This explains the less severe impact on the performance.

Decomposition of Post-filter Coefficients

Depending on the coefficient acquisition approach, it might make sense to decompose the noise whitening filter coefficients into a partial response equalization with a subsequent post-filter. The impact on the performance for 2 km PAM-4 transmission based on the setup in Tab. 5.1 is shown in Fig. 5.16 a). The VNLE uses memory lengths of $N_1 = 200$, $N_2 = 11$ and $N_3 = 11$ and the weights are acquired based on training based LMS with 4096 training symbols followed by decision-directed updates. Two DSP options are compared: full response VNLE followed by a 2-coefficient post-filter and DB VNLE followed by a 1-tap post-filter. For both approaches, VE with the same number of states is used to recover the ISI free PAM-4 signal. If perfect equalizer convergence is assumed, the approach based on full response equalization and 2-tap post-filter has the advantage that both coefficients can be adjusted, while one memory coefficient is fixed for the DB VNLE. However, significantly better performance is observed for the DB equalization approach. The advantage of this scheme is given by the better match between received signal and equalizer target. This way, less adjustment of the coefficient weights is necessary and the decision-directed updates lead to better results since the error rate after the equalizer is significantly lower. Exemplary spectra after equalization and after a post-filter for 88 GBd are shown in Fig. 5.16 b). If the equalizer targets the full response, strong noise

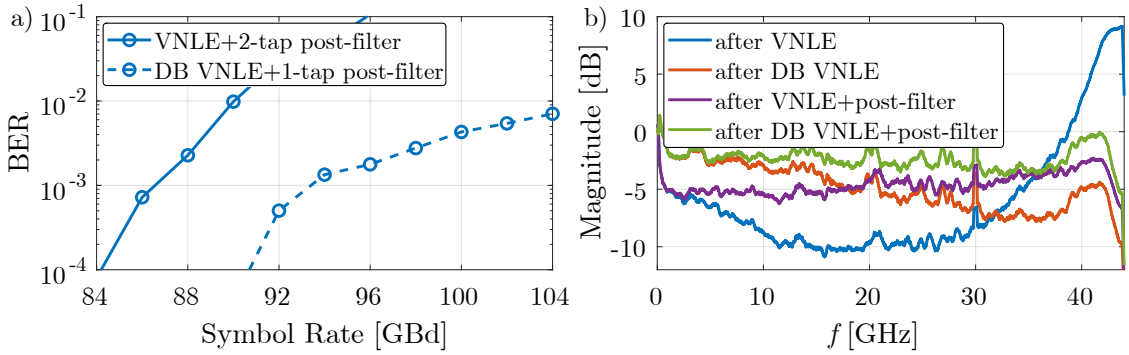

Figure 5.16: Impact of the decomposition of a 2-coefficient post-filter based on 2 km PAM-4 experimental data. a) shows the BER as a function of the symbol rate and b) shows different spectra for 88 GBd.

enhancement is observed. Decisions on a signal with such a strong noise enhancement are not reliable. Even though the 2-tap post-filter can whiten the noise, the performance is limited by the poor VNLE convergence. For the DB target, on the other hand, no noise enhancement is visible.

5.1.7 Weighted DFE

The first investigation on WDFE focuses on the coefficient update in case the equalizer is converged based on decision-directed LMS. As explained in Sec. 3.2.2, two options to calculate the error used for the coefficient update are available: either the hard decision $\hat{x}_{\text{out}}(k)$ is used as in Eq. 3.13 or the weighted decision $\overline{x}_{\text{out}}(k)$ is utilized (Eq. 3.35). To compare these two options, 90 GBd PAM-4 data after 2 km transmission is used. The experimental setup is based on the parameters in Tab. 5.1. The results in Fig. 5.17 show the BER over the number of DFE coefficients N_{DFE} for the two error calculation options and different WDFE upper limits I_{max}, while the remaining WDFE parameters are fixed to $a_s = 5$ and $b_s = 0.2$. The FFE part of the applied equalizer has memory lengths of $N_1 = 200$, $N_2 = 11$ and $N_3 = 11$. Normalized LMS was applied during training mode with 2048 training symbols and $\mu = 10^{-4}$ during decision-directed mode. When comparing the performance for varying upper limits, it is visible that the number of coefficients has a stronger impact on the performance, if a lower upper limit is chosen. While the BER for $I_{\text{max}} = 0.4$ can be reduced by a factor of four by increasing the number of feedback coefficients from $N_{\text{DFE}} = 2$ to $N_{\text{DFE}} = 8$, the impact of the coefficient number is much less severe for $I_{\text{max}} = 1$. Regarding the two error calculation options, the approach based on the hard decision leads to better performance for all considered scenarios. The performance improvement is larger, if a lower upper limit is used. In this case, the deviation between hard decision and weighted decision is large, while the difference is small for $I_{\text{max}} = 1$. As it generally appears advantageous to calcu-

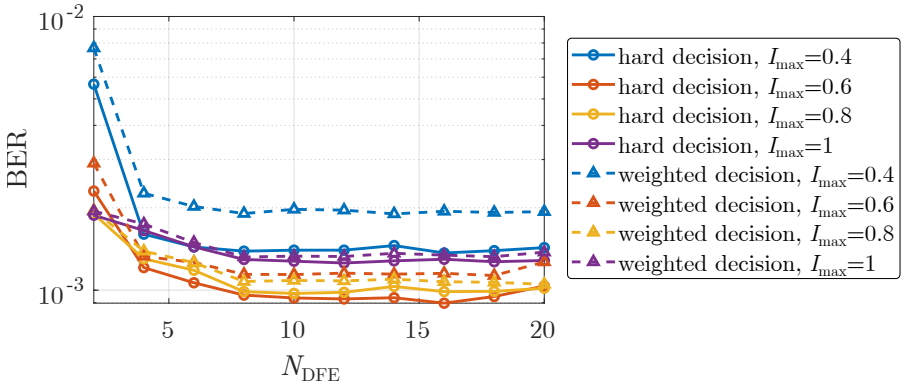

Figure 5.17: Comparison of the WDFE performance obtained with decision directed LMS equalizers using either the hard decision $\hat{x}_{\text{out}}(k)$ or the weighted decision $\overline{x}_{\text{out}}(k)$ for the error calculation. The results are based on experimental 90 GBd PAM-4 data transmitted over 2 km.

late the error based on the hard decision, this approach is applied for further investigations.

To evaluate the performance of WDFE, it is obvious to compare it to conventional DFE and THP. This comparison is shown in Fig. 5.18 for PAM-4 transmission based on the setup parameters in Tab. 5.1. These investigations have already been published in [102]. Results for a back-to-back configuration and rates between 110 GBd and 136 GBd are shown in Fig. 5.18 a). The combination of FFE based on VNLE with memory lengths of $N_1 = 200$, $N_2 = 11$ and $N_3 = 11$ and conventional DFE with two coefficients shows poor performance for the higher rates. WDFE based on the function $f_{\text{I1}}(\gamma_k)$ (Eq. 3.32) cannot reach a visible improvement. A slight gain is achieved by applying the WDFE function $f_{\text{I2}}(\gamma_k)$ (Eq. 3.33), but still a huge performance gap compared to THP is visible. This gap increases with growing symbol rate, i.e. with growing ISI due to bandwidth limitations. The lower bound is again given by the unpractical scenario of DFE that always feeds back the correct symbol, i.e. the penalty by error propagation is not existent. For 2 km transmission and symbol rates between 86 GBd and 102 GBd, as shown in Fig. 5.18 b), the comparison of the different approaches looks similar. Conventional DFE shows significantly worse performance than THP at higher symbol rates again. When comparing DFE and WDFE, a gain by WDFE can be observed at rates above 96 GBd. For the different WDFE functions, the sigmoid function $f_{\text{I2}}(\gamma_k)$ with the adjustable upper limit shows improved performance. The gain over conventional DFE, however, is still small and THP is the more attractive solution for these constrained conditions.

To show the dependence of the WDFE performance on its parameters, Fig. 5.18 c) shows an exemplary optimization of the compression factor b_s and the upper limit $I_{\max}$ for the function $f_{\text{I2}}(\gamma_k)$. This optimization is done for 100 GBd PAM-4 data transmitted over 2 km. The lowest BER is reached for values of $b_s \approx 0.1$ and $0.5 \leq I_{\max} \leq 0.65$. It

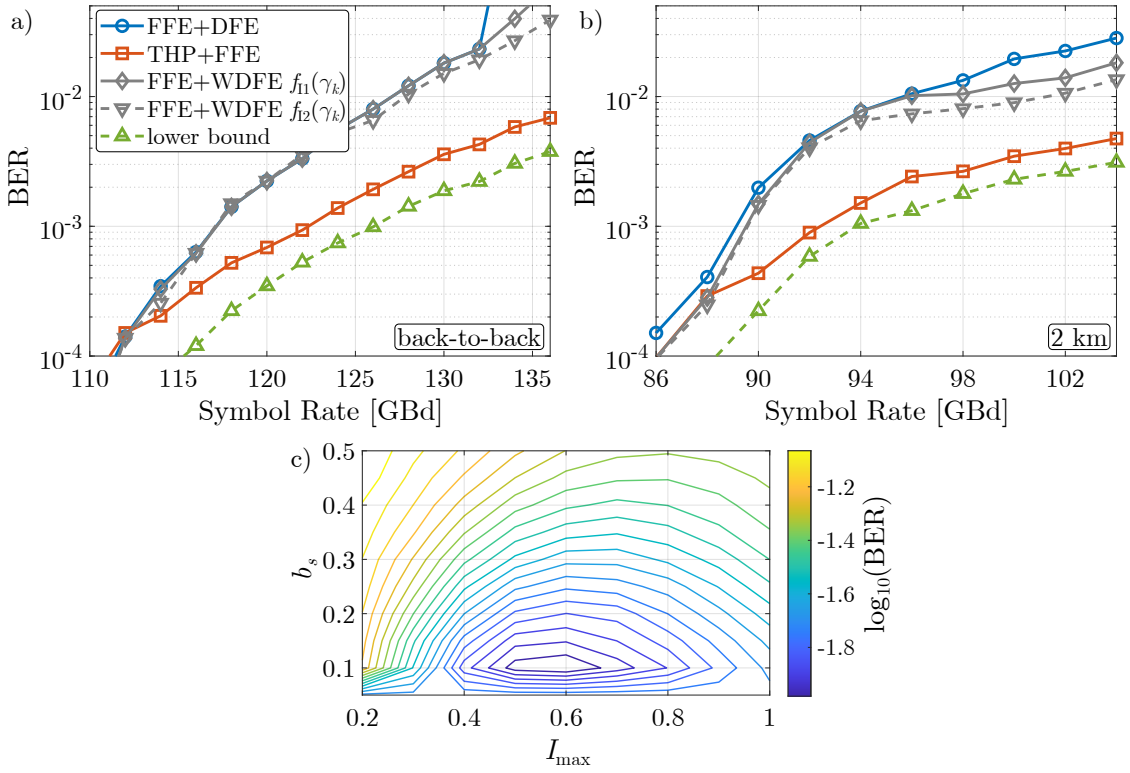

Figure 5.18: Experimental investigations on WDFE. a) and b) show the performance for different PAM-4 symbol rates compared to established schemes for back-to-back and 2 km transmission. c) exemplary shows the optimization of the WDFE parameters for 100 GBd PAM-4 transmission over 2 km, where the steepness is fixed to $a_s = 5$.

is visible that the optimization of the upper limit improves the performance. However, to reach a performance able to compete with THP, WDFE needs to be combined with additional DSP, as shown in the next part.

Combinations with Noise Whitening Filter and DB Equalization

As explained in Sec. 3.2.5 WDFE or PDFE with a low upper limit $I_{\max}$ or a low ratio r_c, respectively, can suffer from noise enhancement in the equalized signal. Therefore, a combination with a noise whitening filter and VE can be helpful in scenarios with heavy constraints by bandwidth limitations and CD-induced power fading. This combination is investigated for WDFE based on the function $f_{I2}(\gamma_k)$ using experimental 92 GBd PAM-4 data transmitted over 2 km (parameters according to Tab. 5.1). Figure 5.19 a) compares the performance of different approaches in dependence on the number of noise whitening filter memory coefficients. The results in this subfigure have been published in [102]. Applying only FFE results in poor performance which can only be slightly improved by applying a post-filter. As seen in previous results, DFE leads to better performance but is clearly outperformed by THP in this scenario. Both schemes do not benefit from a

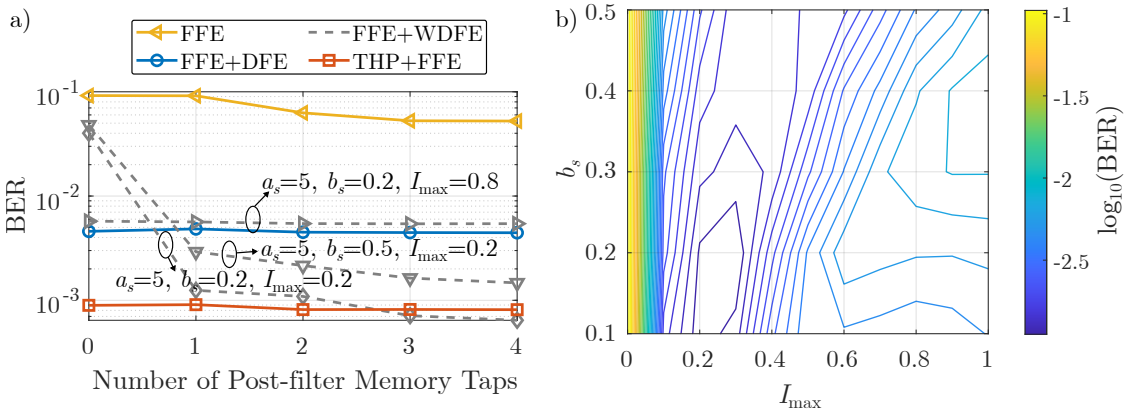

Figure 5.19: Results for the combination of WDFE and a noise whitening FIR filter combined with VE. a) shows the BER in dependence on the number of post-filter coefficients for 92 GBd PAM-4 data transmitted over 2 km and b) shows the optimization of the WDFE parameters considering a post-filter with one memory tap.

combination with a noise whitening filter, because they avoid noise enhancement. In addition to these approaches, WDFE with different parameters is shown. For a high upper limit of $I_{\max} = 0.8$ a slightly worse performance than for conventional DFE is achieved and post-filtering does not improve the performance. For a low upper limit of $I_{\max} = 0.2$, however, the application of a noise whitening filter yields a significant gain. While the performance is poor without a post-filter, a single memory tap is sufficient to reach a better performance than conventional DFE. For $b_s = 0.2$ the best performance is reached and THP can be slightly outperformed for more than three memory coefficients. The full optimization of the WDFE parameters b_s and $I_{\max}$ is shown in Fig. 5.19 b) for a noise whitening filter with two memory taps. The optimum is found in the range $0.1 \leq b_s \leq 0.25$ and $0.2 \leq I_{\max} \leq 0.3$.

The simplified approach PDFE that avoids weighting of decisions can also be combined with a noise whitening filter and VE. The performance of this combination in dependence on the PDFE ratio r_c is shown in Fig. 5.20 for different numbers of post-filter memory coefficients. The results are based on 112 GBd PAM-4 data transmitted over 1 km on the setup in Tab. 5.1. If one memory tap is used, a ratio of $r_c = 0.2$ leads to the best performance. For two and three memory taps, $r_c = 0.25$ leads to the lowest BER. While some gain can be achieved by increasing the post-filter coefficient number from one to two, the third coefficient does not have a relevant impact on the optimal performance.

To evaluate the capabilities of PDFE, it needs to be compared to alternative DSP approaches, especially WDFE as a closely related contender. This comparison is shown in Fig. 5.21 for 112 GBd PAM-4 transmitted over 1 km. As previously observed for

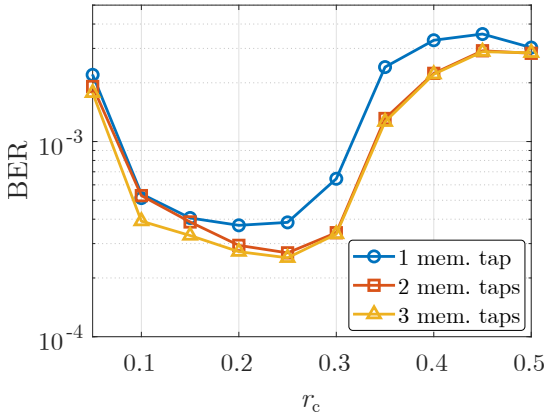

Figure 5.20: Optimization of the ratio r_c between hard decision and equalizer output in the PDFE feedback. The results are based on experimental data of 112 GBd PAM-4 transmission over 1 km.

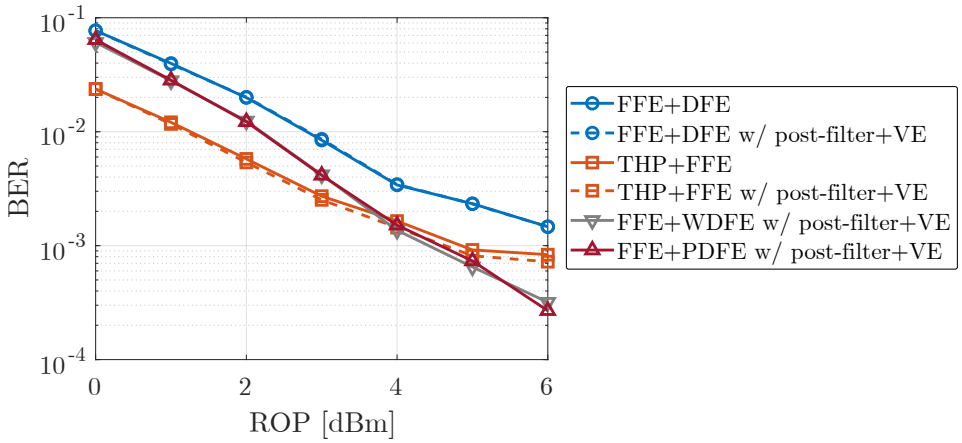

Figure 5.21: Performance of various DSP approaches as a function of the ROP for experimental 112 GBd PAM-4 data transmitted over 1 km. The combinations of WDFE and PDFE with noise whitening filter and VE are compared.

similar scenarios, THP outperforms DFE and the performance of both schemes cannot be improved by a consecutive noise whitening filter. The combination of FFE and WDFE followed by a post-filter lies between DFE and THP for ROPs between 0 dBm and 4 dBm. For higher ROPs a better performance than for THP is reached. In case WDFE is replaced by PDFE, an almost identical performance is obtained. Therefore, PDFE is the preferable solution as it requires fewer calculation and optimization steps.

Finally, the performance of the combination of FFE, two coefficient PDFE and noise whitening filtering with VE is evaluated on varying symbol rates for 2 km PAM-4 transmission. The results are depicted in Fig. 5.22. As a reference, the curves for DFE, WDFE and THP are given, as already shown in Fig. 5.18 b). Additionally, the option of making the FFE-PDFE structure target the DB response, adding a noise whitening

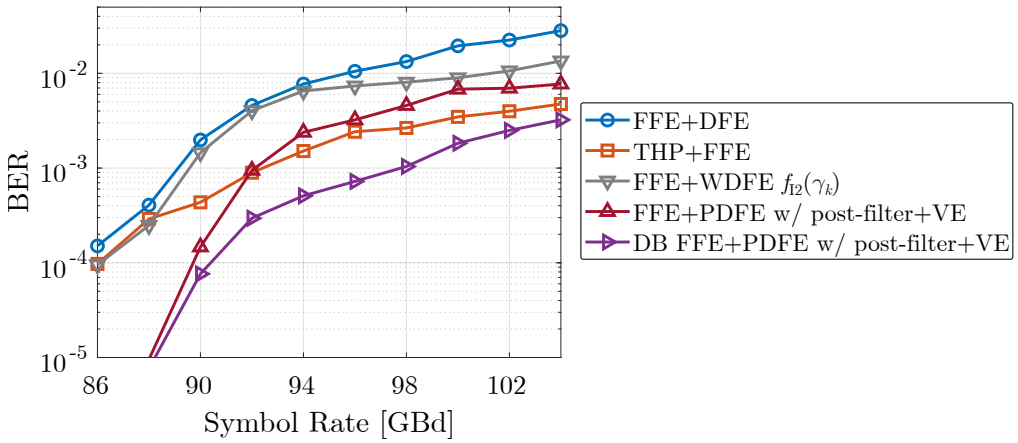

Figure 5.22: Performance of PDFE combined with a noise whitening filter and VE at varying symbol rates for 2 km PAM-4 transmission compared to conventional approaches. Additionally, PDFE targeting the DB response combined with a post-filter is shown.

filter and removing the combined DB and post-filter response by VE, as described in Sec. 3.2.5, is considered. For rates below 92 GBd, PDFE combined with a post-filter leads to a better performance than THP. For higher rates, the performance is worse but still an improvement compared to DFE and WDFE is visible. Using the DB response as a target is especially beneficial at high symbol rates. A clear improvement towards PDFE targeting the full response is realized. Even for the highest considered rates, this approach performs better than THP. This makes it an interesting alternative, as only receiver-side operations are performed and the feedback of channel information as required for THP is avoided. However, this good performance comes at the cost of high computational complexity.

5.1.8 Gerchberg-Saxton based Electronic Dispersion Compensation

For the investigations of GS EDC also scenarios outside the intra DCR and DCR campus ranges are considered. This is done because the effect of CD can be investigated more isolated from bandwidth limitations, if lower symbol rates and higher transmission distances are treated. The parameters of the components used for the simulations are chosen according to the experimental setup summarized in Tab. 5.5. Only the bandwidth of the MZM is increased to 50 GHz and an EDFA is used to cover the increased distance. The simulation results for 28 GBd PAM-4 transmitted over 40 km SSMF in C-band are shown in Fig. 5.23. First, the impact of GS EDC on the spectrum of the transmitted signal is depicted in Fig. 5.23 a). As an input, a signal shaped by an RRC filter with an ROF of $\beta_{\mathrm{ro}} = 1$ is chosen. GS EDC aims at a flattening of the signal spectrum in the regions between the spectral nulls induced by power fading. For the considered scenario, the first four nulls lie at the frequencies $\{9.6; 16.6; 21.5; 25.4\}$ GHz. At these exact frequencies,

Table 5.5: Parameters of the setup used for investigations on GS EDC. The systems block diagram is depicted in Fig. 5.1.

Component Type	Model Name	Parameters
AWG	Keysight M8199A	3-dB bandwidth: 55 GHz Sampling Rate: 256 GS/s ENOB: $\approx$ 5.5 bits
DA	SHF 810	3-dB bandwidth: >40 GHz Gain: 30 dB
MZM	Oclaro SD-40	3-dB bandwidth: 32 GHz V_π: $\approx$ 5 V
PD	Fraunhofer HHI Single Detector	3-dB bandwidth: >70 GHz
DSO	Keysight UXR1104A	3-dB bandwidth: 80 GHz Sampling Rate: 256 GS/s ENOB: $\approx$ 5 bits

notches are visible in the spectrum after GS EDC, as an amplification of these frequencies will not improve the performance due to the complete cancellation after reception. The frequencies next to the notches are amplified the most, as these experience a strong attenuation by power fading. The frequencies in the middle between two notches, on the other hand, are not amplified, as these components are not impacted by power fading. The optimization of the digital ER of the input signal is shown in Fig. 5.23 b). For this, the bias point is chosen to be at the quadrature point and the DAC output voltage range is fixed to $0.6V_\pi$. The lowest BER is reached at 3 dB, so this value is used for the following investigations.

Finally, the performance of GS EDC is evaluated in dependence on the MZM input voltage range for different receiver FFEs (5.23 c)). As a baseline, the performance without application of GS EDC is shown. It is generally visible that the voltage range at the input of the modulator has a significant impact on the performance for all scenarios. The optimum is shifted towards higher ranges, if GS EDC is applied. For FFE with $N_1 = 80$ coefficients operating at 2 SpS, the optimal MZM input range lies at $0.3V_\pi$ for the case without GS EDC and at $0.6V_\pi$, if it is applied. The improvement of the optimal performance by GS EDC is limited. For FFE with only $N_1 = 20$ coefficients a clear performance penalty compared to the higher coefficient number is observed. The optimum MZM input voltage is similar, but the gain by GS EDC is more significant than for the previous case. If FFE operating at 1 SpS is applied, the performance is poor. GS EDC improves the performance by more than a factor of two but does still not reach a BER below 10^{-2}. These results can be explained by the usability of redundant frequencies in oversampled signals to recover spectral nulls, which is utilized in SFPC

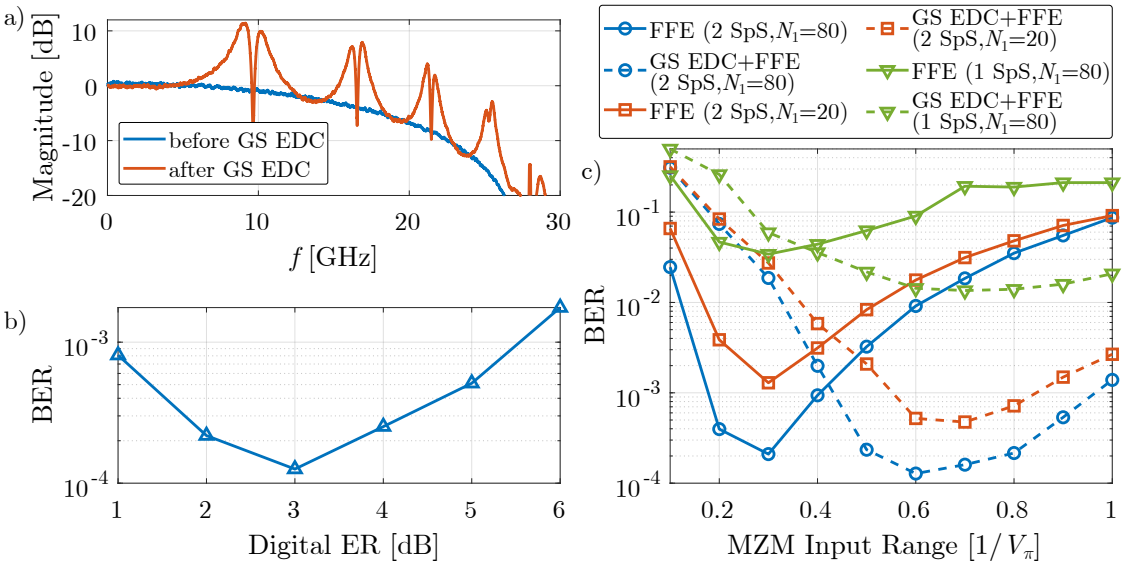

Figure 5.23: Simulative investigations on GS EDC. The results are based on 28 GBd PAM-4 transmitted over 40 km. a) shows the impact on the transmitted signal spectrum, b) the optimization of the digital ER and c) the performance in dependence on the MZM input voltage range.

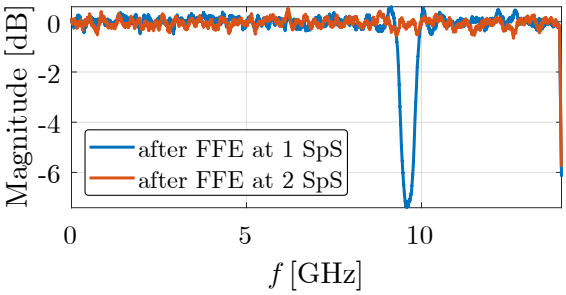

Figure 5.24: Spectra after FFE for 28 GBd PAM-4 transmitted over 40 km. GS EDC was applied on the signal in the transmitter DSP.

(cf. Sec. 3.3.2). Since the transmitted signal is oversampled multiple times and a RRC ROF of $\beta_{\mathrm{ro}} = 1$ is used, all frequency components are contained twice in the transmitted signal. If the equalizer in the receiver DSP operates at 2 SpS, this redundancy can be utilized to overcome the spectral nulls in the received signal. This effect is exemplary shown in Fig. 5.24 for an MZM input range of $0.6V_\pi$ and $N_1 = 80$ FFE coefficients. After equalization at 1 SpS, a notch at the position of the first spectral null is clearly visible. If the equalizer operates at 2 SpS, this notch can be completely removed. Therefore, it can be concluded that the utilization of redundant frequencies has a significantly stronger impact on the performance than GS EDC in the investigated scenario.

Experimental investigations on GS EDC are done based on a setup with parameters according to Tab. 5.5. The results based on FFE with memory lengths of $N_1 = 200$,

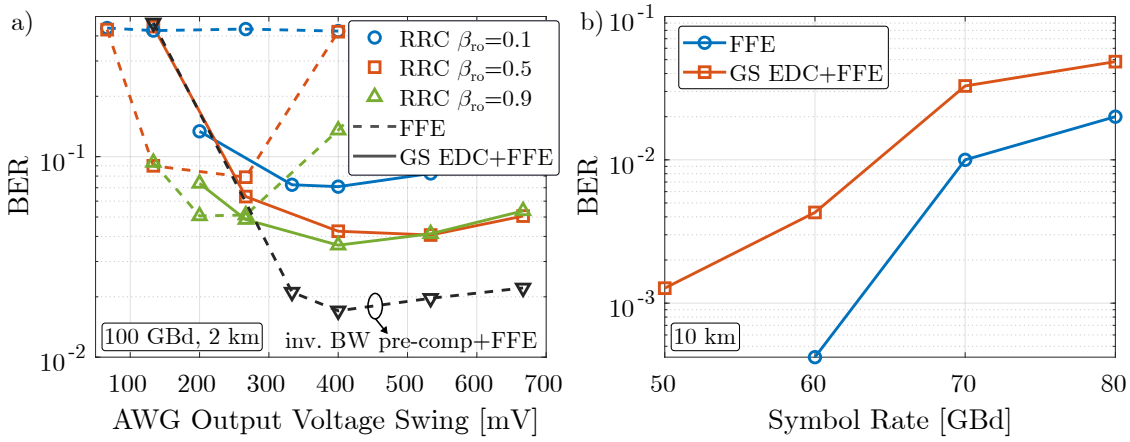

Figure 5.25: Experimental investigations on GS EDC. a) shows the BER in dependence on the AWG output voltage swing for 2 km and b) shows results for 10 km and different symbol rates.

$N_2 = 9$ and $N_3 = 9$ are visualized in Fig. 5.25. Figure 5.25 a) shows the impact of the AWG output voltage swing on the performance of a 100 GBd PAM-4 transmission over 2 km in C-band. Results with and without the application of GS EDC are shown. For both cases, higher ROFs lead to improved performance, but the impact of the ROF is less significant, if GS EDC is applied. For a low ROF of $\beta_{ro} = 0.1$, the transmission without EDC fails (constant BER of 0.5) and GS EDC can improve the performance significantly. However, for a high ROF of $\beta_{ro} = 0.9$, the performance gain achieved by GS EDC is limited. As already seen in the simulations, a higher AWG output voltage is necessary, if GS EDC is applied. Additionally, a curve is shown, where conventional inverse bandwidth pre-compensation is applied. For an ROF of $\beta_{ro} = 0.9$, a better performance than for GS EDC can be reached. Figure 5.25 b) shows the BER as a function of the symbol rate for 10 km C-band PAM-4 transmission. For the rates between 50 GBd and 80 GBd, the results for the case of applying only FFE are even better than for the case that GS EDC is added. The reason for this is probably the strong amplifications of certain frequency components in the transmitted signal due to GS EDC. This causes a relative attenuation of other frequency components and increases the PAPR of the signal, which in turn leads to higher quantization noise. The adaptation of the signal to the dispersive channel does not seem to help significantly. The relatively long receiver equalizer can flatten the signal spectrum, except for the spectral zeros, which are not improved by GS EDC anyway. All in all, it seems difficult to find convincing scenarios for the application of this scheme. Especially, because the iterative procedure (cf. Sec. 3.3.1) is computationally complex due to the two FFTs and inverse fast Fourier transforms (IFFTs) as well as complex multiplications per iteration.

Table 5.6: Pre-compensation options considered to evaluate SFPC.

Option	Pre-compensation approach
1	none
2	inverse bandwidth
3	SFPC
4	combined (SFPC+inverse bandwidth)

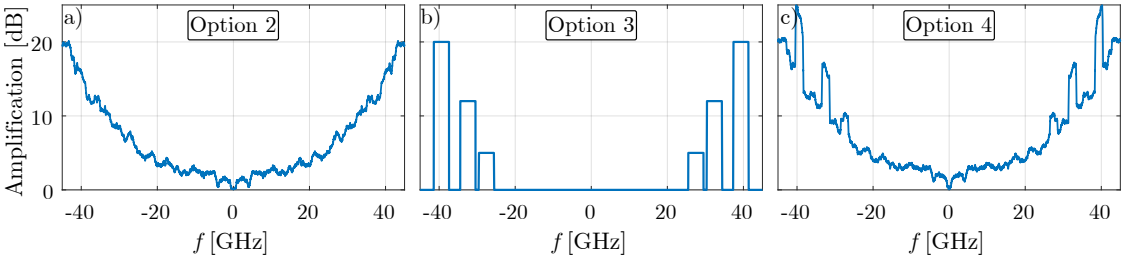

Figure 5.26: Exemplary spectra of the different pre-compensation options optimized for 50 GBd transmission over 35 km SSMF in C-band.

5.1.9 Selected Frequency Pre-Compensation

Similar to the investigations on GS EDC, part of the results on SFPC are based on transmission distances outside the FR and LR scenarios, to view the effect of CD more isolated from bandwidth limitations. The parameters of the setup used for experiments are summarized in Tab. 5.3. Due to the relatively long transmission distance of 35 km used for these investigations, an EDFA is deployed before the PD. This amplifier delivers a constant power of 7 dBm to the receiver. The EDFA is treated like a part of the receiver in the following, so that ROP values refer to the input power into the amplifier. The major part of the experimental results shown for this approach has been published in [115].

To evaluate the performance of SFPC, four options for pre-compensation need to be considered. Those options are summarized in Tab. 5.6 and will be referred to as option 1, 2, 3 and 4 in the following. Option 1 gives the baseline scenario of using no pre-compensation at all. Option 2 is the usage of inverse bandwidth pre-compensation (cf. Sec. 3.1.4). The corresponding frequency response is obtained by transmitting a multi-tone sequence with 256 sub-carriers and comparing the transmitted and received sequences at each sub-carrier. The transfer function for the given experimental setup is shown in Fig. 5.26 a). Option 3 corresponds to the application of only SFPC. For the 35 km C-band transmission, the first three spectral nulls lie at the frequencies $f_{\mathrm{null},1} = 10.61$ GHz, $f_{\mathrm{null},2} = 17.57$ GHz and $f_{\mathrm{null},3} = 22.48$ GHz. According to Eq. 3.43, the redundant frequencies $f_{\mathrm{r},1} = 39.39$ GHz, $f_{\mathrm{r},2} = 32.43$ GHz and $f_{\mathrm{r},3} = 27.52$ GHz can be used to recover these in case of a 50 GBd signal. Figure 5.26 b) shows an example of a pre-compensation frequency response

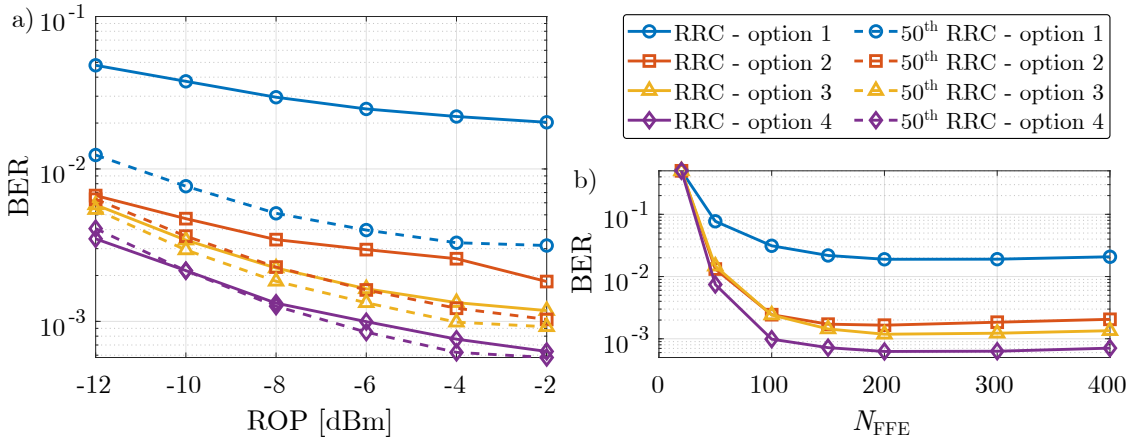

Figure 5.27: Experimental investigations on SFPC for 50 GBd PAM-4 transmission over 35 km. a) shows the BER as a function of the ROP into the EDFA and b) shows the impact of the number of linear FFE coefficients.

resulting from this information. The frequencies $f_{\mathrm{r},1}$, $f_{\mathrm{r},2}$ and $f_{\mathrm{r},3}$ as well as a range of ± 2 GHz around these are amplified by a constant value. The amount of amplification is optimized individually and is dependent on the bandwidth limitations these frequencies experience, the power fading effect and the pulse shape of the signal. Strong amplifications of these outer frequencies effectively attenuate the signal inside the Nyquist frequency range and enhance the PAPR, so this trade-off needs to be optimized. For the following results, the optimization is done by sweeping through possible values and evaluating these by the resulting BER. Finally, option 4 combines the approaches of options 2 and 3. The inverse bandwidth pre-compensation is used as a basis and the redundant frequencies for the recovery of the spectral nulls are additionally enhanced. Several parameters, like the maximum amplification by the inverse bandwidth pre-compensation, the amplification of the redundant frequencies as well as the width of the amplification windows, need to be optimized. An example of a resulting transfer function is given in Fig. 5.26 c). To limit the PAPR at the DAC input to a reasonable level, clipping is applied after pre-compensation. A PAPR of 10 dB has shown to provide good performance.

Fig. 5.27 a) shows experimental results for the BER as a function of the ROP for 50 GBd PAM-4 transmission over 35 km. For the pulse shape next to conventional RRC a more rectangular shape, namely 50$^{\mathrm{th}}$ RRC, is considered to limit the attenuation of the high-frequency components. VNLE with memory lengths of $N_1 = 200$, $N_2 = 11$ and $N_3 = 11$ is used in the receiver DSP. All four pre-compensation options are compared for the two different pulse shapes. For the RRC shape, option 1 results in poor performance. Adding inverse bandwidth pre-compensation (option 2) improves the performance significantly, but option 3 based on SFPC outperforms this option. This shows that a proper pre-

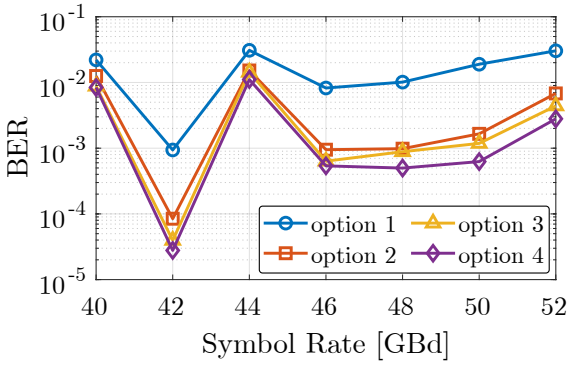

Figure 5.28: Performance for different symbol rates considering PAM-4 transmission over 35 km and an RRC pulse shape at a constant ROP of -2 dBm into the EDFA.

compensation of the redundant frequencies is more relevant than pre-compensation of the whole signal frequency range. Option 4 leads to the clearly best performance. The 50^{th} RRC shape results in a much better performance for option 1, because the redundant frequencies do not experience a significant attenuation by the pulse shape. Option 2 further improves the performance to the level of option 3 with RRC shape. Option 3 additionally improves the performance slightly and option 4 again leads to the best overall performance. Independent from the pulse shape, it seems favorable to combine inverse bandwidth pre-compensation with SFPC to improve the performance. Figure 5.27 b) shows the performance of the 50 GBd PAM-4 transmission over 35 km in dependence on the number of linear FFE coefficients. For all pre-compensation options, the performance improves up to $N_{\text{FFE}} = 200$ coefficients. Options 2 and 3 perform very similarly up to $N_{\text{FFE}} = 150$ coefficients. In case the receiver FFE uses $N_{\text{FFE}} = 200$ coefficients or more, option 3 leads to better performance. The reason for this is given by the fact that the signal in the Nyquist frequency range ($\pm f_{\text{sym}}/2$) is not pre-compensated for option 3 and FFE has to overcome the bandwidth limitations in that range, which requires many coefficients. Option 4 shows the best performance for all equalizer lengths.

As described in Sec. 3.3.2, a drawback of the SFPC approach is the fact that certain combinations of accumulated CD, carrier wavelength and symbol rate lead to poor performance. This is the case because in such unfavorable scenarios one or more of the redundant frequencies lie very close to a spectral null. Under these circumstances, the information is not only lost at the initial spectral null but also at the backup frequency so that the information cannot be recovered. Results for the BER over the symbol rate for PAM-4 transmission over 35 km using an RRC pulse shape are shown in Fig. 5.28. Tab. 5.7 shows the frequency gap of the redundant frequencies that are necessary for the reconstruction of the spectral nulls to their neighboring spectral nulls for each shown

Table 5.7: Frequency gap between redundant frequencies and spectral nulls for different rates and 35 km C-band transmission.

Symbol Rate [GBd]	Minimum distance of the redundant frequency to the next spectral null [GHz]		
	$f_{r,1}$	$f_{r,2}$	$f_{r,3}$
40	0.57	0.05	-
42	1.43	1.95	-
44	0.31	0.07	-
46	0.54	1.53	1.04
48	1.21	0.47	0.98
50	0.79	0.65	1.02
52	0.31	1.35	0.44

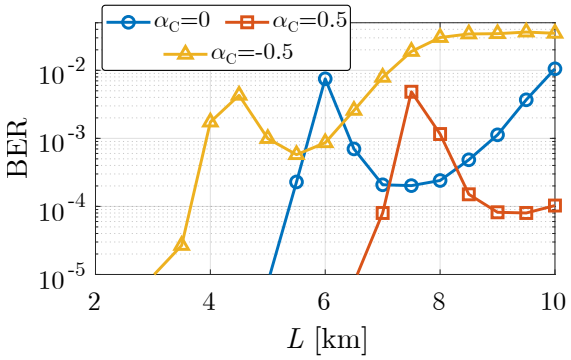

Figure 5.29: Simulations on 112 GBd PAM-4 transmission over varying fiber lengths L, assuming different chirp parameters α_C.

symbol rate. Cases, in which the frequency is experiencing a relevant attenuation by power fading are marked in orange and the cases, in which the distance to a spectral null is so small that these frequencies cannot be utilized are marked in red. While 42 GBd transmission results in a good performance for all pre-compensation options, 44 GBd leads to poor results. The explanation can be found in Tab. 5.7: for 42 GBd, the redundant frequencies are not significantly affected by power fading and can be utilized, while for 44 GBd especially $f_{r,2}$ is strongly affected by power fading and cannot be utilized to reconstruct the corresponding spectral null. Comparing the different pre-compensation options, the order is unchanged to the 50 GBd results for all rates. Option 4 outperforms all the other options as expected.

Evaluation of the Analytical Description

The conditions under which spectral nulls cannot be compensated are analytically described in Sec. 3.3.2. This description is evaluated in simulations, which are based on the setup in Tab. 5.5, where only the modulator bandwidth is increased to 50 GHz. For

the evaluation, the whole LR scenario is considered: 112 GBd PAM-4 is transmitted over 2 km to 10 km SSMF in O-band. As a carrier wavelength, the worst-case scenario of a CWDM transmission with four carriers, i.e. $\lambda = 1270\,\text{nm}$ with a dispersion parameter of $D = -5\,\text{ps/nm/km}$, is assumed. As SFPC does not have an impact on the positions of the spectral nulls, it is not applied for these investigations for simplicity. The performance for transmission over varying fiber lengths is shown in Fig. 5.29. If no chirp is induced during modulation, a fiber length of 6 km leads to poor performance, because the spectral null is located directly at the edge of the signal spectrum and according to that, this frequency would also be required for reconstruction. A calculation of this worst-case scenario based on Eq. 3.45 results in a length of $L = 5.934\,\text{km}$, which matches the simulation results. Considering the condition in Eq. 3.47 and a minimum attenuation of $a_{\text{min}} = 10\,\text{dB}$, an interval of $5.934\,\text{km} \leq L \leq 6.526\,\text{km}$ results. Looking at the upper limit, this matches the simulation results, as a distance of 6.5 km still leads to a relatively high BER. However, the lower limit does not seem to match. This is based on the fact that the condition only considers scenarios in which a spectral null is inside the signal spectrum. For distances below 5.934 km this is not the case, however, the outer signal frequencies can already be significantly attenuated by power fading leading to degraded performance. When chirp is added, the positions of the spectral nulls change. Considering chirp parameters of $\alpha_{\text{C}} = 0.5$ and $\alpha_{\text{C}} = -0.5$ and using Eq. 2.19 as a basis for the calculation of non-compensable lengths, values of $L = \{4.181; 9.166\}\,\text{km}$ for $\alpha_{\text{C}} = -0.5$ and $L = 7.682\,\text{km}$ for $\alpha_{\text{C}} = 0.5$ result. A comparison with the simulations in Fig. 5.29 shows a good match. Therefore, it can be concluded that the analytical description of the combinations of accumulated CD, wavelength and symbol rate leading to non-compensable spectral nulls is appropriate. Additionally, it is observed that any distance between 2 km and 10 km can be covered with a BER below 10^{-3} if different chirp parameters are available.

EML for Chirp Variation

For a more realistic simulation, an EML model is added to the simulation setup. The characteristics of the model are shown in Fig. 5.30. The power characteristic of the EML function was obtained in lab measurements on an actual component (CIG ETV800GXLMD001). The corresponding field characteristic is assumed to be the square root of the power characteristic. The relationship between the chirp parameter and input voltage was taken from [120]. According to these characteristics, the chirp parameter can be significantly changed by varying the bias voltage. However, this also significantly impacts the linearity of the EML function and the extinction ratio. To evaluate the impact of these characteristics, simulations for different bias voltages u_{bias} are shown

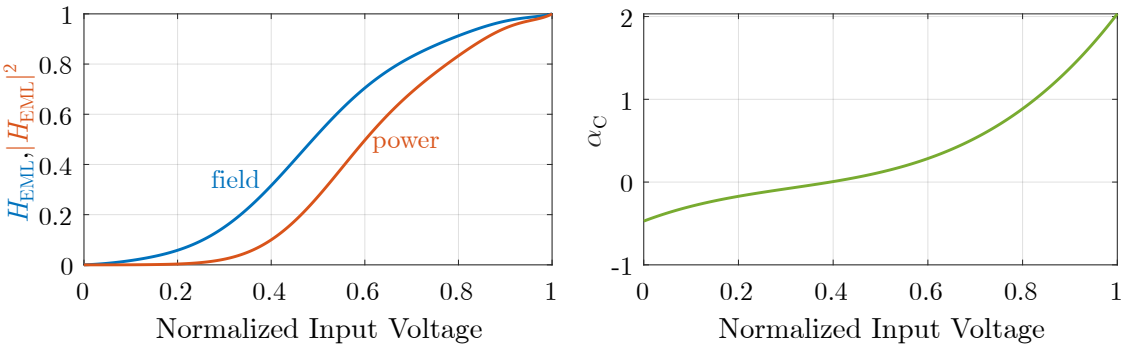

Figure 5.30: Characteristics of the EML model used for simulations.

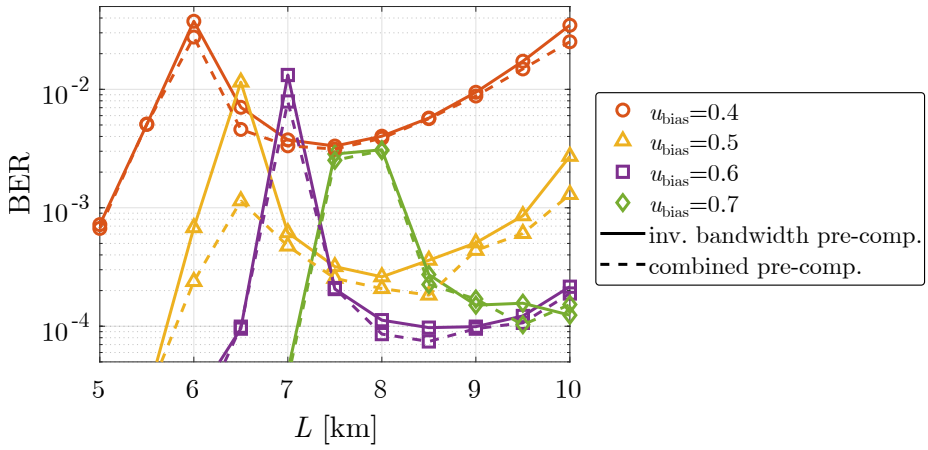

Figure 5.31: Simulation performance for 112 GBd PAM-4 over varying transmission distances using an EML model and different bias voltages.

in Fig. 5.31. 112 GBd PAM-4 shaped with a 50$^{\mathrm{th}}$ RRC is transmitted over distances between 5 km and 10 km and conventional inverse bandwidth pre-compensation as well as the combination with SFPC are considered. As carrier wavelength 1270 nm is used and the setup parameters are set as in the previous part, apart from an increased AWG bandwidth of 55 GHz for these investigations. It is observed that the non-compensable points shift towards higher fiber lengths with growing bias voltage. This can be explained by the linewidth enhancement factor that grows with higher input voltage. The bias voltage of $u_{\mathrm{bias}} = 0.4$ results in poor performance because it is in the nonlinear region of the EML power characteristic. However, by varying the bias voltage, all transmission distances in the considered range can be covered with a BER below 10^{-3}. Apparently varying the EML bias voltage is a feasible solution to avoid combinations of accumulated CD, wavelength and symbol rate that cannot be covered otherwise. However, the gain by adding SFPC on top of inverse bandwidth pre-compensation is very limited for this scenario. This is caused by the relatively high symbol rate and the resulting strong attenuation of frequencies outside the signal range by bandwidth limitations. In such a

Table 5.8: Parameters of the O-band setup. The systems block diagram is depicted in Fig. 5.1.

Component Type	Model Name	Parameters
AWG	Keysight M8196A	3-dB bandwidth: 32 GHz Sampling Rate: 92 GS/s ENOB: ≈ 5.5 bits
DA	SHF 804EA	3-dB bandwidth: >45 GHz Gain: 20 dB
Bias Tee	SHF BT 65 B	3-dB bandwidth: >65 GHz
EML	CIG ETV800GXLMD001	3-dB bandwidth: 55 GHz λ=1308 nm
SOA+ Evaluation Board	Aeon SAOM Aeon SET-II	Peak Gain: 20 dB Noise Figure: 7 dB
PD	Fraunhofer HHI Single Detector	3-dB bandwidth: >70 GHz
DSO	Keysight DSOZ634A	3-dB bandwidth: 63 GHz Sampling Rate: 160 GS/s ENOB: ≈ 5 bits

scenario, inverse bandwidth pre-compensation can improve the performance significantly by applying strong amplification on high frequencies. Adding even more amplification by SFPC is critical due to the limited DAC resolution and linear modulator range, so no significant improvement can be achieved.

5.1.10 O-band Transmission

The vast majority of experiments shown in this work are done in C-band at a carrier wavelength of 1550 nm. This is founded on the better availability of C-band components in the labs in which measurements were done. Additionally, dispersion effects can be investigated easier at this wavelength. However, transmission in the O-band around the zero-dispersion wavelength for SSMF of 1310 nm is the preferred option for short-reach IM/DD systems. The increased fiber loss compared to the C-band is not critical for short transmission distances, while the notable reduction of CD can have a significant impact on the performance. O-band experiments are shown based on a setup with parameters summarized in Tab. 5.8. For the O/E conversion an EML transmitting at 1308 nm is applied. As this device has no bias voltage input, an additional bias tee is used to make the input signal utilize the desired region of the characteristic (shown in Fig. 2.3 b)). For the operation of the EML an external thermoelectric cooler (TEC) controller and a laser current source are required. Before detection with a PD, an SOA is used to provide a constant power of 7 dBm. This device is mounted on an evaluation board that ensures temperature control and current supply.

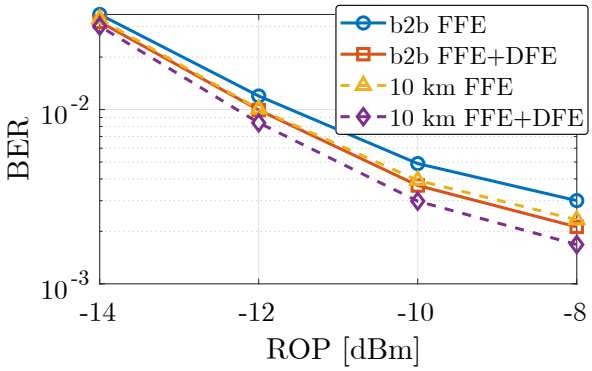

Figure 5.32: Experimental results for 92 GBd PAM-4 transmission on O-band.

The experimental results for 92 GBd PAM-4 transmission in a back-to-back configuration and over 10 km SSMF are shown in Fig. 5.32. For the equalization in the receiver DSP, two options were considered: VNLE with memory lengths of $N_1 = 200$, $N_2 = 11$ and $N_3 = 11$ with and without $N_{\mathrm{DFE}} = 2$ coefficient DFE. The ROP refers to the input power into the SOA. It is visible that the performance for transmission over 10 km is even better than for the back-to-back configuration. The reason for this is that the modulator introduces a certain frequency chirp to the signal and the small amount of CD due to the O-band transmission limits the penalty by the chirp. DFE brings a relatively small gain for both transmission distances. Note that the dispersion penalty in O-band can be considerably higher than in the shown results if WDM with carrier wavelengths deviating further from the zero-dispersion wavelength is applied.

5.1.11 Comparison of DSP Approaches

The performance penalty by CD gets more and more critical with growing data rates. Therefore, the tolerance regarding this impairment is interesting to evaluate DSP approaches. The tolerance of different schemes is shown in Fig. 5.33 for 112 GBd PAM-4 simulations. For the simulations, the parameters in Tab. 5.1 are used, but the transmitter bandwidth constraints are relaxed to a 3-dB bandwidth of 60 GHz per component. This way, the simulations are more focussed on the impact of CD. To keep the simulations simple, only a single noise source with a noise figure of $F_{\mathrm{N}} = 5$ dB placed before the PD is assumed. Six DSP approaches are considered for the comparison, namely FFE only, FFE with DFE, THP combined with FFE, FFE with post-filter and VE, DB FFE with VE and finally DB FFE-PDFE with a noise whitening post-filter and VE. To evaluate the tolerance of the different approaches, the required OSNR to reach a BER of $2 \cdot 10^{-3}$ is shown over accumulated CD values in the range [-35;35] ps/nm. Applying only FFE in the receiver DSP results in the lowest CD tolerance. An OSNR of ≈ 25 dB is required, if no CD is induced during transmission and ± 15 ps/nm already lead to a penalty of nearly

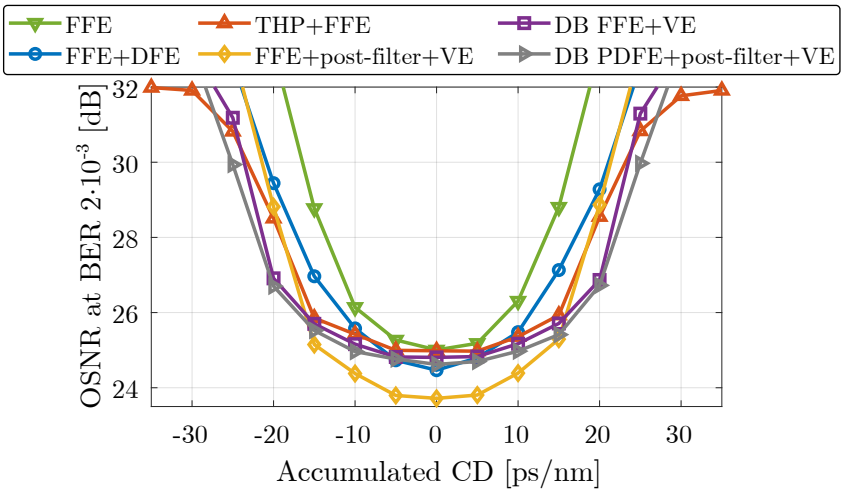

Figure 5.33: Simulative results for the required OSNR to reach a BER of $2 \cdot 10^{-3}$ for different amounts of accumulated CD at 112 GBd PAM-4.

4 dB. Combining FFE with DFE improves the CD tolerance. While the gain over only FFE lies around 0.5 dB at zero dispersion, it is approximately 1.5 dB at ±15 ps/nm. THP shows even better capabilities of compensating CD induced power fading. The required OSNR is similar to FFE in the case without dispersion which can be explained by the relaxed bandwidth limitations. However, the penalty induced by ±15 ps/nm is only 1 dB. Especially for high values of >25 ps/nm, THP shows the lowest OSNR penalty of all considered DSP approaches. Combining FFE with a subsequent post-filter with 1 memory coefficient and VE requires the lowest OSNR for the case without CD. The CD tolerance is increased compared to only FFE but especially at high CD values, other schemes show a better performance. The approaches based on the DB target for the receiver equalizer show good CD tolerance. The relative performance compared to the other approaches in the case without CD is rather poor, since the high available bandwidth results in a receiver spectrum not ideally matching the DB response. Both schemes show a similar penalty up to ±20 ps/nm. Only at a high accumulated dispersion of ±25 ps/nm, the scheme including PDFE and noise whitening filtering shows a penalty smaller than 1 dB compared to the simpler DB FFE.

The same setup as for the previous results is used to investigate the impact of chirp on the CD tolerance and to compare PAM-4, PAM-6 and PAM-8. These results are shown in Fig. 5.34. To keep the results clear, only FFE is considered for DSP. Linewidth enhancement factors of $\alpha_C = -0.5$ and $\alpha_C = 0.5$ are considered to see how the tolerance could be increased by a variable modulator chirp. The curves for 112 GBd PAM-4 are shifted by approximately ±10 ps/nm compared to the chirp less case. This means the dispersion tolerance can be increased in this range, if the modulator chirp is variable

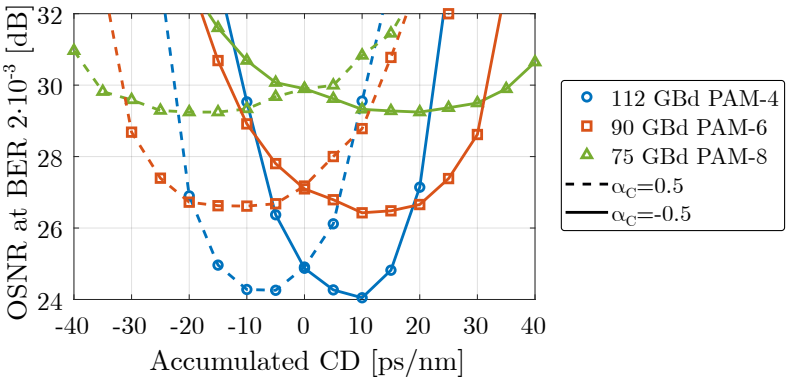

Figure 5.34: Simulative results for the required OSNR to reach a BER of $2 \cdot 10^{-3}$ for different amounts of accumulated CD comparing PAM-4, PAM-6 and PAM-8. The impact of chirp is shown for two exemplary values of the chirp parameter α_C.

in the range $\alpha_C = \pm 0.5$. The curves for PAM-6 are flatter than for PAM-4 due to the decreased symbol rate. A change in accumulated CD by ± 15 ps/nm only results in an OSNR penalty of around 1 dB. However, due to the increased number of symbol levels, a higher OSNR is required to reach a BER of $2 \cdot 10^{-3}$ in case of no CD. Therefore, the required OSNR can only be decreased compared to PAM-4, if significant amounts of CD are introduced in the channel. This trend is continued for 75 GBd PAM-8. While a comparatively high OSNR of more than 29 dB is required in the best case, the penalty by CD is very low. Even at the highest considered accumulated CD values, only a penalty of 2 dB is observed. In conclusion, the expectations are met by these results: low order PAM formats perform well in channels with less significant lowpass characteristics, while higher order formats show a good tolerance towards CD induced power fading.

To get a comprehensive overview of the relative performance of various DSP schemes under different conditions, broad experimental measurements were performed. These include PAM-4, PAM-6 and PAM-8 transmitted over a back-to-back configuration, 1 km and 2 km SSMF at a carrier wavelength of 1550 nm. Bit rates in the range of 180 Gb/s to 300 Gb/s are considered. The corresponding results have already been published in [106]. For the intra-DCR FR application a fixed net bit rate of 200 Gb/s is of interest. However, the performance at this rate strongly depends on the exact components used for the measurements. While formats with a lower order potentially perform better in systems with less strict bandwidth limitations, explained by their higher noise and nonlinearity tolerance, higher order formats can be advantageous in systems with a strong lowpass characteristic. As the experimental setup has fixed parameters, a variation of the symbol rate is used as an emulation of varying component bandwidths. A lower bit rate at constant bandwidth limitations behaves similarly to an increased bandwidth at a constant

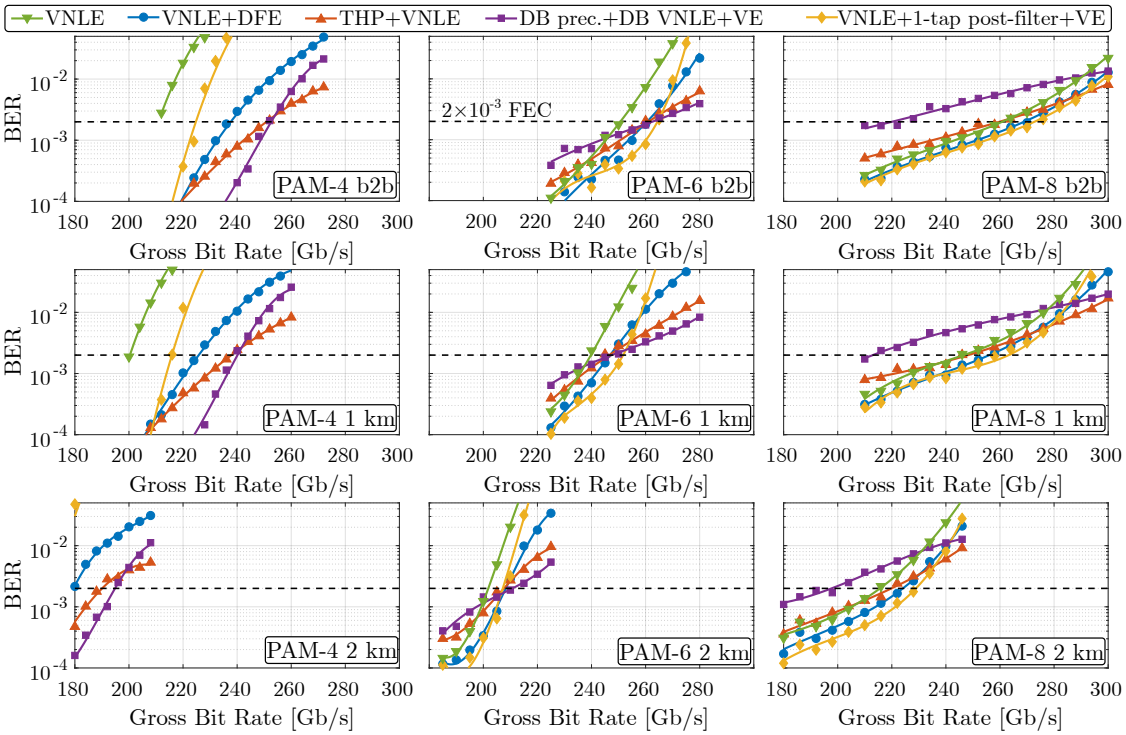

Figure 5.35: Experimental comparison of PAM-4, PAM-6 and PAM-8 applying different DSP approaches at bit rates ranging between 180 Gb/s and 300 Gb/s. Transmission over an optical back-to-back configuration, 1 km and 2 km SSMF in C-band are considered.

bit rate and vice versa. Note that the impact of the penalty by CD induced power fading also increases for growing symbol rates so that the approximation is only fair for the back-to-back configuration.

The experimental results based on the setup summarized in Tab. 5.1 are shown in Fig. 5.35. Five different DSP approaches that supplement the basic DSP stack (cf. Fig. 3.1) are considered: VNLE, VNLE combined with DFE, THP and VNLE, DB pre-coding with DB VNLE and VE as well as VNLE followed by a noise whitening filter with one memory coefficient and VE. The parameters for these approaches are summarized in Tab. 5.9. The number of FFE coefficients is chosen sufficiently high so that the impact of the additional DSP approaches can be compared irrespective of this parameter. A FEC limit of $2 \cdot 10^{-3}$ is assumed (cf. Sec. 2.5).

Considering PAM-4 transmission in a back-to-back configuration, the best performance for rates below 250 Gb/s is obtained by the DB scheme. If the rate is further increased, THP shows a better performance. At 220 Gb/s DFE and the post-filter approach perform similarly to THP. However, for growing rates DFE is clearly outperformed by THP and in turn shows a significantly better performance than the noise whitening filter, which

Table 5.9: Parameters of the DSP schemes that are experimentally compared.

DSP approach	Parameters
VNLE	$N_1 = 200$, $N_2 = 11$, $N_3 = 11$
DFE, THP	2 coefficients
Noise whitening filter	1 memory coefficient

results in a BER of $5 \cdot 10^{-2}$ at a rate of 236 Gb/s. The worst performance for all rates is obtained by VNLE without additional DSP. For this approach, the FEC limit is not reached for rates of 212 Gb/s and above. It needs to be noted that in case of PAM-4 rates above 240 Gb/s exceed the AWG sampling rate of 120 GS/s. A Kaiser window anti-aliasing filter is used during the re-sampling process to enable these rates. Increasing the transmission distance to 1 km provides the expected performance degradation for all schemes due to CD. The relative performance of the considered DSP approaches, however, stays similar. DB pre-coding together with DB equalization and VE performs best below the FEC limit. At rates above 240 Gb/s THP is the best choice. A transmission distance of 2 km results in more severe power fading and the reachable rates are significantly reduced. The DB approach crosses the FEC limit at 195 Gb/s and besides THP, no other scheme enables data rates above 180 Gb/s.

The relative performance of the DSP approaches changes clearly for PAM-6. While the DB approach is the best choice for PAM-4 transmission below the FEC limit for the considered rates, it performs worse than the other advanced DSP schemes for rates up to 260 Gb/s in PAM-6 back-to-back measurements. This can be explained by the fact that the received spectrum after PAM-6 transmission does not match the DB response due to the lower symbol rates compared to PAM-4. The corresponding spectra for a 224/225 Gb/s together with the target responses are shown in Fig. 5.2 for PAM-4 and PAM-6. The mismatch between the received PAM-6 spectrum and the DB response shrinks with growing rates, which explains the relatively good performance of the DB scheme for the highest considered PAM-6 rates. For rates below 260 Gb/s DFE and the noise whitening filter approach show the best performance. While the gain by the post-filter is low compared to only applying VNLE for rates up to 230 Gb/s, a clear gain is achieved for higher rates. This is again explained by the increased noise enhancement at higher rates (cf. Sec. 5.1.6). THP is the second best approach for rates above 265 Gb/s but is no interesting choice for lower rates. Especially for rates below 235 Gb/s THP even decreases the performance compared to VNLE without additional schemes. For 1 km transmission a similar relative performance of the considered DSP approaches as in the back-to-back measurements is visible. The post-filter scheme is the best approach up to

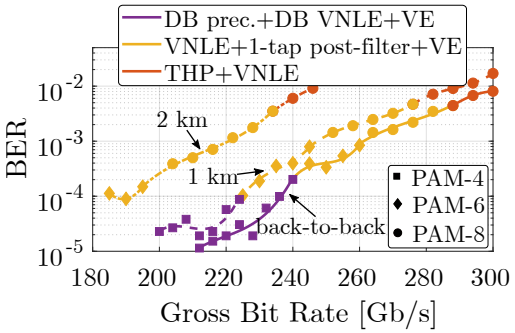

Figure 5.36: Best obtained results in terms of modulation format and DSP steps for the considered bit rates and distances.

250 Gb/s and the DB scheme for higher rates. For 2 km the performance of all schemes is degraded significantly and no rates higher than 210 Gb/s are realized below the FEC limit.

The results of the PAM-8 measurements show a very similar performance of DFE and the post-filter approach. Both are superior to the alternative schemes in the considered bit rate range. The gain over VNLE without additional steps, however, is small. The application of THP leads to a performance penalty at the lowest rates and around 260 Gb/s the penalty by applying THP is zero, before a small gain is observed for higher rates. The DB scheme performs worse than the other contenders, which is again explained by the decreased symbol rate for PAM-8. The relative performance is similar for 1 km and 2 km transmission. The gain of the post-filter approach compared to DFE gets slightly higher for increased rates and THP performs best for the highest considered rates.

The comparison of the results between PAM-4, PAM-6 and PAM-8 shows a general trend: A steep ascend of the BER for growing rates is observed for PAM-4, while the curves get flatter with increasing modulation order. For the lower considered bit rates, PAM-4 offers the capability of reaching very low BERs, while a good performance at higher rates and distances can be reached with PAM-8. PAM-6 seems to be a good choice for the intermediate region in terms of bit rate and distance. Also, some general trends regarding the different DSP schemes are observed: the noise whitening filter results in good performance under favorable conditions, i.e. low rates and distances, while the relative performance under stronger restrictions is poor. The explanation lies in the convergence of the equalizer. As long as VNLE converges well, the post-filter can improve the performance, while it cannot work properly after a poorly converged equalizer. The other schemes have a direct impact on the VNLE convergence, which is advantageous under strong restrictions.

The best solutions concerning modulation format and DSP approach for each bit rate at the considered transmission distances are depicted in Fig. 5.36. For the back-to-back

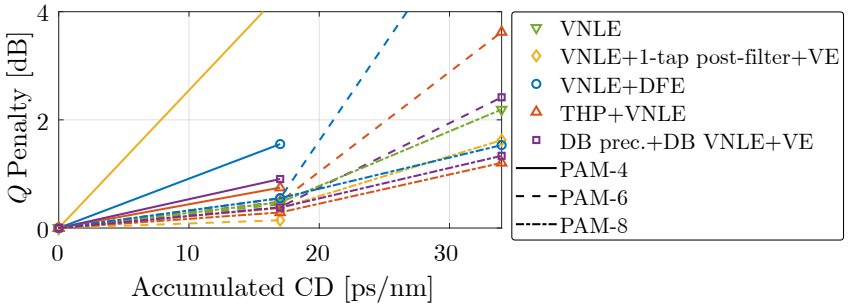

Figure 5.37: Q factor penalty for the different modulation formats and DSP approaches in dependence on the accumulated CD at 224/225 Gb/s.

case, the lowest BER for rates up to 240 Gb/s is reached using PAM-4 combined with DB pre-coding, DB FFE and VE. The rates between 240 Gb/s and 260 Gb/s are covered best by PAM-6 with the post-filter approach and for the highest rates, PAM-8 leads to the best results. THP is the best DSP scheme for rates beyond 280 Gb/s. The optimal curve for 1 km transmission only shows a small penalty over the back-to-back scenario. The same combination of modulation format and DSP approaches appear in the curve. PAM-4 with the DB scheme is best up to 225 Gb/s, PAM-6 with post-filter up to 245 Gb/s, PAM-8 with post-filter up to 280 Gb/s and finally PAM-8 with THP yields the best results. Increasing the transmission distance to 2 km leads to a clearly decreased performance, as the first spectral null by power fading reaches positions inside or close to the signal spectra. PAM-4 does not play a role for this distance, as it is affected most critically by this effect. For rates up to 200 Gb/s PAM-6 with the noise whitening filter approach performs best, before PAM-8 is the best solution for higher rates.

The exact results shown are specific to the transmission system setup that was available for the measurements. However, the range of different bit rates allows an estimation of the changes in case the component parameters are varied. Comparable to the dispersion induced power fading effect, the BER will be generally increased through stricter bandwidth limitations. Assuming constant noise, this leads to a higher relevance of higher order modulation formats, while relaxed bandwidth limitations make lower order formats like PAM-4 the best solution.

To visualize the impact of CD on the different modulation formats and DSP approaches, the Q penalty for the experimental results is depicted in Fig. 5.37 for a rate of 224/225 Gb/s. The relationship between BER and the Q factor denoted by Q is given by [143]

$$Q = \sqrt{2}\mathrm{erfc}^{-1}(2\mathrm{BER}). \tag{5.1}$$

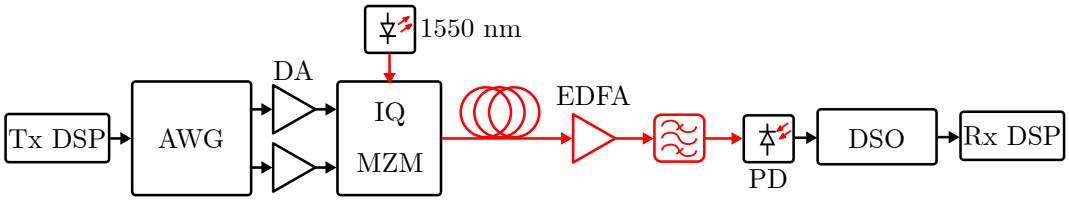

Figure 5.38: Block diagram of the system setup used for simulations and measurements on advanced DD systems.

Here, erfc^{-1} denotes the inverse complementary error function. As observed before, PAM-4 suffers most from CD. The rate of 224 Gb/s over 1 km, i.e. 17 ps/nm of accumulated CD in the channel, is not reached for VNLE only and no DSP approach enables 2 km (34 ps/nm) transmission at this rate. While THP and the DB scheme experience a relatively low Q penalty after 1 km, this penalty lies at 1.5 dB for DFE and above 4 dB for the post-filter approach. For PAM-6 all schemes but VNLE without additional steps as well as the post-filter approach reach 225 Gb/s over 2 km. The DB approach experiences a penalty of more than 2 dB compared to the back-to-back case, while the Q penalty for THP lies at 3.5 dB and for DFE at 6.5 dB. If PAM-8 is used, even VNLE without additional DSP reaches 225 Gb/s over 2 km with a Q penalty of 2 dB. The other DSP approaches experience a comparable penalty of around 1.5 dB.

5.2 Approaches for Advanced DD Systems

In the following part, the schemes described in Sec. 4 are investigated. First, the setup for the simulations and experiments is described, before the obtained results are shown.

5.2.1 System Setup

A subgroup of advanced DD systems that is based on detection with a single PD is investigated in this work. Therefore, the same setup depicted in Fig. 5.38 is used for all simulations and experiments. Only the exact component parameters are varied during simulations. After the complex signal is generated in the transmitter DSP, the AWG generates two analog signals for the inphase and quadrature components. Both analog electrical signals are amplified by DAs before the E/O conversion is done by an IQ MZM. The bias voltages for the modulator are controlled by an automatic bias control (ABC) for the SCOH systems during the experiments. After transmission over the optical fiber, an EDFA is used to provide a constant input power into the receiver. To limit the noise bandwidth, an optical filter is applied. The O/E conversion is performed by a PD before a DSO generates the digital signal that is processed by the receiver DSP. The exact

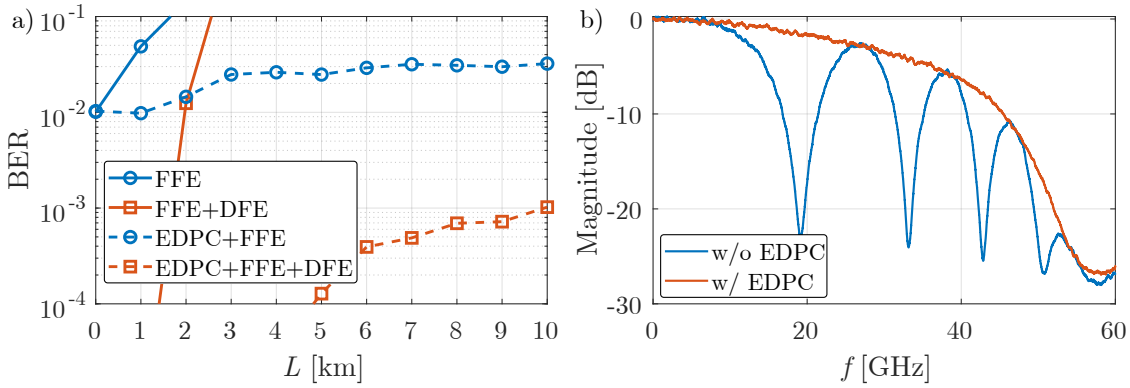

Figure 5.39: Simulative investigations on EDPC. a) shows the performance for 112 GBd PAM-4 over varying fiber lengths and b) shows the received spectra after ADC for 10 km C-band transmission.

component parameters are summarized in the corresponding subsections.

5.2.2 Chromatic Dispersion Pre-Compensation

As seen in the simulative and experimental investigations on IM/DD systems in the previous section, CD can severely impair the transmission performance and even sophisticated DSP can hardly overcome a high amount of it. Therefore, EDPC at the cost of a more complex modulator can be a viable option to overcome this effect. To show the reach extension that can be realized by EDPC, simulations for up to 10 km C-band transmission are depicted in Fig. 5.39. The component parameters can be found in Tab. 5.1, however, the intensity modulator is replaced by an IQ modulator and two AWG channels and DAs are used, as in Fig. 5.38. Figure 5.39 a) shows the BER as a function of the fiber length L. Four cases for the DSP are compared: FFE ($N_1 = 100$, $N_2 = 9$, $N_3 = 9$) and FFE combined with 2-coefficient DFE, both with and without EDPC. The approaches without EDPC suffer from strong CD penalties. While FFE cannot reach 2 km with a BER below 10^{-1}, DFE fails after less than 3 km transmission distance. If EDPC is applied in the transmitter DSP, even 10 km transmission distance only increases the BER by a factor of three for the FFE case. As the EDPC is assumed to compensate the exact amount of CD in the channel, this performance penalty is caused by a decreased SNR due to fiber loss, other fiber effects and potentially an increased quantization noise during DAC. DFE can significantly improve the performance in combination with EDPC and a BER of 10^{-3} results after 10 km transmission. The effect of EDPC on the received signal after 10 km transmission is visualized in Fig. 5.39 b). While the spectrum for the case without EDPC shows various notches caused by power fading, the application of EDPC can completely avoid these.

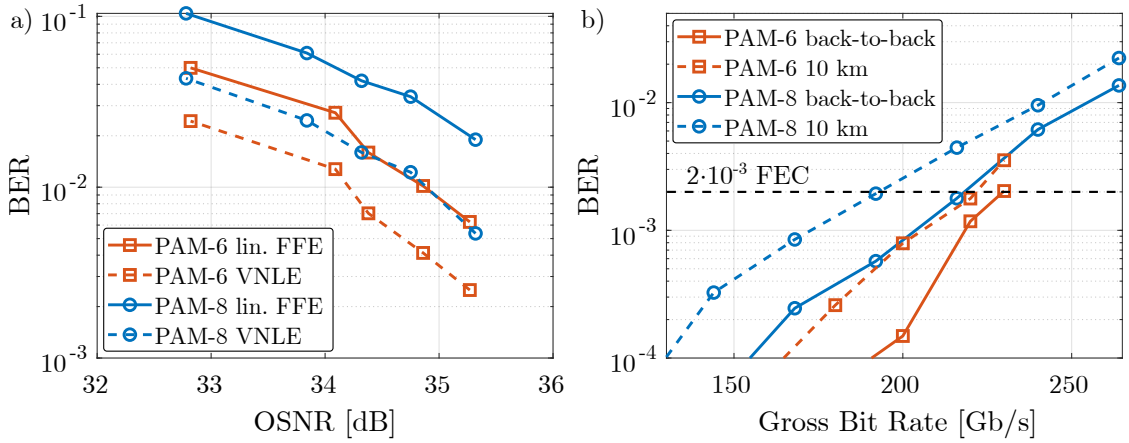

Figure 5.40: Experimental investigations on EDPC. a) shows the BER as a function of the OSNR for 90 GBd PAM-6 and 75 GBd PAM-8 and b) shows the performance for varying symbol rates.

Table 5.10: Parameters of the experimental setup used for investigations on advanced DD approaches. The systems block diagram is depicted in Fig. 5.38.

Component Type	Model Name	Parameters
AWG	Keysight M8196A	3-dB bandwidth: 32 GHz Sampling Rate: 92 GS/s ENOB: ≈ 5.5 bits
DAs	SHF S807	3-dB bandwidth: >50 GHz Gain: 23 dB
PolMux IQ MZM	Oclaro D00521-SN	3-dB bandwidth: 35 GHz
EDFA	HHI MGM FL-1AEC28	-
Optical Filter	Yenista XTract XTA-50	-
PD	u2t XPD2150R	3-dB bandwidth: >50 GHz
DSO	Keysight DSOZ634A	3-dB bandwidth: 63 GHz Sampling Rate: 160 GS/s ENOB: ≈ 5 bits

Experimental investigations on EDPC are shown in Fig. 5.40. The parameters of the setup are summarized in Tab. 5.10. The corresponding results have been published in [144]. Figure 5.40 a) shows the BER as a function of the OSNR for PAM-6 and PAM-8 at a bit rate of 224/225 Gb/s transmitted over 10 km SSMF. PAM-4 is not considered in this comparison, because the limited AWG sampling rate does not allow this bit rate. For both modulation formats, the performance with linear FFE ($N_{\mathrm{FFE}} = 120$) and VNLE ($N_1 = 120$, $N_2 = 5$, $N_3 = 5$) is shown. PAM-6 performs better than PAM-8 for the considered OSNR range. The nonlinear coefficients in VNLE lead to a clear performance improvement for both formats. Figure 5.40 b) shows the performance for both formats at varying bit rates for back-to-back and 10 km transmission, using VNLE in the receiver

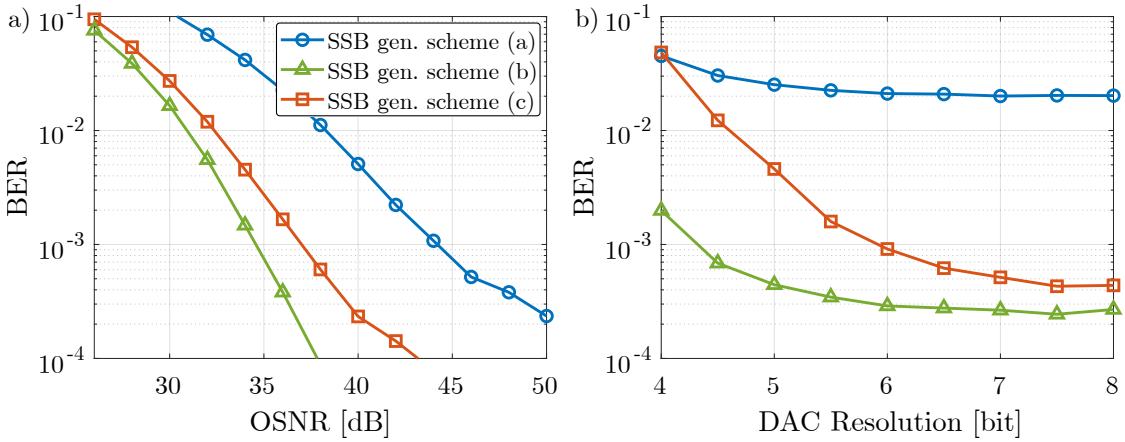

Figure 5.41: Simulative comparison of different SSB signal generation approaches for 56 GBd 16-QAM back-to-back transmission. a) shows the BER as a function of the OSNR and b) shows the impact of the DAC resolution. Scheme (a) refers to the approach of driving the modulator with an electrical SSB signal, scheme (b) adds the carrier in the optical domain and scheme (c) is based on a digital carrier inserted during DSP.

DSP. Note that in the back-to-back case the same signal is transmitted on inphase and quadrature components to increase the optical power. PAM-6 outperforms PAM-8 for all considered rates. Higher rates are reached with PAM-8 due to the limited AWG sampling rate. For both formats a penalty after 10 km transmission compared to the back-to-back case is visible. Besides a slightly decreased SNR due to fiber loss, other fiber effects and potentially increased quantization noise during DAC, also a small deviation between pre-compensated CD and actual CD might be a reason for this penalty. All in all, EDPC can increase the CD tolerance drastically and is an interesting extension compared to IM/DD systems, especially when it comes to longer transmission distances.

5.2.3 Self-Coherent Systems

The investigations on SCOH systems are divided into two main parts. First, the different approaches to generate SSB signals are compared in simulations, before experimental results on the transmission performance are shown. The KK receiver and the SSBI cancellation approaches are compared.

SSB Signal Generation Approaches

As described in Sec. 4.2.1, different approaches to generate optical SSB signals that are required to fulfill the minimum phase condition exist. These approaches are denoted as scheme (a), (b) and (c) in the following. Scheme (a) refers to the approach of driving the IQ modulator with an electrical SSB signal. The optical carrier is generated by setting a proper bias voltage. Scheme (b) generates an optical DSB signal and adds a carrier at one side of the spectrum in the optical domain. Scheme (c) adds a digital tone on

Table 5.11: Parameters of the simulation setup used to compare the different SSB signal generation approaches. The systems block diagram is depicted in Fig. 5.38.

Component Type	Parameters
AWG	3-dB bandwidth: 50 GHz Sampling Rate: 120 GS/s ENOB: $\approx$ 5.5 bits
DAs	3-dB bandwidth: 50 GHz
IQ MZM	3-dB bandwidth: 50 GHz
PD	3-dB bandwidth: 70 GHz
DSO	3-dB bandwidth: 113 GHz Sampling Rate: 256 GS/s ENOB: $\approx$ 5 bits

one side of the spectrum during DSP and drives the modulator at the null point. These three approaches are compared based on 56 GBd 16-QAM simulations and the results are shown in Fig. 5.41. The simulation parameters are summarized in Tab. 5.11. Results for the BER over OSNR are depicted in Fig. 5.41 a). Scheme (a) shows comparatively poor performance. The reason for this is given by the higher transmitter bandwidth requirement of this approach compared to schemes (b) and (c). As the transmitter components get an electrical SSB signal as input, only half the bandwidth can be utilized which impairs the performance for the given parameters. Scheme (b) shows the best performance and scheme (c) lies between the two alternatives. The disadvantage of scheme (c) over scheme (b) lies in the enhanced quantization noise and the lower linear modulator range for the signal due to the digital carrier which is transmitted along with the data signal. To evaluate the impact of quantization noise, the BER in dependence on the DAC resolution is shown for an OSNR of 36 dB in Fig. 5.41 b). The performance of scheme (a) cannot be significantly improved by a higher resolution. For scheme (b) the impact of the DAC resolution is stronger. Especially a low resolution of 4 bits leads to a decreased performance, while approx. 6 bits seem to be sufficient and no further gain is achieved by higher resolutions. Scheme (c) shows the by far strongest relation between performance and DAC resolution. While the performance is on the level of scheme (a) for 4 bits, the performance can be improved by a factor of 100 if a high resolution is available. The performance penalty compared to scheme (b) shrinks with growing resolution. Therefore, the major part of the disadvantage of scheme (c) can be explained by additional quantization noise due to the digital carrier. For the following investigation scheme (c) is considered, since the additional hardware in scheme (b) is critical for cost-sensitive short-reach scenarios. Additionally, the implementation of scheme (c) in the lab is simpler.

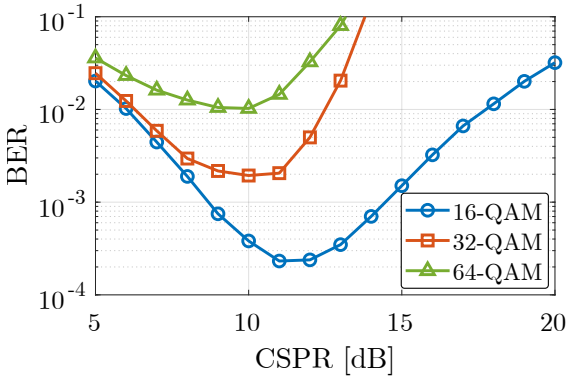

Figure 5.42: Impact of the CSPR on the performance of 16-QAM, 32-QAM and 64-QAM at a constant bit rate of 224/225 Gb/s.

Results for Virtual Carrier Assisted Systems

Several parameters influence the performance of SCOH systems. For the generation of SSB signals, especially the frequency spacing between the carrier and the signal as well as the CSPR are relevant. For the latter parameter, simulations of 16-QAM, 32-QAM and 64-QAM at a constant rate of 224/225 Gb/s are shown in Fig. 5.42. The setup parameters are chosen according to Tab. 5.11. In the receiver DSP, a conventional KK receiver with an oversampling factor of $n_{\mathrm{OS}} = 4$ is deployed. The spacing between carrier and signal is fixed to 1 GHz for these investigations and an OSNR of 40 dB is set. 16-QAM reaches the lowest BER of the three considered modulation formats, which can be explained by the relatively high bandwidth of all components. 32-QAM performs worse by a factor of approx. 10 at the optimal point and 64-QAM again shows a significantly worse performance than 32-QAM. The optimum for the CSPR is lower for higher-order modulation formats. While it lies between 11 dB and 12 dB for 16-QAM, it is between 10 dB and 11 dB for 32-QAM and around 10 dB for 64-QAM. This can be explained by the lower noise tolerance of higher-order formats. While a high CSPR helps to reduce the SSBI term and ensures a fulfillment of the minimum phase condition, it also leads to additional quantization noise on the signal in virtual carrier assisted systems. The stronger the carrier transmitted along with the signal, the less effective resolution is available for the data carrying signal. The closer the symbol levels are spaced, the stronger this effect impairs the overall performance.

Investigations on the DC-Value Method The DCV-method is the only iterative procedure considered in this work to remove the SSBI from the received signal. To investigate the impact of the iteration number, 56 GBd 16-QAM simulations are shown in Fig. 5.43 based on the setup in Tab. 5.11. Oversampling factors of $n_{\mathrm{OS}} = 2.5$ and $n_{\mathrm{OS}} = 4$ are considered and the performance of a conventional KK receiver is given as a benchmark.

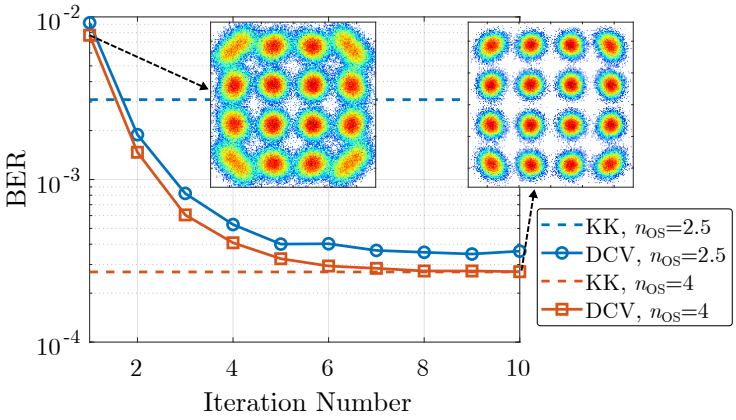

Figure 5.43: Simulations on the performance of the DCV method for varying iteration numbers. 16-QAM is transmitted at a symbol rate of 56 GBd and oversampling factors of $n_{\mathrm{OS}} = 2.5$ and $n_{\mathrm{OS}} = 4$ are considered. The insets show the constellations after receiver FFE for 1 and 10 iterations.

The performance with the KK receiver is heavily impaired, if the oversampling factor is reduced. While a BER below $3 \cdot 10^{-4}$ is reached at $n_{\mathrm{OS}} = 4$, the performance is worse by a factor of 10 for $n_{\mathrm{OS}} = 2.5$. The performance of the DCV-method is strongly dependent on the iteration number. While a single iteration results in poor performance, few iterations are sufficient to decrease the BER significantly. For both oversampling rates, the performance saturates at approx. 7 iterations. For $n_{\mathrm{OS}} = 4$ the performance of the DCV-method approaches the KK performance. Only a small penalty is observed if the oversampling factor is reduced to $n_{\mathrm{OS}} = 2.5$. In this case, the KK receiver with the same oversampling is clearly outperformed. The results show that the DCV-method can effectively remove the SSBI. If sufficient iterations are used, no visible penalty compared to the KK receiver exists at high oversampling. Due to the avoidance of the nonlinear operations (except for the square root) the performance at a low oversampling is significantly better than for the KK receiver. However, a high number of iterations for the DCV-method leads to a high complexity due to the multiplications as well as FFT and IFFT per iteration.

Investigations on SSBI Cancellation Approaches For the considered SSBI cancellation approaches, one or two scaling factors need to be optimized. While the schemes only need a few steps and are therefore desirable in terms of complexity, the optimization of the scaling factors is not straightforward. The optimal values for these factors need to be found by an extensive search. Figure 5.44 shows the results for a sweep through the scaling factors γ_1 and γ_2 based on the approach in Fig. 4.5 b). An optimum in terms of resulting BER is found at $\gamma_1 \approx 0.5$ and $\gamma_2 \approx 0.05$. The approach based on a single scaling factor (Fig. 2.11 a)) corresponds to the case $\gamma_1 = 0$. As visible, the addition

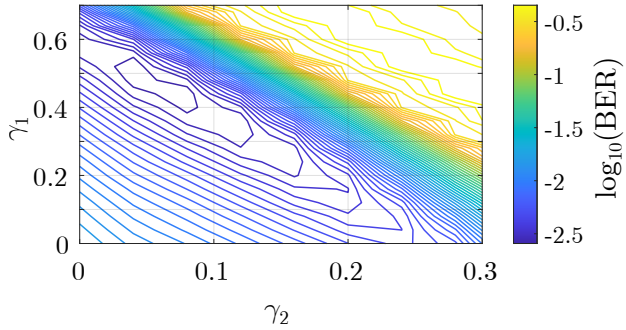

Figure 5.44: Impact of the scaling factors γ_1 and γ_2 on the performance of the SSBI cancellation approach.

of the non-squared term can significantly improve the performance compared to this case. Interestingly, the non-squared term is even more relevant for the performance than the squared term, as visible when comparing the cases of $\gamma_1 = 0$ and $\gamma_2 = 0$. For the investigated data, it would therefore be advantageous to change the single term approach by removing the squaring operation.

Comparison of Field Reconstruction and SSBI Cancellation Approaches For a comparison of the different field reconstruction and SSBI cancellation approaches, the oversampling factor in the receiver DSP plays an important role. As explained in Sec. 4.2.2, the conventional KK receiver requires digital oversampling for the nonlinear operations. Therefore it is expected that it can be outperformed at lower oversampling rates. To have a comprehensive comparison of the introduced schemes, all approaches are compared based on 56 GBd 16-QAM back-to-back data measured on the setup in Tab. 5.11. The results are depicted in Fig. 5.45. Eight different DSP variations are considered. Besides the straightforward approach of using no SSBI cancellation at all, the conventional KK receiver and the modified KK approach that aims at a reduction of the oversampling demand are shown. Additionally, the SSBI cancellation approaches using either one or two scaling factors (cf. Figure 4.5) are considered. Finally, the DCV method with two, four and six iterations is given. Obviously, the performance without any SSBI cancellation is worst and the BER saturates above a value of 10^{-2} even for high oversampling. Besides this, the KK receiver is the worst approach for oversampling factors of $n_{\mathrm{OS}} \leq 2.4$. However, the performance significantly improves for higher oversampling rates and for oversampling factors of $n_{\mathrm{OS}} \geq 3.5$ it shows the best performance of all considered approaches. The modified KK approach shows a significantly better performance for low oversampling factors and results in a slightly higher BER than the conventional KK receiver for $n_{\mathrm{OS}} \geq 3$. Concerning the scaling factor based SSBI cancellation approaches, it is visible that the scheme using a single scaling factor saturates at a comparatively

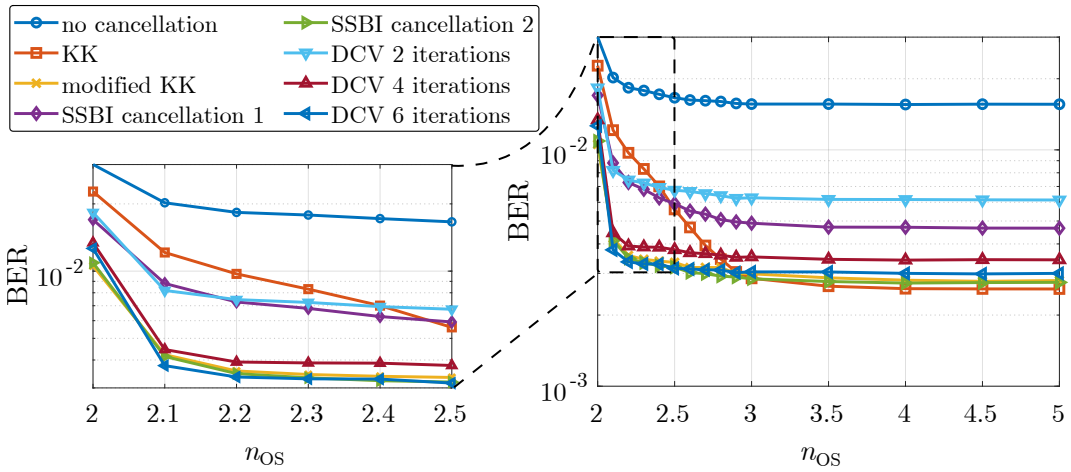

Figure 5.45: Performance in dependence on the oversampling factor n_{OS} for experimental 56 GBd 16-QAM data.

high BER. The approach based on two scaling factors, however, performs well for all oversampling rates and generally shows very similar results to the modified KK receiver. The DCV method performs poorly when only two iterations are passed, but the BER is significantly reduced for higher iteration counts. For six iterations, the performance is marginally better than for any other approach at oversampling factors $2.1 \leq n_{OS} \leq 2.3$. For higher oversampling, the performance is slightly worse than that of the modified KK receiver.

In summary, the conventional KK receiver is the best approach, if sufficient oversampling is available due to the ideal SSBI cancellation. For lower oversampling factors, the modified KK receiver, the SSBI cancellation approach with two scaling factors and the DCV method with a high number of iterations are good alternatives.

As the previous investigations are only based on the highest reachable OSNR for the experimental setup, it is interesting to compare different schemes for varying OSNR values. This is done based on the same experimental setup for 56 GBd 16-QAM back-to-back data. Selected approaches showing promising performance in the previous results are used for the comparison, namely the conventional KK receiver, the modified KK, the SSBI cancellation using two scaling factors and the DCV method with six iterations. The results are depicted in Fig. 5.46. According to the previous insights, an oversampling factor of $n_{OS} = 4$ is chosen for the conventional KK receiver. In this case, the best performance for all OSNR values is reached. Besides a curve for linear FFE, the performance after VNLE with $N_1 = 120$, $N_2 = 5$, $N_3 = 5$ is shown. The additional nonlinear coefficients only lead to a minor gain. Reasons for this are the large linear range of the modulator driven at

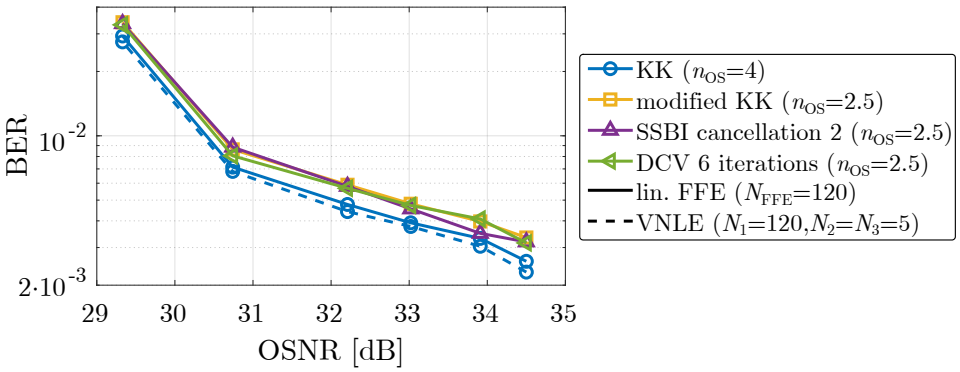

Figure 5.46: BER as a function of the OSNR for 56 GBd 16-QAM back-to-back data. Selected reconstruction schemes are compared.

the null point and the completely canceled SSBI at the input of the equalizer. According to this, it can be concluded that linear FFE is sufficient for the given data. For the alternative approaches, an oversampling factor of $n_{\mathrm{OS}} = 2.5$ is applied. All approaches show a near identical performance and a small penalty compared to conventional KK is observed. Lower BER values for all schemes are restricted by the relatively low reachable OSNR for the experimental setup.

5.2.4 Comparison of Advanced DD Approaches

To evaluate the relative performance of the advanced DD systems considered in this work, namely EDPC and SCOH systems based on a single PD, the results shown in the previous parts are compared. This comparison has been published in [144]. For the SCOH systems, only the KK receiver with a sufficient oversampling factor of $n_{\mathrm{OS}} = 4$ is considered. As shown in the previous part, this approach leads to the best performance of all considered field reconstruction approaches. The comparison of the advanced DD approaches is shown in Fig. 5.47. Figure 5.47 a) shows the BER as a function of the OSNR for 16-QAM, 32-QAM and 64-QAM based on SCOH detection as well as PAM-6 and PAM-8 with EDPC, all at a rate of 224/225 Gb/s. For all cases, linear FFE with $N_{\mathrm{FFE}} = 120$ coefficients and VNLE with memory lengths of $N_1 = 120$, $N_2 = 5$, $N_3 = 5$ are considered. While 16-QAM and 32-QAM perform nearly identically, 64-QAM shows a worse performance at the given rate. The 56 GBd 16-QAM signal faces a penalty due to bandwidth limitations but has the highest noise tolerance of the considered schemes. For the 32-QAM format, 50 GBd are sufficient to reach 225 Gb/s, leading to a lower penalty by bandwidth limitations. Due to the lower noise tolerance, the performance is similar to that reached with 16-QAM. The high number of amplitude levels in 64-QAM further reduces the noise tolerance, leading to a decreased performance. For all SCOH formats, the gain by using VNLE instead of linear FFE is negligible. As described in the previous

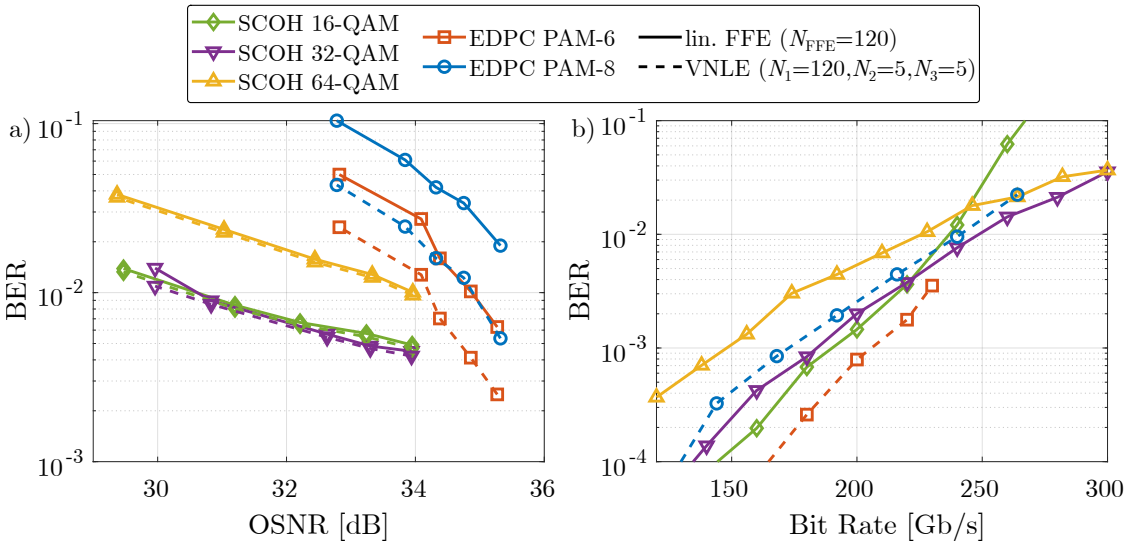

Figure 5.47: Comparison of the considered advanced DD approaches for 10 km transmission. a) shows the BER as a function of the OSNR for a rate of 224/225 Gb/s and b) shows the performance for different rates at the maximum reachable OSNR.

part, the main reasons for this are the large linear range of the modulator driven at the null point and the absence of SSBI after field reconstruction.

The results for EDPC have already been discussed in Sec. 5.2.2. When comparing the results for SCOH and EDPC, it is observed that the lowest BER for a given OSNR is reached by the SCOH schemes. However, a higher OSNR is reached with EDPC which is explained by the different bias points used at the modulator. At the highest reachable OSNR, PAM-6 with VNLE reaches the lowest overall BER. The performance reached with PAM-8 is similar to that of 16-QAM and 32-QAM.

To get a broader overview of the relative performance, the BER for different bit rates at the highest reachable OSNR is depicted in Fig. 5.47 b). For rates up to 230 Gb/s, the best performance is reached using PAM-6 with EDPC and VNLE. Higher rates for this format are restricted by the AWG sampling rate of 92 GS/s. For higher rates up to 300 Gb/s, SCOH detection with 32-QAM shows the best results.

From a complexity and practicability perspective, several remarks have to be made. EDPC can only be performed, if the amount of CD in the channel is known at the transmitter. As this information can only be accessed at the receiver, a feedback channel for this information is necessary for practical implementation. This requirement is avoided for SCOH reception. To perform the field reconstruction with a conventional KK receiver, digital oversampling is required which increased the computational complexity. However, as shown in the previous part, several approaches to reduce the necessary oversampling

with only minor performance penalty exist. While an equalizer with coefficients for the inphase and quadrature components is required for the complex symbol constellations used in SCOH reception, the sampling rate is reduced compared to the real-valued constellations used in combination with EDPC. The performance advantage of PAM-6 with EDPC is only reached when nonlinear equalization is applied, which increases the computational complexity.

Chapter 6

Conclusions and Outlook

In this work, different solutions for increasing data rates and transmission distances in optical intra-datacenter transmission systems have been investigated. Two reach scenarios for this application were treated: connections between leaf and spine switches inside a single datacenter with up to 2 km transmission distance, as well as an increased distance of up to 10 km to cover the connections between co-located datacenters on a single campus. To address the next generations of 800 Gb/s and 1.6 Tb/s systems, the focus was set on the transmission of 200 Gb/s per lane and beyond.

To cover the transmission distance scenario of up to 2 km, intensity-modulation and direct-detection systems were considered as a cost-efficient solution. These systems suffer from several impairments that limit the reachable rate and performance. Electrical bandwidth limitations of the components at the transmitter and receiver limit the reachable symbol rates, as high frequencies are severely attenuated during transmission. The end-to-end 3-dB bandwidth of current commercially available setups hardly reaches 50 GHz so that symbol rates beyond 100 GBd require digital signal processing to be realized. The lowpass characteristic of the channel is further increased by the interaction between chromatic dispersion and direct-detection. The resulting power fading effect induces strong attenuations of certain frequencies and leads to spectral nulls. For the considered short transmission distances spectral nulls do typically not lie inside the signal spectrum but the effect still leads to an attenuation of high signal frequencies. Besides the lowpass characteristic of the channel, nonlinear effects impair the performance. Significant nonlinearities can be induced by the modulator characteristic and the square-law detection of the photodiode. Additionally, electrical amplifiers such as the driver amplifier used before the electrical-to-optical conversion can induce a nonlinear gain. Noise sources are typically given by amplifiers in the electrical and optical domain, if applicable, as well as by quantization during the digital-to-analog and analog-to-digital conversion.

Several DSP approaches to overcome certain impairments and improve the transmission performance under constrained conditions were introduced and evaluated in this work. A

well-established approach is given by feed-forward equalization. However, under strong lowpass characteristics of the channel, this approach suffers from noise enhancement due to strong amplifications of high signal frequencies. Several approaches to mitigate this effect and therefore increase the reachable rates are shown and compared. These approaches include transmitter DSP schemes such as partial response signaling, Tomlinson-Harashima pre-coding and bandwidth pre-compensation as well as receiver DSP schemes such as decision-feedback equalization and noise whitening filters. Besides this, approaches to combat nonlinearities are investigated. These include a non-regular spacing of the PAM amplitude levels to overcome modulator nonlinearities as well as Volterra nonlinear equalization as a general approach. Different solutions to reduce the complexity of VNLE are shown. Finally, also approaches specifically focussing on CD induced power fading are shown. While these schemes are hardly applicable for the considered transmission distances, increased reaches and higher symbol rates can make them become relevant. All the mentioned schemes are evaluated based on simulative and experimental data, combinations of different approaches are considered and the capabilities to overcome impairments in high-rate IM/DD systems are compared. It has been shown that duobinary equalization offers a good performance and a high CD tolerance. For the most constrained conditions, THP offers the best capabilities. The application of a post-filter after FFE results in low BERs under less severe impairments. Combinations of different approaches, such as partial DFE and post-filtering show promising results and could be interesting for systems with strong lowpass characteristics, despite the increased complexity. VNLE can significantly improve the overall performance compared to linear equalization but the number of coefficients needs to be reduced for a reasonable complexity. In general, the DSP needs to be carefully chosen according to the exact impairments in the considered system and the desired rate and modulation format. This work shows an overview of different options and their capabilities.

The increased amount of CD in datacenter campus links with up to 10 km transmission distance motivates the consideration of advanced DD systems, that allow an increased tolerance to this fiber effect. Advanced DD systems refer to intermediate solutions between IM/DD and coherent systems in terms of hardware demand. While various setups fall into this group, only a specific hardware configuration is considered in this work. This configuration replaces the intensity modulator with an IQ modulator but still uses a single PD for detection. This setup enables electronic dispersion pre-compensation in the transmitter DSP or the transmission of minimum phase signals that can be utilized for self-coherent detection. For the latter approach besides the well-known Kramers-Kronig receiver alternative field reconstruction and SSBI cancellation approaches are investigated

and compared. It is shown that several approaches can improve the performance at low oversampling factors compared to the KK receiver. Especially the modified KK receiver, the DC-value method and a two-stage SSBI cancellation approach show promising results. Comparing EDPC and SCOH systems, the best performance is reached with the former and PAM-6 as a modulation format. However, this performance comes at the cost of nonlinear equalization. SCOH systems offer the advantage of being capable of EDC at the receiver which avoids the demand for channel information at the transmitter. This is an important consideration for the implementation in practical systems.

Over recent years, coherent systems were deployed for applications with shorter transmission distances. By now, they are used in all distances from datacenter interconnect to long-haul. Solely intra-datacenter links are still covered by IM/DD systems. Subsequently, the power consumption of coherent systems was improved, leading to considerations of even applying these systems inside datacenters or especially in datacenter campus networks. However, as high numbers of transceivers are necessary for these short-reach applications, the hardware demand and cost per transceiver as well as the power consumption are more critical factors than for longer reaches, where the fiber cost plays an important role. The hardware and DSP demand for IM/DD and coherent systems as well as advanced DD systems based on detection with a single PD are summarized in Tab. 6.1. For IM/DD and advanced DD systems four wavelengths are required to reach the same rate as coherent PolMux systems. According to this, four lasers are required. However, for both systems, the linewidth tolerance is high, while coherent systems require more expensive lasers with a low linewidth. The transmitter complexity is similar for IM/DD and coherent systems, while advanced DD systems need more modulators and digital-to-analog converters. At the receiver, coherent systems increase the hardware demand compared to the other configurations by using balanced PDs, 90° hybrids, polarization splitters and most importantly an additional low linewidth laser as local oscillator. Additionally, coherent systems require carrier recovery and IQ imbalance correction in the receiver DSP, making this step more complex than for IM/DD systems.

Considering the system complexity, there are good reasons to continue using IM/DD systems for intra-datacenter applications. However, the reachable transmission distance shrinks with growing symbol rates, as CD becomes more and more critical. As soon as the number of channels needs to be increased to transmit the same rate as a coherent PolMux system, the complexity advantage of IM/DD systems may get lost. The DSP approaches shown in this work can be used to increase the impairment tolerance of these systems and could help to keep the channel count low. However, the additional computational

Table 6.1: Hardware and DSP demand for different transmission system configurations.

	IM/DD	Advanced DD*	Coherent (PolMux)
WDM Channels	4	4	1
Lasers	4	4	1, Low Linewidth
DACs/ADCs	4/4	8/4	4/4
Modulation	4 Intensity Modulators	4 IQ Modulators	1 PolMux IQ Modulator
Photodiodes	4, Single-Ended	4, Single-Ended	4, Balanced
Additional Optics	Multiplexer, De-multiplexer	Multiplexer, De-multiplexer	90° Hybrid, Polarization Splitters, Local Oscillator
DSP	Equalization	EDC/Field Rec., Equalization	Carrier Recovery, IQ Imbalance Correction, MIMO Equalization

*Only systems using a single PD per lane for detection are considered here.

complexity needs to be reasonable to keep the advantage over coherent systems. Advanced DD systems could form a transition technology before coherent systems eventually take over intra-datacenter transmission systems.

List of Abbreviations

ABC	automatic bias control
ADC	analog-to-digital converter
ASK	amplitude shift keying
ASE	amplified spontaneous emission
AWG	arbitrary waveform generator
AWGN	additive white Gaussian noise
BER	bit error ratio
BW	bandwidth
CD	chromatic dispersion
CSPR	carrier-to-signal power ratio
CW	continuous wave
CWDM	coarse wavelength division multiplexing
CR	coherent receiver
DA	driver amplifier
DAC	digital-to-analog converter
DB	duobinary
DC	direct current
DCF	dispersion compensating fiber
DCR	datacenter
DCV	DC-value
DD	direct-detection

DFE decision-feedback equalization

DML directly modulated laser

DSB double-sideband

DSO digital storage oscilloscope

DSP digital signal processing

EAM electro-absorption modulator

EDC electronic dispersion compensation

EDFA Erbium-doped fiber amplifier

EDPC electronic dispersion pre-compensation

EDS effective data sequence

EML electro-absorption modulated laser

ENOB effective number of bits

E/O electrical-to-optical

ER extinction ratio

FEC forward error correction

FFE feed-forward equalization

FFT fast Fourier transform

FIR finite impulse response

FR far reach

FWM four-wave mixing

GS Gerchberg-Saxton

HD hard decision

IFFT inverse fast Fourier transform

IIR infinite impulse response

IM intensity-modulation

IQ inphase-quadrature

ISI inter-symbol interference

KK Kramers-Kronig

LMS least mean squares

LO local oscillator

LR long reach

MMF multi mode fiber

MMSE minimum mean square error

MP memory polynomial

MZI Mach-Zehnder interferometer

MZM Mach-Zehnder modulator

NUQ non-uniformly quantized

O/E optical-to-electrical

OOK on-off keying

OSNR optical signal-to-noise ratio

PDFE partial decision-feedback equalizer

PAM pulse amplitude modulation

PAPR peak-to-average power ratio

PBC polarization beam combiner

PBS polarization beam splitter

PD photodiode

PMD polarization mode dispersion

PolMux polarization multiplexing

PR partial response

PRBS pseudo-random binary sequence

PSD power spectral density

QAM quadrature amplitude modulation

RF radio frequency

RI restricted interval

ROF roll-off factor

ROP received optical power

ROADM reconfigurable optical add-drop multiplexer

RC raised cosine

RRC root-raised cosine

SCOH self-coherent

SBS stimulated Brillouin scattering

SD soft decision

SFPC selected frequency pre-compensation

SNR signal-to-noise ratio

SOA semiconductor optical amplifier

SPM self-phase modulation

SpS samples per symbol

SRS stimulated Raman scattering

SSB single-sideband

SSBI signal-signal beat interference

SSMF standard single mode fiber

TEC thermoelectric cooler

THP Tomlinson-Harashima pre-coding

TIA transimpedance amplifier

ToR top of rack

VE Viterbi equalization

VNLE Volterra nonlinear equalization

VOA variable optical attenuator

WDFE weighted decision-feedback equalization

WDM wavelength division multiplexing

XPM cross-phase modulation

List of Symbols

A	amplitude
B_f	feedback filter transfer function
B	bandwidth
C	number of coefficients
D_{PMD}	PMD parameter
D_{S}	dispersion slope parameter
D	dispersion parameter
E_0	carrier
E_{in}	input electrical field
E_{out}	output electrical field
F_{MSE,ℓ_1}	minimum mean square error cost function with ℓ_1 penalty term
F_{MSE}	minimum mean square error cost function
F_{N}	noise figure
G	amplifier gain
$H_{\mathrm{CD,DD}}$	chromatic dispersion frequency response in a direct-detection system
H_{C}	channel frequency response
H_{DB}	transfer function of the duobinary filter
H_{EML}	transfer function of the electro-absorption modulator
H_{GVD}	group velocity dispersion frequency response
H_{MZM}	transfer function of the Mach-Zehnder modulator
H_{PR}	transfer function of partial response filter
H_{SSMF}	transfer function of the optical fiber
H	frequency repsonse
I_{max}	upper limit
I	intensity
L	fiber length

M	order of the symbol constellation
N_{DFE}	number of DFE coefficients
N_{FFE}	number of FFE coefficients
N_d	upper limit
N	memory length
P_{in}	input optical power
P_{out}	output optical power
P	optical power
Q	Q-factor
R_{PD}	responsivity
S	state
V_π	characteristic voltage of an MZM
Δf	frequency chirp
Λ_p	sum path metric
α_{PR}	partial response coefficient
α_{THP}	THP coefficient
α_{C}	chirp parameter
α_{dB}	attenuation coefficient
α	fiber loss
β_{ro}	roll-off factor
β	phase constant of dispersion
ϵ	error
γ_k	reliability value
γ	scaling factor
$\hat{d}$	received symbol sequence
$\hat{k}$	reflection coefficient
$\hat{x}_{\mathrm{out}}$	hard decision on equalizer output
λ_p	path metric
λ	wavelength
$\mathbf{C}$	vector containing the number of coefficients
$\mathbf{R}_{xx}$	auto-correlation matrix of x
$\mathbf{b}$	DFE coefficient vector

$\mathbf{h}$	equalizer coefficient vector
$\mathbf{l}$	FIR filter coefficient vector
$\mathbf{r}_{xd}$	cross-correlation vector of x and d
μ	step size
ω_c	carrier frequency
ω	angular frequency
$\overline{x}_{\text{out}}$	weighted decision on equalizer output
$\overline{x}_{\text{Tx}}$	DC-part of the transmitted optical signal
$\overline{x}$	modulator DC input
ϕ	phase
σ_{T}	PMD induced pulse broadening
$\tilde{x}_{\text{Tx}}$	DC-free part of the transmitted optical signal
$\tilde{x}$	modulator drive signal
a_0	initial signal
a_s	steepness parameter
a_{min}	minimum attenuation
a_{out}	output signal
a	transmitted signal
b_{PR}	pre-coded sequence
b_s	compression factor
b	DFE coefficient
c_{PR}	partial response sequence
c	speed of light
d_{max}	maximum spacing between samples participating in a coefficient
d_{min}	threshold constant
d_t	training symbols
d	transmitted symbol sequence
e	forward prediction error
f	frequency
g	backward prediction error
h_{Ch}	channel impulse response
h_{DC}	equalizer DC coefficient

h_{C}	channel impulse response
h_{Rx}	receiver impulse response
h_{Tx}	transmitter impulse response
h	FFE coefficient
i	photocurrent
l	FIR filter coefficient
n_{OS}	oversampling factor
p	precoding sequence
r_c	constant ratio
r	received signal
s_{SSB}	single-sideband signal
s	state content
u_D	modulator drive voltage
u_{bias}	modulator bias voltage
v	effective data sequence
x_{in}	equalizer input
x_{out}	equalizer output
x_{Rx}	received optical signal
x_{Tx}	transmitted optical signal
x	transmitted signal
y	recieved electrical signal

Bibliography

[1] P. J. Winzer, D. T. Neilson, and A. R. Chraplyvy, "Fiber-optic transmission and networking: the previous 20 and the next 20 years," *Opt. Express*, vol. 26, no. 18, pp. 24190–24239, 2018.

[2] E. Desurvire, J. R. Simpson, and P. C. Becker, "High-gain erbium-doped traveling-wave fiber amplifier," *Opt. Lett.*, vol. 12, no. 11, pp. 888–890, 1987.

[3] R. J. Mears, L. Reekie, I. M. Jauncey, and D. N. Payne, "Low-noise erbium-doped fibre amplifier operating at 1.54μm," *Electron. Lett.*, vol. 23, no. 19, pp. 1026–1028, 1987.

[4] X. Zhou, R. Urata, and H. Liu, "Beyond 1 Tb/s Intra-Data Center Interconnect Technology: IM-DD OR Coherent?," *Journal of Lightwave Technology*, vol. 38, no. 2, pp. 475–484, 2020.

[5] 800G Pluggable Multi-Source Agreement, "Enabling The Next Generation of Cloud & AI using 800 Gb/s Optical Modules," [Online]. Available: https://www.800gmsa.com/news/white-paper, 2020.

[6] E. Agrell, M. Karlsson, A. R. Chraplyvy, D. J. Richardson, P. M. Krummrich, P. Winzer, K. Roberts, J. K. Fischer, S. J. Savory, B. J. Eggleton, M. Secondini, F. R. Kschischang, A. Lord, J. Prat, I. Tomkos, J. E. Bowers, S. Srinivasan, M. Brandt-Pearce, and N. Gisin, "Roadmap of optical communications," *Journal of Optics*, vol. 18, no. 6, p. 063002, 2016.

[7] K. Schmidtke, "Cloud-scale computing," Plenary Talk, 2019 European Conference on Optical Communication (ECOC), 2019.

[8] F. Chang, *Datacenter Connectivity Technologies: Principles and Practice*. River Publishers, 2017.

[9] IEEE B400G study group, "IEEE B400G study group," website, https://www.ieee802.org/3/B400G, accessed on 2022/07/14.

[10] IEEE P802.3df 200 Gb/s, 400 Gb/s, 800 Gb/s, and 1.6 Tb/s Ethernet Task Force, "IEEE P802.3df 200 Gb/s, 400 Gb/s, 800 Gb/s, and 1.6 Tb/s Ethernet Task Force," website, https://www.ieee802.org/3/df, accessed on 2022/07/14.

[11] R. Nagarajan, I. Lyubomirsky, and O. Agazzi, "Low Power DSP-Based Transceivers for Data Center Optical Fiber Communications (Invited Tutorial)," *Journal of Lightwave Technology*, vol. 39, no. 16, pp. 5221–5231, 2021.

[12] C. Xie and J. Cheng, "Coherent Optics for Data Center Networks," in *2020 IEEE Photonics Society Summer Topicals Meeting Series (SUM)*, pp. 1–2, 2020.

[13] F. Gao, S. Zhou, X. Li, S. Fu, L. Deng, M. Tang, D. Liu, and Q. Yang, "2 x 64 Gb/s PAM-4 transmission over 70 km SSMF using O-band 18G-class directly modulated lasers (DMLs)," *Opt. Express*, vol. 25, no. 7, pp. 7230–7237, 2017.

[14] K. Zhang, Q. Zhuge, H. Xin, Z. Xing, M. Xiang, S. Fan, L. Yi, W. Hu, and D. V. Plant, "Demonstration of 50Gb/s/l Symmetric PAM4 TDM-PON with 10G-class Optics and DSP-free ONUs in the O-band," in *2018 Optical Fiber Communications Conference and Exposition (OFC)*, pp. 1–3, 2018.

[15] K. Zhang, Q. Zhuge, H. Xin, W. Hu, and D. V. Plant, "Performance comparison of DML, EML and MZM in dispersion-unmanaged short reach transmissions with digital signal processing," *Opt. Express*, vol. 26, no. 26, pp. 34288–34304, 2018.

[16] C.-C. Wei, H.-L. Cheng, and W.-X. Huang, "On Adiabatic Chirp and Compensation for Nonlinear Distortion in DML-Based OFDM Transmission," *Journal of Lightwave Technology*, vol. 36, no. 16, pp. 3502–3513, 2018.

[17] G. P. Agrawal, *Fiber-Optic Communications Systems.* John Wiley & Sons, Inc., 2002.

[18] E. Säckinger, *Broadband Circuits for Optical Fiber Communication.* John Wiley & Sons, Inc., 2005.

[19] J. L. Wei, K. Grobe, C. Sanchez, E. Giacoumidis, and H. Griesser, "Comparison of cost- and energy-efficient signal modulations for next generation passive optical networks," *Opt. Express*, vol. 23, no. 22, pp. 28271–28281, 2015.

[20] A. Samani, M. Chagnon, E. El-Fiky, D. Patel, M. Jacques, V. Veerasubramanian, and D. V. Plant, "Silicon photonics modulator architectures for multi-level signal generation and transmission," in *2017 Optical Fiber Communications Conference and Exhibition (OFC)*, pp. 1–3, 2017.

[21] M. Jacques, Z. Xing, A. Samani, E. El-Fiky, X. Li, S. Lessard, and D. V. Plant, "200 Gbit/s net rate transmission over 2 km with a silicon photonic segmented MZM," in *45th European Conference on Optical Communication (ECOC 2019)*, pp. 1–4, 2019.

[22] F. Zhang, Y. Zhu, F. Yang, L. Zhang, X. Ruan, Y. Li, and Z. Chen, "Up to single lane 200g optical interconnects with silicon photonic modulator," in *2019 Optical Fiber Communications Conference and Exhibition (OFC)*, pp. 1–3, 2019.

[23] M. Li, L. Wang, X. Li, X. Xiao, and S. Yu, "Silicon intensity mach-zehnder modulator for single lane 100-gb/s applications," *Photon. Res.*, vol. 6, no. 2, pp. 109–116, 2018.

[24] Q. Hu, R. Borkowski, Y. Lefevre, F. Buchali, R. Bonk, K. Schuh, E. D. Leo, P. Habegger, M. Destraz, N. D. Medico, H. Duran, V. Tedaldi, C. Funck, Y. Fedoryshyn, J. Leuthold, W. Heni, B. Baeuerle, and C. Hoessbacher, "Plasmonic-mzm-based short-reach transmission up to 10 km supporting >304 gbd polybinary or 432 gbit/s pam-8 signaling," in *2021 European Conference on Optical Communication (ECOC)*, pp. 1–4, 2021.

[25] C. Hoessbacher, B. Baeuerle, E. De Leo, N. Del Medico, H. Duran, N. Guesken, P. Habegger, W. Heni, and N. Meier, "Progress and challenges of plasmonics for efficient and high-speed optical communications," in *2021 Conference on Lasers and Electro-Optics (CLEO)*, pp. 1–2, 2021.

[26] U. Koch, C. Uhl, H. Hettrich, Y. Fedoryshyn, C. Hoessbacher, W. Heni, B. Baeuerle, B. I. Bitachon, A. Josten, M. Ayata, H. Xu, D. L. Elder, L. R. Dalton, E. Mentovich, P. Bakopoulos, S. Lischke, A. Krüger, L. Zimmermann, D. Tsiokos, N. Pleros, M. Möller, J. Leuthold, "A monolithic bipolar CMOS electronic-plasmonic high-speed transmitter," *Nat Electro*, vol. 3, pp. 338–345, 2020.

[27] A. Melikyan, N. Kaneda, K. Kim, Y. Baeyens, and P. Dong, "Differential drive i/q modulator based on silicon photonic electro-absorption modulators," *Journal of Lightwave Technology*, vol. 38, no. 11, pp. 2872–2876, 2020.

[28] A. W. Leonid Kazovsky, Sergio Benedetto, *Optical Fiber Communication Systems*. JArtech House, Inc., 1996.

[29] Y. Nishida, M. Yamada, T. Kanamori, K. Kobayashi, J. Temmyo, S. Sudo, and Y. Ohishi, "Development of an efficient praseodymium-doped fiber amplifier," *IEEE Journal of Quantum Electronics*, vol. 34, no. 8, pp. 1332–1339, 1998.

[30] D. Zimmerman and L. Spiekman, "Amplifiers for the masses: Edfa, edwa, and soa amplets for metro and access applications," *Journal of Lightwave Technology*, vol. 22, no. 1, pp. 63–70, 2004.

[31] S. Ohlendorf, S. Pachnicke, and W. Rosenkranz, "Bandwidth-variable dwdm transmission for data center interconnects using multidimensional pam," in *2018 Asia Communications and Photonics Conference (ACP)*, pp. 1–3, 2018.

[32] S. Ohlendorf, R. Joy, S. Pachnicke, and W. Rosenkranz, "Flexible pam in dwdm transmission with kramers-kronig dsp," in *2018 European Conference on Optical Communication (ECOC)*, pp. 1–3, 2018.

[33] G. P. Agrawal, *Nonlinear Fiber Optics*. Elsevier Inc., 2013.

[34] A. Ali, *Investigation of OFDM-transmission for direct detection optical systems*. Kieler Berichte zur Nachrichtentechnik, Band 12, Dissertation, Shaker Verlag, 2012.

[35] M. Chagnon, "Optical communications for short reach," *Journal of Lightwave Technology*, vol. 37, no. 8, pp. 1779–1797, 2019.

[36] R. Rath, *Investigation of Digital Signal Processing Techniques for Compensation of Linear and Nonlinear Impairments in Fiber-Optical Communication Systems*. Kieler Berichte zur Nachrichtentechnik, Band 20, Dissertation, Shaker Verlag, 2020.

[37] S. Ohlendorf, *Experimental Demonstration of Flexible Modulation Formats for Optical Data Center Interconnects*. Kieler Berichte zur Nachrichtentechnik, Band 22, Dissertation, Shaker Verlag, 2021.

[38] A. E. Willner, *Optical Fiber Telecommunications VII*. Elsevier, Inc., 2019.

[39] W. Shieh, C. Sun, H. Ji, "Carrier-assisted differential detection," *Light Sci Appl*, vol. 9, no. 18, 2020.

[40] J. Li, Z. Wang, H. Ji, X. Li, H. Chen, R. R. Unnithan, W. Shieh, and Y. Su, "High electrical spectral efficiency silicon photonic receiver with carrier-assisted differential detection," in *2022 Optical Fiber Communications Conference and Exhibition (OFC)*, pp. 1–3, 2022.

[41] X. Li, M. O'Sullivan, Z. Xing, M. S. Alam, M. E. Mousa-Pasandi, and D. V. Plant, "Asymmetric self-coherent detection," *Opt. Express*, vol. 29, no. 16, pp. 25412–25427, 2021.

[42] D. Che, C. Sun, and W. Shieh, "Optical field recovery in stokes space," *Journal of Lightwave Technology*, vol. 37, no. 2, pp. 451–460, 2019.

[43] M. Morsy-Osman, M. Chagnon, and D. V. Plant, "Four-dimensional modulation and stokes direct detection of polarization division multiplexed intensities, inter polarization phase and inter polarization differential phase," *Journal of Lightwave Technology*, vol. 34, no. 7, pp. 1585–1592, 2016.

[44] Q. Hu, D. Che, Y. Wang, and W. Shieh, "Advanced modulation formats for high-performance short-reach optical interconnects," *Opt. Express*, vol. 23, no. 3, pp. 3245–3259, 2015.

[45] J. Smith, "Odd-bit quadrature amplitude-shift keying," *IEEE Transactions on Communications*, vol. 23, no. 3, pp. 385–389, 1975.

[46] N. Stojanovic, C. Prodaniuc, L. Zhang, and J. Wei, "210/225 gbit/s pam-6 transmission with ber below kp4-fec/efec and at least 14 db link budget," in *2018 European Conference on Optical Communication (ECOC)*, pp. 1–3, 2018.

[47] A. Alvarado, E. Agrell, D. Lavery, R. Maher, and P. Bayvel, "Replacing the soft-decision fec limit paradigm in the design of optical communication systems," *Journal of Lightwave Technology*, vol. 33, no. 20, pp. 4338–4352, 2015.

[48] J. Cho, L. Schmalen, and P. J. Winzer, "Normalized generalized mutual information as a forward error correction threshold for probabilistically shaped qam," in *2017 European Conference on Optical Communication (ECOC)*, pp. 1–3, 2017.

[49] X. S. J.i Man, W. Chen and L. i Zeng, "A low-cost 100ge optical transceiver module for 2km smf interconnect with pam4 modulation," in *OFC 2014*, pp. 1–3, 2014.

[50] 800G Pluggable Multi-Source Agreement, "200g per lane for future 800g & 1.6t modules," [Online]. Available: https://www.800gmsa.com/documents/200g-per-lane-for-future-800g-and-16t-modules, 2022.

[51] Y. Tian, Y. Lin, J. Zheng, J. Tang, Q. Huang, H. Ma, T. Rahman, M. Kuschnerov, R. Leung, and L. Zhang, "800gb/s-fr4 specification and interoperability analysis," in *2021 Optical Fiber Communications Conference and Exhibition (OFC)*, pp. 1–3, 2021.

[52] P. Kabal and S. Pasupathy, "Partial-response signaling," *IEEE Transactions on Communications*, vol. 23, no. 9, pp. 921–934, 1975.

[53] A. Lender, "The duobinary technique for high-speed data transmission," *IEEE Transactions on Communication and Electronics*, vol. 82, no. 2, pp. 214–218, 1963.

[54] J. Bergmans, *Digital Baseband Transmission and Recording.* Springer US, 2013.

[55] J. Wei, T. Rahman, S. Calabrò, N. Stojanovic, L. Zhang, C. Xie, Z. Ye, and M. Kuschnerov, "Experimental demonstration of advanced modulation formats for data center networks on 200 gb/s lane rate imdd links," *Opt. Express*, vol. 28, no. 23, pp. 35240–35250, 2020.

[56] G. Forney, "Maximum-likelihood sequence estimation of digital sequences in the presence of intersymbol interference," *IEEE Transactions on Information Theory*, vol. 18, no. 3, pp. 363–378, 1972.

[57] M. Eyuboglu and S. Qureshi, "Reduced-state sequence estimation with set partitioning and decision feedback," *IEEE Transactions on Communications*, vol. 36, no. 1, pp. 13–20, 1988.

[58] M. Tomlinson, "New automatic equalizer employing modulo arithmetic," *Electron. Lett.*, vol. 7, no. 5, pp. 138–139, 1971.

[59] H. Harashima and H. Miyakawa, "Matched-transmission technique for channels with intersymbol interference," *IEEE Transactions on Communications*, vol. 20, no. 4, pp. 774–780, 1972.

[60] R. Rath, D. Clausen, S. Ohlendorf, S. Pachnicke, and W. Rosenkranz, "Tomlinson-harashima precoding for dispersion uncompensated pam-4 transmission with direct-detection," *Journal of Lightwave Technology*, vol. 35, no. 18, pp. 3909–3917, 2017.

[61] Q. Hu, M. Chagnon, K. Schuh, F. Buchali, and H. Bülow, "Im/dd beyond bandwidth limitation for data center optical interconnects," *Journal of Lightwave Technology*, vol. 37, no. 19, pp. 4940–4946, 2019.

[62] K. Matsumoto, Y. Yoshida, A. Maruta, A. Kanno, N. Yamamoto, and K.-i. Kitayama, "On the impact of tomlinson-harashima precoding in optical pam transmissions for intra-dcn communication," in *2017 Optical Fiber Communications Conference and Exhibition (OFC)*, pp. 1–3, 2017.

[63] T. Wettlin, S. Ohlendorf, T. Rahman, J. Wei, S. Calabrò, N. Stojanovic, and S. Pachnicke, "Beyond 200 gb/s pam4 transmission using tomlinson-harashima precoding," in *45th European Conference on Optical Communication (ECOC 2019)*, pp. 1–4, 2019.

[64] X. Li, Z. Xing, M. S. Alam, M. Jacques, and D. V. Plant, "102 gbaud pam-4 transmission over 2 km using a pulse shaping filter with asymmetric isi and thomlinson-harashima precoding," in *2020 Optical Fiber Communications Conference and Exhibition (OFC)*, pp. 1–3, 2020.

[65] Q. Hu, K. Schuh, M. Chagnon, F. Buchali, and H. Bülow, "Up to 94 gbd thp pam-4 transmission with 33 ghz bandwidth limitation," in *2018 European Conference on Optical Communication (ECOC)*, pp. 1–3, 2018.

[66] M. S.-B. Hossain, T. Rahman, N. Stojanovic, R. Rosales, T. Wettlin, S. Calabrò, J. Wei, C. Xie, and S. Pachnicke, "Transmission beyond 200 gbit/s with im/dd system for campus and intra-datacenter network applications," *IEEE Photonics Technology Letters*, vol. 33, no. 5, pp. 263–266, 2021.

[67] R. F. H. Fischer, *Precoding and Signal Shaping for Digital Transmission.* John Wiley & Sons, Inc., 2002.

[68] T. Wettlin, S. Calabrò, T. Rahman, M. S.-B. Hossain, J. Wei, N. Stojanovic, and S. Pachnicke, "Improvement of tomlinson-harashima precoding performance for bandwidth-limited im/dd systems," in *2020 European Conference on Optical Communications (ECOC)*, pp. 1–4, 2020.

[69] D. Rafique, A. Napoli, S. Calabro, and B. Spinnler, "Digital preemphasis in optical communication systems: On the dac requirements for terabit transmission applications," *Journal of Lightwave Technology*, vol. 32, no. 19, pp. 3247–3256, 2014.

[70] D. Rafique, T. Rahman, A. Napoli, and B. Spinnler, "Digital pre-emphasis in optical communication systems: On the nonlinear performance," *Journal of Lightwave Technology*, vol. 33, no. 1, pp. 140–150, 2015.

[71] G. Khanna, B. Spinnler, S. Calabrò, E. De Man, and N. Hanik, "A robust adaptive pre-distortion method for optical communication transmitters," *IEEE Photonics Technology Letters*, vol. 28, no. 7, pp. 752–755, 2016.

[72] G. Khanna, B. Spinnler, S. Calabrò, E. de Man, Y. Chen, and N. Hanik, "Adaptive transmitter pre-distortion using feedback from the far-end receiver," *IEEE Photonics Technology Letters*, vol. 30, no. 3, pp. 223–226, 2018.

[73] N. Stojanovic, F. Karinou, Z. Qiang, and C. Prodaniuc, "Volterra and wiener equalizers for short-reach 100g pam-4 applications," *Journal of Lightwave Technology*, vol. 35, no. 21, pp. 4583–4594, 2017.

[74] K.-D. Kammeyer, *Nachrichtenübertragung*. Vieweg+Treubner Verlag, 5 ed., 2011.

[75] A. Zaknich, *Priciples of Adaptive Filters and Self-learning Systems*. Springer-Verlag London Limited, 2005.

[76] Z. M. R. Alexander D. Poularikas, *Adaptive Filtering Primer with Matlab*. Taylor & Francis Group, LLC, 2006.

[77] D. Slock, "On the convergence behavior of the lms and the normalized lms algorithms," *IEEE Transactions on Signal Processing*, vol. 41, no. 9, pp. 2811–2825, 1993.

[78] V. Mathews, "Adaptive polynomial filters," *IEEE Signal Processing Magazine*, vol. 8, no. 3, pp. 10–26, 1991.

[79] M. Schetzen, "Nonlinear system modeling based on the wiener theory," *Proceedings of the IEEE*, vol. 69, no. 12, pp. 1557–1573, 1981.

[80] C. Xia and W. Rosenkranz, "Performance enhancement for duobinary modulation through nonlinear electrical equalization," in *2005 31st European Conference on Optical Communication, ECOC 2005*, vol. 2, pp. 255–256 vol.2, 2005.

[81] K.-Z. Chen, L.-W. Chen, C.-Y. Lin, W.-J. Huang, C.-C. Wei, and J. Chen, "224-gbps transmission for next-generation wdm long-reach pon using cap modulation," in *2016 Optical Fiber Communications Conference and Exhibition (OFC)*, pp. 1–3, 2016.

[82] X. Li, S. Zhou, H. Ji, M. Luo, Q. Yang, L. Yi, R. Hu, C. Li, S. Fu, A. Alphones, W.-D. Zhong, and C. Yu, "Transmission of 4x28-gb/s pam-4 over 160-km single mode fiber using 10g-class dml and photodiode," in *2016 Optical Fiber Communications Conference and Exhibition (OFC)*, pp. 1–3, 2016.

[83] Y. Gao, J. C. Cartledge, S. S.-H. Yam, A. Rezania, and Y. Matsui, "112 gb/s pam-4 using a directly modulated laser with linear pre-compensation and nonlinear post-compensation," in *ECOC 2016; 42nd European Conference on Optical Communication*, pp. 1–3, 2016.

[84] W.-J. Huang, W.-F. Chang, C.-C. Wei, J.-J. Liu, Y.-C. Chen, K.-L. Chi, C.-L. Wang, J.-W. Shi, and J. Chen, "93% complexity reduction of volterra nonlinear equalizer by l1-regularization for 112-gbps pam-4 850-nm vcsel optical interconnect," in *2018 Optical Fiber Communications Conference and Exposition (OFC)*, pp. 1–3, 2018.

[85] D. Li, L. Deng, Y. Ye, Y. Zhang, H. Song, M. Cheng, S. Fu, M. Tang, and D. Liu, "Amplifier-free 4x96 gb/s pam8 transmission enabled by modified volterra equalizer for short-reach applications using directly modulated lasers," *Opt. Express*, vol. 27, no. 13, pp. 17927–17939, 2019.

[86] C. Bluemm, M. Schaedler, S. Calabrò, G. Charlet, C. Xie, F. Pittalà, and M. Kuschnerov, "Equalizing nonlinearities with memory effects: Volterra series vs. deep neural networks," in *45th European Conference on Optical Communication (ECOC 2019)*, pp. 1–4, 2019.

[87] R. Raich and G. Zhou, "Orthogonal polynomials for complex gaussian processes," *IEEE Transactions on Signal Processing*, vol. 52, no. 10, pp. 2788–2797, 2004.

[88] C.-Y. Chuang, W.-F. Chang, C.-C. Wei, C.-J. Ho, C.-Y. Huang, J.-W. Shi, L. Henrickson, Y.-K. Chen, and J. Chen, "Sparse volterra nonlinear equalizer by employing pruning algorithm for high-speed pam-4 850-nm vcsel optical interconnect," in *2019 Optical Fiber Communications Conference and Exhibition (OFC)*, pp. 1–3, 2019.

[89] G. S. Yadav, C.-Y. Chuang, K.-M. Feng, J.-H. Yan, J. Chen, and Y.-K. Chen, "Reducing computation complexity by using elastic net regularization based pruned volterra equalization in a 80 gbps pam-4 signal for inter-data center interconnects," *Opt. Express*, vol. 28, no. 26, pp. 38539–38552, 2020.

[90] L. Shu, J. Li, Z. Wan, Z. Yu, X. Li, M. Luo, S. Fu, and K. Xu, "Single-photodiode 112-gbit/s 16-qam transmission over 960-km ssmf enabled by kramers-kronig detection and sparse i/q volterra filter," *Opt. Express*, vol. 26, no. 19, pp. 24564–24576, 2018.

[91] Y. Chen, Y. Gu, and A. O. Hero, "Sparse lms for system identification," in *2009 IEEE International Conference on Acoustics, Speech and Signal Processing*, pp. 3125–3128, 2009.

[92] K. K. J. Kim, "Digital predistortion of wideband signals based on power amplifier model with memory," *Electronics Letters*, vol. 37, pp. 1417–1418(1), 2001.

[93] E. L. O. Batista, R. Seara, "On the performance of adaptive pruned volterra filters," *Signal Processing*, vol. 93, no. 7, pp. 1909–1920, 2013.

[94] H. Xin, K. Zhang, D. Kong, Q. Zhuge, Y. Fu, S. Jia, W. Hu, and H. Hu, "Nonlinear tomlinson-harashima precoding for direct-detected double sideband pam-4 transmission without dispersion compensation," *Opt. Express*, vol. 27, no. 14, pp. 19156–19167, 2019.

[95] Y. Yu, M. R. Choi, T. Bo, Z. He, Y. Che, and H. Kim, "Low-complexity second-order volterra equalizer for dml-based im/dd transmission system," *Journal of Lightwave Technology*, vol. 38, no. 7, pp. 1735–1746, 2020.

[96] T. Wettlin, S. Pachnicke, T. Rahman, J. Wei, S. Calabro, and N. Stojanovic, "Complexity reduction of volterra nonlinear equalization for optical short-reach im/dd systems," in *Photonic Networks; 21th ITG-Symposium*, pp. 1–6, 2020.

[97] T. Wettlin, T. Rahman, S. Calabrò, J. Wei, M. S.-B. Hossain, N. Stojanovic, and S. Pachnicke, "Low-complexity nonlinearity compensation for short-reach im/dd systems using pam," in *2021 Optical Fiber Communications Conference and Exhibition (OFC)*, pp. 1–3, 2021.

[98] J. Zhang, X. Wu, L. Sun, J. Liu, A. P. T. Lau, C. Guo, S. Yu, and C. Lu, "C-band 120-gb/s pam-4 transmission over 50-km ssmf with improved weighted decision-feedback equalizer," *Opt. Express*, vol. 29, no. 25, pp. 41622–41633, 2021.

[99] J. Palicot, "A weighted decision feedback equalizer with limited error propagation," in *2000 IEEE International Conference on Communications*, pp. 377–381, 2000.

[100] J. Palicot and A. Goupil, "Performance analysis of the weighted decision feedback equalizer," *Signal Processing*, vol. 88, no. 2, pp. 284–295, 2008.

[101] J. Zhou, C. Yang, D. Wang, Q. Sui, H. Wang, S. Gao, Y. Feng, W. Liu, Y. Yan, J. Li, C. Yu, and Z. Li, "Burst-error-propagation suppression for decision-feedback equalizer in field-trial submarine fiber-optic communications," *Journal of Lightwave Technology*, vol. 39, no. 14, pp. 4601–4606, 2021.

[102] T. Wettlin, T. Rahman, S. Calabrò, M. S.-B. Hossain, J. Wei, N. Stojanovic, and S. Pachnicke, "Investigation of weighted dfe for high-rate short-reach transmission," in *2022 OptoElectronics and Communications Conference (OECC)*, pp. 1–4, 2022.

[103] Y. Zhu, F. Zhang, F. Yang, L. Zhang, X. Ruan, Y. Li, and Z. Chen, "Toward single lane 200g optical interconnects with silicon photonic modulator," *Journal of Lightwave Technology*, vol. 38, no. 1, pp. 67–74, 2020.

[104] K. Zhong, X. Zhou, Y. Gao, W. Chen, J. Man, L. Zeng, A. P. T. Lau, and C. Lu, "140-gb/s 20-km transmission of pam-4 signal at 1.3 μm for short reach communications," *IEEE Photonics Technology Letters*, vol. 27, no. 16, pp. 1757–1760, 2015.

[105] L. Liu, L. Li, and Y. Lu, "Detection of 56gbaud pdm-qpsk generated by commercial cmos dac with 11ghz analog bandwidth," in *2014 The European Conference on Optical Communication (ECOC)*, pp. 1–3, 2014.

[106] T. Wettlin, S. Calabrò, T. Rahman, J. Wei, N. Stojanovic, and S. Pachnicke, "Dsp for high-speed short-reach im/dd systems using pam," *Journal of Lightwave Technology*, vol. 38, no. 24, pp. 6771–6778, 2020.

[107] J. G. Proakis, D. G. Manolakis, *Digital Signal Processing - Principles, Algorithms and Applications*. Prentice-Hall, Inc., 3 ed., 1996.

[108] R. Bos, S. de Waele, and P. Broersen, "Autoregressive spectral estimation by application of the burg algorithm to irregularly sampled data," *IEEE Transactions on Instrumentation and Measurement*, vol. 51, no. 6, pp. 1289–1294, 2002.

[109] S. de Waele and P. Broersen, "The burg algorithm for segments," *IEEE Transactions on Signal Processing*, vol. 48, no. 10, pp. 2876–2880, 2000.

[110] A. Viterbi, "Error bounds for convolutional codes and an asymptotically optimum decoding algorithm," *IEEE Transactions on Information Theory*, vol. 13, no. 2, pp. 260–269, 1967.

[111] G. Forney, "The viterbi algorithm," *Proceedings of the IEEE*, vol. 61, no. 3, pp. 268–278, 1973.

[112] A. S. Karar, "Iterative algorithm for electronic dispersion compensation in im/dd systems," *Journal of Lightwave Technology*, vol. 38, no. 4, pp. 698–704, 2020.

[113] X. Wu, A. S. Karar, K. Zhong, A. P. T. Lau, and C. Lu, "Experimental demonstration of pre-electronic dispersion compensation in im/dd systems using an iterative algorithm," *Opt. Express*, vol. 29, no. 16, pp. 24735–24749, 2021.

[114] D. Zou, F. Li, W. Wang, M. Yin, Q. Sui, and Z. Li, "Modified gerchberg-saxton algorithm based electrical dispersion pre-compensation for intensity-modulation and direct-detection systems," *Journal of Lightwave Technology*, vol. 40, no. 9, pp. 2840–2849, 2022.

[115] T. Wettlin, S. Calabrò, T. Rahman, Md S.-B. Hossain, J. Wei, N. Stojanovic, S. Pachnicke, "Improved Pre-Compensation to Combat Power Fading in IM/DD Systems," in *2022 European Conference on Optical Communication (ECOC)*, pp. 1–3, 2022.

[116] Y. Matsui, D. Mahgerefteh, X. Zheng, C. Liao, Z. Fan, K. McCallion, and P. Tayebati, "Chirp-managed directly modulated laser (cml)," *IEEE Photonics Technology Letters*, vol. 18, no. 2, pp. 385–387, 2006.

[117] S. T. Le, Y. Matsui, G. Raybon, A. Venna, M. Kwakernaak, and T. Sudo, "Reach extension for 100 gb/s pam-4 im/dd transmission by chirp managed laser," in *2022 Optical Fiber Communications Conference and Exhibition (OFC)*, pp. 1–3, 2022.

[118] S. Liu, P.-C. Peng, L. Huang, C.-W. Hsu, H. Tian, and G.-K. Chang, "Bandwidth-enhanced pam-4 transmissions using polarization modulation and direct detection with a tunable frequency range," *Journal of Lightwave Technology*, vol. 37, no. 3, pp. 1014–1022, 2019.

[119] R. Borkowski, H. Schmuck, G. Cerulo, J.-G. Provost, V. Houtsma, D. van Veen, E. Harstead, F. Mallecot, and R. Bonk, "The impact of transmitter chirp parameter on the power penalty and design of 50 gbit/s tdm-pon," in *2020 Optical Fiber Communications Conference and Exhibition (OFC)*, pp. 1–3, 2020.

[120] M. N. Ngo, H. T. Nguyen, C. Gosset, D. Erasme, Q. Deniel, N. Genay, R. Guillamet, N. Lagay, J. Decobert, F. Poingt, and R. Brenot, "Electroabsorption modulated laser integrated with a semiconductor optical amplifier for 100-km 10.3 gb/s dispersion-penalty-free transmission," *Journal of Lightwave Technology*, vol. 31, no. 2, pp. 232–238, 2013.

[121] Q. Zhang, N. Stojanovic, C. Xie, C. Prodaniuc, and P. Laskowski, "Transmission of single lane 128 gbit/s pam-4 signals over an 80 km ssmf link, enabled by ddmzm aided dispersion pre-compensation," *Opt. Express*, vol. 24, no. 21, pp. 24580–24591, 2016.

[122] R. Killey, P. Watts, V. Mikhailov, M. Glick, and P. Bayvel, "Electronic dispersion compensation by signal predistortion using digital processing and a dual-drive mach-zehnder modulator," *IEEE Photonics Technology Letters*, vol. 17, no. 3, pp. 714–716, 2005.

[123] J. Zhang, J. Yu, J. Shi, and H.-C. Chien, "Digital dispersion pre-compensation and nonlinearity impairments pre- and post-processing for c-band 400g pam-4 transmission over ssmf based on direct-detection," in *2017 European Conference on Optical Communication (ECOC)*, pp. 1–3, 2017.

[124] P. Torres-Ferrera, G. Rizzelli, V. Ferrero, and R. Gaudino, "100+ gbps/Î» 50 km c-band downstream pon using cd digital pre-compensation and direct-detection onu receiver," *Journal of Lightwave Technology*, vol. 38, no. 24, pp. 6807–6816, 2020.

[125] A. Mecozzi, C. Antonelli, and M. Shtaif, "Kramers–kronig coherent receiver," *Optica*, vol. 3, no. 11, pp. 1220–1227, 2016.

[126] A. Mecozzi, "A necessary and sufficient condition for minimum phase and implications for phase retrieval," 2016.

[127] S. T. Le, K. Schuh, M. Chagnon, F. Buchali, R. Dischler, V. Aref, H. Buelow, and K. M. Engenhardt, "1.72-tb/s virtual-carrier-assisted direct-detection transmission over 200 km," *Journal of Lightwave Technology*, vol. 36, no. 6, pp. 1347–1353, 2018.

[128] S. T. Le, K. Schuh, F. Buchali, X. Q. Du, M. Grözing, M. Berroth, L. Schmalen, and H. Buelow, "16×200 gbps virtual carrier assisted dd transmission over 80 km with only 14 ghz of digitizer bandwidth," in *45th European Conference on Optical Communication (ECOC 2019)*, pp. 1–4, 2019.

[129] Y. Wei, Y. Zhou, C. Liu, K. Wang, J. Zhang, F. Wang, J. Ding, and J. Yu, "Ssb single carrier and multicarrier in c-band fso transmission with kk receiver," *Journal of Lightwave Technology*, vol. 38, no. 18, pp. 5000–5007, 2020.

[130] S. T. Le, K. Schuh, F. Buchali, and H. Nguyen Tan, "5 × 240 gb/s wdm dd transmission over 80 km with spectral efficiency of 5.25 bit/s/hz," *IEEE Photonics Technology Letters*, vol. 31, no. 22, pp. 1830–1833, 2019.

[131] K. Wang, Y. Wei, M. Zhao, W. Zhou, and J. Yu, "140-gb/s ps-256-qam transmission in an ofdm system using kramers-kronig detection," *IEEE Photonics Technology Letters*, vol. 31, no. 17, pp. 1405–1408, 2019.

[132] S. T. Le, K. Schuh, R. Dischler, F. Buchali, L. Schmalen, and H. Buelow, "Beyond 400 gb/s direct detection over 80 km for data center interconnect applications," *Journal of Lightwave Technology*, vol. 38, no. 2, pp. 538–545, 2020.

[133] I. Sackey, C. Schmidt-Langhorst, R. Emmerich, R. Elschner, T. Kato, T. Tanimura, S. Watanabe, T. Hoshida, and C. Schubert, "Distributed aggregation and reception of a 400-gb/s net rate superchannel in a single-photodiode 110-ghz kramers-kronig receiver," in *2018 Optical Fiber Communications Conference and Exposition (OFC)*, pp. 1–3, 2018.

[134] K. Schuh, S. T. Le, R. Dischler, and F. Buchali, "Transmission of 90 gbd 32 qam over 480 km of ssmf with kramers-kronig detection," in *2019 Optical Fiber Communications Conference and Exhibition (OFC)*, pp. 1–3, 2019.

[135] S. T. Le, K. Schuh, R. Dischler, F. Buchali, L. Schmalen, and H. Buelow, "5×510 gbps single-polarization direct-detection wdm transmission over 80 km of ssmf," in *2019 Optical Fiber Communications Conference and Exhibition (OFC)*, pp. 1–3, 2019.

[136] R. W. Boyd, *Nonlinear Optics*. Elsevier, Inc., 4 ed., 2020.

[137] H. Voelcker, "Demodulation of single-sideband signals via envelope detection," *IEEE Transactions on Communication Technology*, vol. 14, no. 1, pp. 22–30, 1966.

[138] T. Bo and H. Kim, "Kramers-kronig receiver operable without digital upsampling," *Opt. Express*, vol. 26, no. 11, pp. 13810–13818, 2018.

[139] T. M. Hoang, Q. Zhuge, Z. Xing, M. Sowailem, M. Morsy-Osman, and D. V. Plant, "Single wavelength 480 gb/s direct detection transmission over 80 km ssmf enabled by stokes vector receiver and reduced-complexity ssbi cancellation," in *2018 Optical Fiber Communications Conference and Exposition (OFC)*, pp. 1–3, 2018.

[140] S. Randel, D. Pilori, S. Chandrasekhar, G. Raybon, and P. Winzer, "100-gb/s discrete-multitone transmission over 80-km ssmf using single-sideband modulation with novel interference-cancellation scheme," in *2015 European Conference on Optical Communication (ECOC)*, pp. 1–3, 2015.

[141] R. K. Patel, F. P. Guiomar, M. A. Fernandes, I. A. Alimi, P. P. Monteiro, N. J. Muga, and A. N. Pinto, "Virtual carrier assisted self-coherent detection employing dc-value method," in *2021 Optical Fiber Communications Conference and Exhibition (OFC)*, pp. 1–3, 2021.

[142] R. K. Patel, I. A. Alimi, N. J. Muga, and A. N. Pinto, "Optical signal phase retrieval with low complexity dc-value method," *Journal of Lightwave Technology*, vol. 38, no. 16, pp. 4205–4212, 2020.

[143] R. Schmogrow, B. Nebendahl, M. Winter, A. Josten, D. Hillerkuss, S. Koenig, J. Meyer, M. Dreschmann, M. Huebner, C. Koos, J. Becker, W. Freude, and J. Leuthold, "Error vector magnitude as a performance measure for advanced modulation formats," *IEEE Photonics Technology Letters*, vol. 24, no. 1, pp. 61–63, 2012.

[144] T. Wettlin, S. Calabrò, T. Rahman, M. S.-B. Hossain, J. Wei, N. Stojanovic, and S. Pachnicke, "Comparison of direct-detection approaches for high-speed datacenter campus networks," in *2021 European Conference on Optical Communication (ECOC)*, pp. 1–4, 2021.

Publikationen des Autors mit Eigenanteilen

[1] Impact of DAC Properties on Tomlinson-Harashima Precoding for 200 Gb/s Intra Datacenter Links, IEEE Photonics Conference (IPC), San Antonio, USA, October 2019
Autoren: T. Wettlin, R. Weixer, T. Rahman, J. Wei, S. Calabrò, N. Stojanovic, S. Pachnicke

Konzeptionierung	Planung	Durchführung	Manuskripterstellung
hoch	hoch	hoch	hoch

[2] Beyond 200 Gb/s PAM4 transmission using Tomlinson-Harashima precoding, European Conference on Optical Communication (ECOC), Dublin, Ireland, September 2019
Autoren: T. Wettlin, S. Ohlendorf, T. Rahman, J. Wei, S. Calabrò, N. Stojanovic, S. Pachnicke

Konzeptionierung	Planung	Durchführung	Manuskripterstellung
hoch	hoch	hoch	hoch

[3] Optimized flexible mappings with multidimensional modulation for coherent optical transport, European Conference on Optical Communication (ECOC), Dublin, Ireland, September 2019
Autoren: S. Ohlendorf, T. Wettlin, S. Pachnicke, W. Rosenkranz

Konzeptionierung	Planung	Durchführung	Manuskripterstellung
niedrig	niedrig	niedrig	niedrig

[4] Adaptive Optical Transmission Systems employing Multidimensional Modulation, International Conference on Transparent Optical Networks (ICTON), Angers, France, July 2019
Autoren: S. Ohlendorf, T. Wettlin, S. Pachnicke, W. Rosenkranz

Konzeptionierung	Planung	Durchführung	Manuskripterstellung
niedrig	niedrig	niedrig	niedrig

[5] Comparison of PAM Formats for 200 Gb/s Short Reach Transmission Systems, Optical Fiber Communication Conference (OFC), San Diego, USA, March 2020
Autoren: T. Wettlin, T. Rahman, J. Wei, S. Calabrò, N. Stojanovic, S. Pachnicke

Konzeptionierung	Planung	Durchführung	Manuskripterstellung
hoch	hoch	hoch	hoch

[6] DSP for High-Speed Short-Reach IM/DD Systems Using PAM, Journal of Lightwave Technology, vol. 38, no. 24, December 2020
Autoren: T. Wettlin, S. Calabrò, T. Rahman, J. Wei, N. Stojanovic, S. Pachnicke

Konzeptionierung	Planung	Durchführung	Manuskripterstellung
hoch	hoch	hoch	hoch

[7] Complexity Reduction of Volterra Nonlinear Equalization for Optical Short-Reach IM/DD Systems, ITG Conference "Photonic Networks", online, November 2020
Autoren: T. Wettlin, T. Rahman, J. Wei, S. Calabrò, N. Stojanovic, S. Pachnicke

Konzeptionierung	Planung	Durchführung	Manuskripterstellung
hoch	hoch	hoch	hoch

[8] Improvement of Tomlinson-Harashima Precoding Performance for Bandwidth-Limited IM/DD Systems, European Conference on Optical Communications (ECOC), online, December 2020
Autoren: T. Wettlin, S. Calabrò, T. Rahman, M. S-B. Hossain, J. Wei, N. Stojanovic, S. Pachnicke

Konzeptionierung	Planung	Durchführung	Manuskripterstellung
hoch	hoch	hoch	hoch

[9] Transmission Beyond 200 Gbit/s With IM/DD System for Campus and Intra-Datacenter Network Applications, IEEE Photonics Technology Letters, vol. 33, no. 5, March 2021
Autoren: M S-B. Hossain, T. Rahman, N. Stojanovic, R. Rosales, T. Wettlin, S. Calabrò, J. Wei, C. Xie, S. Pachnicke

Konzeptionierung	Planung	Durchführung	Manuskripterstellung
mittel	niedrig	niedrig	niedrig

[10] Experimental Comparison of Uniform and Probabilistically Shaped PAM-8 for IMDD System at Transmission Rates Beyond 200 Gbit/s, Optical Fiber Communication Conference (OFC), online, June 2021
Autoren: M. S-B. Hossain, T. Rahman, G. Böcherer, N. Stojanovic, T. Wettlin, S. Calabrò, J. Wei, C. Xie, and S. Pachnicke

Konzeptionierung	Planung	Durchführung	Manuskripterstellung
niedrig	niedrig	niedrig	niedrig

[11] Feasibility of Transmitting 270 Gbit/s with PAM-8 in O-band CWDM4 with IM/DD System, Optical Fiber Communication Conference (OFC), online, June 2021
Autoren: M. S-B. Hossain, T. Rahman, N. Stojanovic, T. Wettlin, S. Calabrò, J. Wei, C. Xie, and S. Pachnicke

Konzeptionierung	Planung	Durchführung	Manuskripterstellung
niedrig	niedrig	niedrig	niedrig

[12] Low-Complexity Nonlinearity Compensation for Short-Reach IM/DD Systems using PAM, Optical Fiber Communication Conference (OFC), online, June 2021
Autoren: T. Wettlin, T. Rahman, S. Calabrò, J. Wei, M. S-B. Hossain, N. Stojanovic, S. Pachnicke

Konzeptionierung	Planung	Durchführung	Manuskripterstellung
hoch	hoch	hoch	hoch

[13] Single-Lane 402 Gb/s PAM-8 IM/DD Transmission Based on a Single DAC and an O-Band Commercial EML, Optoelectronics and Communications Conference (OECC), online, July 2021
Autoren: M. S-B. Hossain, J. Wei, F. Pittalà, N. Stojanovic, S. Calabrò, T. Rahman, T. Wettlin, C. Xie, M. Kuschnerov, S. Pachnicke

Konzeptionierung	Planung	Durchführung	Manuskripterstellung
niedrig	niedrig	niedrig	niedrig

[14] Experimental Comparison of Cap and Cup Probabilistically Shaped PAM for O-Band IM/DD Transmission System, European Conference on Optical Communication (ECOC), Bordeaux, France, September 2021
Autoren: M. S-B. Hossain, G. Böcherer, T. Rahman, N. Stojanovic, P. Schulte, S. Calabrò, J. Wei, C. Bluemm, T. Wettlin, C. Xie, M. Kuschnerov, S. Pachnicke

Konzeptionierung	Planung	Durchführung	Manuskripterstellung
niedrig	niedrig	niedrig	niedrig

[15] Comparison of Direct-Detection Approaches for High-Speed Datacenter Campus Networks, European Conference on Optical Communication (ECOC), Bordeaux, France, September 2021
Autoren: T. Wettlin, S. Calabrò, T. Rahman, M. S-B. Hossain, J. Wei, N. Stojanovic, S. Pachnicke

Konzeptionierung	Planung	Durchführung	Manuskripterstellung
hoch	hoch	hoch	hoch

[16] 402 Gb/s PAM-8 IM/DD O-Band EML Transmission, European Conference on Optical Communication (ECOC), Bordeaux, France, September 2021
Autoren: M. S-B. Hossain, J. Wei, F. Pittalà, N. Stojanovic, S. Calabrò, T. Rahman, G. Böcherer, T. Wettlin, C. Xie, M. Kuschnerov, S. Pachnicke

Konzeptionierung	Planung	Durchführung	Manuskripterstellung
niedrig	niedrig	niedrig	niedrig

[17] Direct-detection is the right choice?, European Conference on Optical Communication (ECOC), Workshop "Applications for IMDD and Coherent in Short Reach Systems", Bordeaux, France, September 2021
Autoren: T. Wettlin, S. Pachnicke

Konzeptionierung	Planung	Durchführung	Manuskripterstellung
hoch	hoch	hoch	hoch

[18] Partial Response O-band EML Transmission Beyond 300-GBd with a 128/256 GSa/s DAC, Optical Fiber Communication Conference (OFC), San Diego, USA, March 2022
Autoren: M. S-B. Hossain, T. Rahman, N. Stojanovic, F. Pittalà, S. Calabrò, G. Böcherer, T. Wettlin, J. Wei, C. Xie, M. Kuschnerov, S. Pachnicke

Konzeptionierung	Planung	Durchführung	Manuskripterstellung
niedrig	niedrig	niedrig	niedrig

[19] Investigation of Weighted DFE for High-Rate Short-Reach Transmission, OptoElectronics and Communications Conference (OECC), Toyama, Japan, July 2022
Autoren: T. Wettlin, T. Rahman, S. Calabrò, M. S-B. Hossain, J. Wei, N. Stojanovic, S. Pachnicke

Konzeptionierung	Planung	Durchführung	Manuskripterstellung
hoch	hoch	hoch	hoch

[20] Experimental Comparison of PAM-8 Probabilistic Shaping with Different Gaussian Orders at 200 Gb/s Net Rate in IM/DD System with O-Band TOSA, European Conference on Optical Communication (ECOC), Basel, Switzerland, September 2022
Autoren: M. S-B. Hossain, G. Böcherer, Y. Lin, S. Li, S. Calabrò, A. Nedelcu, T. Rahman, T. Wettlin, J. Wei, N. Stojanovic, C. Xie, M. Kuschnerov, S. Pachnicke

Konzeptionierung	Planung	Durchführung	Manuskripterstellung
niedrig	niedrig	niedrig	niedrig

[21] Improved Pre-Compensation to Combat Power Fading in IM/DD Systems, European Conference on Optical Communication (ECOC), Basel, Switzerland, September 2022
Autoren: T. Wettlin, S. Calabrò, T. Rahman, M. S-B. Hossain, J. Wei, N. Stojanovic, S. Pachnicke

Konzeptionierung	Planung	Durchführung	Manuskripterstellung
hoch	hoch	hoch	hoch

[22] Advanced DSP for IM/DD PON, European Conference on Optical Communication (ECOC), Workshop "The path towards Terabit/s PONs: Enabling multi Gbit/s data rate services", Basel, Switzerland, September 2022
Autoren: T. Wettlin, S. Pachnicke

Konzeptionierung	Planung	Durchführung	Manuskripterstellung
hoch	hoch	hoch	hoch